March 2020

METABOLIC MODELING OF MULTISPECIES MICROBIAL BIOFILMS

Poonam Phalak
University of Massachusetts Amherst

METABOLIC MODELING OF MULTISPECIES MICROBIAL BIOFILMS

A Dissertation Presented

by

POONAM PHALAK

Submitted to the Graduate School of the
University of Massachusetts Amherst in partial fulfillment
of the requirements for the degree of

DOCTOR OF PHILOSOPHY

February, 2020

Department of Chemical Engineering

METABOLIC MODELING OF MULTISPECIES MICROBIAL BIOFILMS

A Dissertation Presented

by

POONAM PHALAK

Approved as to style and content by:

Michael A. Henson, Chair

Jessica Schiffman, Member

Jeffrey Blanchard, Member

John Klier, Department Chair
Department of Chemical Engineering

DEDICATION

In loving memory of my father Liladhar Phalak

ACKNOWLEDGMENTS

I am very grateful to my advisor Prof. Michael A. Henson for giving me an opportunity to work on this project. His guidance, support and motivation helped me throughout my work and have instilled discipline in me that would help me throughout my career. I would like to thank Prof. Jessica Schiffman and Prof. Jeffrey Blanchard for serving as committee members, providing directions and feedback on the project.

I would like to thank Prof. Ross Carlson for providing insights on the biofilm dynamics and chronic wounds. I am thankful to Dr. Jose A. Gomez in Prof. Paul I. Barton research group at MIT for sharing expertise on using dynamic flux balance tool. I would also like to thank Dr. Hyun Seob Song and Dr. William Cannon for giving me an opportunity to work at Pacific National Lab as an intern. Their valuable guidance and support were instrumental in the progress of the project.

I am thankful to Dr. Sanjeev Katti for inspiring me to pursue the PhD, without his help and motivation, this journey wouldn't have been possible. I am grateful to my mother and brother who have unconditionally supported me throughout my studies and constantly motivated me to perform better each day. I would also like to thank my husband for motivating and supporting me throughout the PhD. This journey wouldn't have been possible without the support of my dear friends in Amherst and in India. Special thanks to Hemant, Shashank, Ashish, Harshwardhan, Neeraja and Dwaipayan for being there to lift my spirits during difficult times. I am also thankful to my group members Aditya, Jin, Boyang, Xiangan, Ayushi and Feem for your valuable feedback and help throughout this journey.

I am also grateful to the funding agencies NIH and UMass Biotechnology training program for providing financial support for conducting this work.

ABSTRACT

METABOLIC MODELING OF MULTISPECIES MICROBIAL BIOFILMS

FEBRUARY, 2020

POONAM PHALAK

B.Chem.Engg., INSTITUTE OF CHEMICAL TECHNOLOGY, MUMBAI

Ph.D., UNIVERSITY OF MASSACHUSETTS AMHERST

Directed by: Professor Michael A. Henson

Biofilms are ubiquitous in medical, environmental, and engineered microbial systems. The majority of naturally occurring microbes grow as mixed species biofilms. These complicated biofilm consortia are comprised of many cell phenotypes with complex interactions and self-organized into three-dimensional structures. Approximately 2% of the US population suffers from non-healing chronic wounds infected by a combination of commensal and pathogenic bacteria whereas about 500,000 cases of *Clostridium difficile* infections (CDI) are reported annually. These polymicrobial infections are often resilient to antibiotic treatment due to the nutrient-rich environments within the biofilms and species interactions that promote community stability and robustness. This thesis focuses on developing metabolic modeling framework to study the interactions and the spatial/temporal organizations in the biofilms. The modeling framework is based on solving genome scale metabolic reconstructions of considered species to predict species abundances, growth rates and byproduct secretions.

The spatiotemporal modeling framework accounts for the nutrient concentration gradients in the biofilm system. Spatiotemporal biofilm metabolic models were formulated by combining genome scale metabolic reconstructions of considered species with uptake kinetics for available nutrients and reaction-diffusion type equations for species biomass, supplied substrates and synthesized metabolic byproducts. The resulting partial differential equations embedded with linear programs were discretized in the space and integrated using a dynamic flux balance method. This framework was used to calculate the spatial and temporal variations in the species, nutrient and byproduct concentrations in biofilms. This framework was applied to analyze the biofilms associated with chronic wound infections, CDI and environmental biofilms. The chronic wound biofilm model was comprising of two most dominant species, *Pseudomonas aeruginosa* and *Staphylococcus aureus*. The model predicted partitioning of species based on their nutritional niches consistent with *in vitro* experiments. The CDI biofilm model was comprising of representative species from three most common phyla in gut *Bacteroidetes thetaiotaomicron*, *Faecalibacterium prausnitzii*, *Escherichia coli* and pathogen *C. difficile*. The simulation results were used to study the interspecies interactions, the spatial partitioning in the biofilms and important crossfeeding relationships within the community. These predictions would be useful in devising effective antibiotic treatment strategies to cure the biofilm infections associated with chronic wounds and *C. difficile*. The environmental biofilm model for cyanobacteria and heterotrophs was developed and validated with the experimental results, this model was used to evaluate the community dynamics under extreme environmental conditions.

The steady state community modeling framework considered biofilm as a well-mixed homogeneous system at steady state. This framework can be used when the community is large and can not be easily solved as a spatiotemporal biofilm. Steady state *in silico* community models were formulated by combining genome scale

metabolic reconstructions of the considered species. The community models were solved using SteadyCom method. This method uses community flux balance analysis to calculate the relative abundance of each species with an objective of maximizing the community growth rate. A 12 species chronic wound community metabolic model covering 74% of 16S rDNA pyrosequencing reads of dominant genera from 2,963 chronic wound patients was developed. The community model was used to predict species abundances averaged across this large patient population. The simulation results from this study were used to identify putative mutualistic interactions between bacteria that could be targeted to enhance treatment efficacy. The frameworks developed in this thesis would be useful in developing patient/disease specific therapeutic treatments.

TABLE OF CONTENTS

LIST OF TABLES

Table **Page**

LIST OF FIGURES

Figure **Page**

CHAPTER 1

INTRODUCTION

1.1 Microbial communities and biofilms

Biofilms are thin slimy layers of bacteria growing on either living or non living surfaces. Bacteria produce slimy extracellular polymeric substances and form a three dimensional robust structure around them. The bacteria living inside the biofilms interact with each other using mutualistic, syntrophic, commensal or antagonistic strategies to compete for and efficiently utilize available nutrients [2–5]. Microbes residing in biofilms exhibit phenotypes distinct from planktonic growth. For instance, bacteria in biofilms can tolerate antimicrobial agent concentrations 10,000 times higher than the same microbes grown planktonically [6, 7].

Microbial biofilms are critically important in medical, environmental and engineered biological systems. For example, the human gut microbiome has emerged as a major focus for biomedical research with mounting evidence suggesting unhealthy gut flora biofilms are associated with illnesses including autoimmune diseases, colorectal cancer and inflammatory bowel disease [8–13]. Environmental microbial biofilm consortia form the basis of global nutrient cycles from nitrogen fixation to carbon fluxes [14, 15]. Additionally, the study of natural biofilms has recently gained in popularity due to their efficient organization and ability, through synergistic interactions, to optimize multiple tasks simultaneously like the deconstruction of complex, recalcitrant plant materials into simple sugars. A major goal of current biofuels research is to engineer synthetic microbial communities that mimic these naturally occurring biofilms for biomass conversion to renewable liquid fuels [16]. While foundational to

the vast majority of microbial life on the planet, the basic design principles of consortial biofilms are still poorly understood due largely to the complexity of naturally occurring systems [4, 5].

1.2 Microbial communities in human health and diseases

The microbial communities in the biofilms play both positive and negative roles in human health. For example, the gut microbiota comprise a complex ecological system that maintains a critical symbiotic relationship with the human host [17, 18]. The microbiota provide essential nutrients such as short-chain fatty acids (SCFAs; acetate, butyrate and propionate), support colonization resistance to pathogens, participate in the degradation of toxic compounds and regulate the immune responses [19–23]. Bacteroidetes and Firmicutes are the two dominant phyla in the healthy gut, comprising approximately 90% of the community. Other important but less abundant phyla are Proteobacteria, Actinobacteria, Euryarchaeota and Verrucomicrobia as well as Eukaryota such as fungi [24, 25]. The gut microbiota composition can be altered by numerous factors including diet, antibiotic treatment, stress and lifestyle [26, 27]. Dietary components including carbohydrates, protein, fat and host secretions such as primary bile acids and nitrate play a particularly important role in shaping microbiota abundances [28–33].

Unhealthy alterations of the gut microbiota are termed as dysbiosis and represent imbalances in species abundances associated with diseases such as inflammatory bowel diseases, Crohn's disease, obesity and diabetes [34–36]. The anaerobic bacterium *Clostridium difficile* is an opportunistic human pathogen responsible for infections in the colon of the human gastrointestinal tract [37]. Various studies have reported that 3%–15% of healthy adults are asymptomatically colonized with *C. difficile* [38–44]. Commensal species in healthy gut usually provide resistance against *C. difficile* pathogenic colonization. *C. difficile* infection (CDI) is most common in patients previ-

ously treated with broad spectrum antibiotics that disrupt the healthy gut microbiota and reduce competition for available nutrients [45], resulting in dysbiosis conducive to *C. difficile* propagation [46–49]. CDI symptoms can range from mild diarrhea to severe and life threatening colitis [37, 50]. *C. difficile* virulence is attributable to the secretion of the high molecular weight toxins A and B that promote epithelial tissue damage and rapid fluid loss. Some *C. difficile* strains have developed resistance to common antibiotics while also exhibiting more severe pathogenicity [51]. CDI has become particularly common in hospital settings due to the ability of *C. difficile* to form spores that adhere to surfaces and resist common disinfectant protocols. Studies estimate that almost 500,000 CDI cases occur within the U.S. annually [52], resulting in 29,000 deaths and over $4.8 billion in associated costs in acute care facilities alone [53].

The other example of negative bacterial biofilm colonization is non healing chronic wound. Chronic wounds are defined as a host-pathogen environment that has failed to proceed through a timely healing process. Chronic wounds are often colonized by microorganisms growing as biofilms on a complex mixture of wound exudate [54–61]. An estimated 2% of the U.S. population (6 million people) have a non-healing chronic wound with treatment costing more than $25 billion per year [62–64]. Chronic wounds are typically colonized by consortia comprised of different microbial species [55, 54, 56, 65, 66]. Polymicrobial infections have been reported to have elevated mortality rates relative to monocultures [67], and in vivo rabbit model systems demonstrated that consortia prevented wound healing compared to their respective monocultures [61, 68].

1.3 Metabolic modeling of microbial communities

Multispecies biofilms are sufficiently complex to preclude detailed understanding through traditional experimental techniques developed for planktonic cultures. A

primary challenge is to understand the complex interactions between the species and the extracellular environment [69]. *In silico* metabolic models are powerful tools for the analysis of how host environment impacts species interactions and community stability, composition and robustness [70–73]. These modeling frameworks need prior knowledge of the types of interspecies interactions such as mutualism, commensalism or competition and they can be extended to study interactions between maximum five species.

To better understand the metabolic interactions between the species and the environment, we have developed two modeling frameworks based on homogeneity and heterogeneity in the biofilm system considered. The first approach is community modeling framework based on SteadyCom method [74] for efficiently simulating large community models to predict the growth rate, species abundances and metabolite crossfeeding rates between species. This *in silico* computational method is used for efficiently simulating complex and realistic host-associated bacterial communities, connecting host environment and community metabolism, exploring growth-diversity tradeoffs, quantifying metabolite crossfeeding relationships, relating metabolism and disease states, and rationalizing patient-to-patient variability [75, 76]. Our modeling framework exploits the availability of 16S rDNA sequencing data to identify the dominant genera present in the host-associated infection, the AGORA database [77] to select a genome-scale metabolic reconstruction for a representative species from each genera, and the SteadyCom method is used to simulate the community. We have applied the *in silico* methods to a 20 species model of commensal species in the human gut [75] and to a 17 species model including dominant pathogens of the adult cystic fibrosis lung [76]. We have used this framework to study the interspecies interactions between chronic wound microbiota comprising of 12 species.

Most naturally occurring microbial consortia exist in spatially heterogeneous environments that also exhibit temporal variations. The presence of spatial hetero-

geneity plays an essential role in the evolution and function of microbial species [78–82] and has profound effects on biofilm formation and development [4, 69, 83, 84]. Concentration gradients in key nutrients due to limited diffusion establish metabolic niches within the biofilm that can produce spatial variations in biomass density [85] and additionally spatial partitioning of species in the case of multispecies biofilms [84, 86]. Quantitative understanding of the relationships between spatial and temporal variations in the extracellular environment and community metabolism is critical to systematically analyze and rationally manipulate biofilm consortia. While spatiotemporal metabolic models that account for both spatial and temporal variations in the extracellular environment have been constructed, these models rely on table lookups of precomputed flux balance solutions [87–89] or lattice based descriptions of nutrient diffusion [90, 91].

The second approach considers heterogeneity in the system based on spatial and temporal variations in the available nutrients. This methodology is based on combining genome-scale reconstructions with fundamental transport equations that capture the relevant convective [92] and/or diffusional [93] processes. We applied this methodology to develop biofilm metabolic models that predict the complex spatiotemporal behavior of multispecies systems associated with chronic wounds, hot lake microbial mats and *Clostridium difficile* infections. The modeling framework helped to understand the spatial arrangements of the species in the biofilm based on nutrient niches.

1.4 Thesis organization

The modeling frameworks developed in this thesis have been used in following studies:

1. Chen, Jin, Jose A. Gomez, Kai Höffner, **Poonam Phalak**, Paul I. Barton, and Michael A. Henson. "Spatiotemporal modeling of microbial metabolism." *BMC systems biology* 10, no. 1 (2016): 21.

2. **Phalak, Poonam**, Jin Chen, Ross P. Carlson, and Michael A. Henson. "Metabolic modeling of a chronic wound biofilm consortium predicts spatial partitioning of bacterial species." *BMC systems biology* 10, no. 1 (2016): 90.

3. Henson, Michael, and **Poonam Phalak**. "Byproduct cross feeding and community stability in an *in silico* biofilm model of the gut microbiome." *Processes* 5, no. 1 (2017): 13.

4. Henson, Michael A., and **Poonam Phalak**. "Microbiota dysbiosis in inflammatory bowel diseases: *in silico* investigation of the oxygen hypothesis." *BMC systems biology* 11, no. 1 (2017): 145.

5. Carlson, Ross P., Ashley E. Beck, **Poonam Phalak**, Matthew W. Fields, Tomas Gedeon, Luke Hanley, William R. Harcombe, Michael A. Henson, and Jeffrey J. Heys. "Competitive resource allocation to metabolic pathways contributes to overflow metabolisms and emergent properties in cross-feeding microbial consortia." *Biochemical Society Transactions* 46, no. 2 (2018): 269-284.

6. Henson, Michael A., and **Poonam Phalak**. "Suboptimal community growth mediated through metabolite crossfeeding promotes species diversity in the gut microbiota." *PLoS computational biology* 14, no. 10 (2018): e1006558.

7. **Phalak, Poonam**, and Michael A. Henson. "Metabolic Modeling of *Clostridium difficile* Associated Dysbiosis of the Gut Microbiota." *Processes* 7, no. 2 (2019): 97.

8. Henson, Michael A., Giulia Orazi, **Poonam Phalak**, and George O'Toole. "Metabolic Modeling of Cystic Fibrosis Airway Communities Predicts Mechanisms of Pathogen Dominance." *mSystems* 4:e00026 (2019)-19.

9. **Phalak, Poonam**, and Michael A. Henson. "Metabolic Modeling of Chronic Wound Microbiota Predicts Mutualistic Interactions that Drive Community Composition." *submitted*.

10. **Phalak, Poonam**, Hans C. Bernstein, Stephen R. Lindemann, Ryan S. Renslow, Dennis G. Thomas, Michael A. Henson and Hyun-Seob Song. "Modeling of Spatiotemporal Metabolic Interactions in Autotroph-Heterotroph Consortia." *in preparation*.

This thesis comprises of detailed description of the biofilm metabolic modeling of chronic wounds, *C. difficile* infections and environmental biofilms. In chapter 2, the general biofilm modeling framework is described and it is applied to study two species biofilms associated with chronic wounds. Various interactions between the considered species are modeled. The model predicted the spatial partitioning and maximum possible biofilm thicknesses based on these interactions. In chapter 3, the developed biofilm framework is extended to study the interspecies interactions between a photoautotroph and heterotroph community. The core metabolic models for considered autotrophs and pan-genome model for heterotrophs are developed using KBase. The biofilm model is validated by using experimental data. This model is used to study interspecies interactions under extreme environmental conditions. In chapter 4, the biofilm modeling framework is extended to study the biofilms associated with *C. difficile* infections. The biofilm model consisted of 3 species representing three most common phyla and the pathogen *C. difficile*. This model is used to analyze the healthy vs dysbiosis gut conditions during *C. difficile* infections. In chapter 5, chronic wound community comprising of 12 most abundant species is studied. This modeling framework is used to find out mutualistic relationships within the pathogens and between pathogen and commensal species.

CHAPTER 2

METABOLIC MODELING OF A CHRONIC WOUND BIOFILM CONSORTIUM PREDICTS SPATIAL PARTITIONING OF BACTERIAL SPECIES

2.1 Introduction

The aerobe *Pseudomonas aeruginosa* and the facultative anaerobe *Staphylococcus aureus* are two bacteria commonly isolated from chronic wound biofilm infections [56, 60, 65]. The same two bacteria are often key contributors to multispecies infections that occur in the lung mucous of cystic fibrosis patients [94]. *P. aeruginosa* is known to exhibit much lower growth rates than *S. aureus* and other facultative anaerobes in anaerobic environments common in chronic wound and mucoid biofilms [95, 96]. Perhaps partially in response to this metabolic disadvantage, *P. aeruginosa* has evolved a number of mechanisms to enhance its competitiveness in multispecies biofilm communities.

The most widely studied mechanism is growth inhibition and lysis of competing bacteria through the secretion of an arsenal of small molecule (e.g. pyocyanin [97]) and protein (e.g. bacteriocins [98]) toxins. The consumption of metabolic byproducts secreted by other bacteria through cross feeding mechanisms also has been proposed to enhance *P. aeruginosa* competitiveness [99]. Another putative mechanism is *P. aeruginosa* chemotaxis towards high oxygen niches (i.e. aerotaxis [100]) where it is metabolically competitive.

This work is published as: Phalak, Poonam, Jin Chen, Ross P. Carlson, and Michael A. Henson. "Metabolic modeling of a chronic wound biofilm consortium predicts spatial partitioning of bacterial species." *BMC systems biology* 10, no. 1 (2016): 90.

The biofilm models were formulated for *P. aeruginosa* and/or *S. aureus* metabolism. We developed an effective computational method for solving the biofilm models, which consisted of a set of partial differential equations with mixed boundary conditions constrained by embedded linear programs. The models were used to analyze the metabolic differences between single species and two species chronic wound biofilms and to investigate putative factors that could impact the physiology of the two species biofilm, including nutrient diffusion, metabolite cross-feeding, *P. aeruginosa* motility and *P. aeruginosa* mediated lysis of *S. aureus*.

2.2 Multispecies biofilm model

2.2.1 Model formulation

Biofilm models were formulated by combining genome-scale reconstructions of *P. aeruginosa* and/or *S. aureus* metabolism with uptake kinetics for available nutrients and reaction-diffusion type equations for species biomass, supplied substrates and synthesized metabolic byproducts. Single species biofilm models were formulated with either the *P. aeruginosa* or *S. aureus* reconstruction, while the two species model used both reconstructions. Diffusion was assumed to occur only in the axial direction of the biofilm such that spatial variations could be captured with a single variable z (Figure 2.1 A). For simplicity, the biofilm was assumed to have a fixed thickness W over which the nutrients diffused and cell growth occurred. Therefore, the models were most appropriate for predicting the metabolism of biofilms of a specified thickness. Both strains were assumed to consume glucose as the primary carbon source [101]. Glucose was supplied at the tissue-biofilm interface at the assumed concentration of the wound exudate, while oxygen was supplied at the biofilm-air interface at a concentration for an aqueous solution in equilibrium with atmospheric oxygen.

The *P. aeruginosa* PA01 iMO1056 reconstruction accounts for 1,056 genes, 1,030 enzymes, 833 intracellular reactions and 277 exchange reactions [102]. This recon-

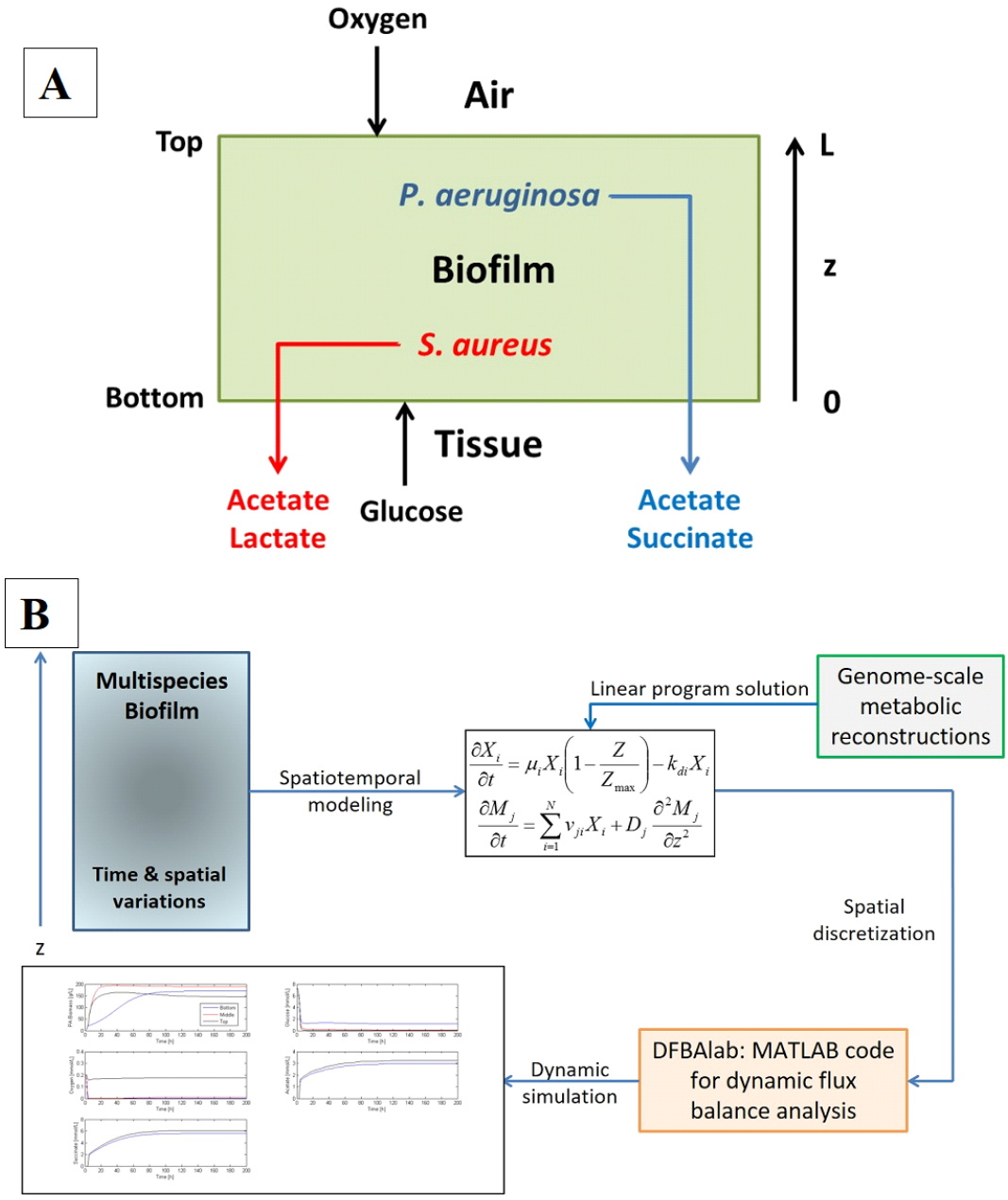

Figure 2.1: Formulation and solution of the multispecies biofilm metabolic model. (A) Schematic representation of the chronic wound biofilm model of constant thickness W with glucose provided at the tissue-biofilm interface ($z = 0$), oxygen supplied at the biofilm-air interface ($z = W$) and the metabolic byproducts acetate, succinate and lactate removed at the tissue-biofilm interface. (B) Schematic representation of the biofilm metabolic model solution procedure.

struction has been shown to provide good agreement with experimentally determined biomass yields for aerobic growth on glucose and anaerobic growth on glucose with nitrate as an electron acceptor. The preliminary flux balance calculations with a maximum growth objective showed the primary metabolic byproducts to be acetate and L-alanine. The secretion fluxes of other minor byproducts were approximately an order of magnitude less than for acetate and L-alanine. *P. aeruginosa* is known to secrete acetate, lactate and succinate [103], while the secretion of L-alanine has not been reported. To obtain byproduct distributions in better agreement with reference [103], we constrained the L-alanine secretion flux to zero. This modification resulted in a redirection of flux from L-alanine to succinate with little effect on the secretion fluxes of acetate and minor byproducts. Furthermore, we enforced a minimal non-growth associated ATP maintenance flux of 5 mmol/gDW/h, the same value as in the *S. aureus* reconstruction, to reduce the *P. aeruginosa* anaerobic growth rate for consistency with experimental studies [95]. The iMO1056 reconstruction contained succinate, lactate and acetate uptake fluxes that allowed the investigation of putative cross feeding of metabolic byproducts. Secretion of the small molecule inhibitor pycoyanin was included by adding an exchange flux with an adjustable lower bound that forced pycoyanin synthesis, which was in opposition to growth rate maximization.

The *S. aureus* N315 iMH551 reconstruction accounts for 551 genes, 604 enzymes, 682 intracellular reactions and 92 exchange reactions [104]. This model correctly reproduces byproduct secretion patterns under aerobic conditions with glucose limitation and under anaerobic conditions with glucose excess [105–109]. The flux calculations showed that the primary byproducts were acetate and lactate. The iMH551 reconstruction contained lactate and acetate uptake fluxes that allowed reassimilation of secreted metabolic byproducts. To explore the possibility of succinate cross feeding, the *S. aureus* model was modified to allow succinate uptake through a putative proton dependent symport mechanism.

Uptake kinetics were specified for the supplied substrates glucose and oxygen as well as for the possible cross-fed metabolites lactate, succinate and acetate. Although both *P. aeruginosa* and *S. aureus* are well known for their ability to perform anaerobic respiration using nitrate as an electron acceptor in place of oxygen, we have neglected the possible role of denitrification in this study. Uptake kinetics were assumed to follow standard Monod expressions of the form,

$$v_i = \frac{v_{\max,i} S_i}{K_{m,i} + S_i} \tag{2.1}$$

where v_i is the uptake rate (mmol/gDW/h) of the i-th substrate, S_i is the extracellular concentration (mmol/SL) of the i-th substrate, $v_{\max,i}$ is the maximum uptake rate and $K_{m,i}$ is the half saturation constant. Equation (2.1) was used to establish transport bounds on the uptake rates with the actual uptake rates being determined by solution of the intracellular flux balance problem. Both $v_{\max,i}$ and $K_{m,i}$ were important parameters due to the large nutrient spatial gradients induced by diffusion through the biofilm.

Mass balances on the two species have the form,

$$\frac{\partial X(z,t)}{\partial t} = \mu_X X \left(1 - \frac{Z}{Z_{\max}}\right) - k_{dX} X + k_A \left(1 - \frac{Z}{Z_{\max}}\right) \frac{\partial}{\partial t}(X \frac{\partial O}{\partial z}) \tag{2.2}$$

$$\frac{\partial X(0,t)}{\partial z} = 0 \ , \ \frac{\partial X(W,t)}{\partial z} = 0$$

$$\frac{\partial Y(z,t)}{\partial t} = \mu_Y Y \left(1 - \frac{Z}{Z_{\max}}\right) - k_{dY} Y - k_L P Y \tag{2.3}$$

$$\frac{\partial Y(0,t)}{\partial z} = 0 \ , \ \frac{\partial Y(W,t)}{\partial z} = 0$$

where X and Y are the biomass concentrations (g/L) of *P. aeruginosa* and *S. aureus*, respectively, $Z = X+Y$ is the total biomass concentration, and μ_X and μ_Y are

the corresponding growth rates (h^{-1}) obtained from the flux balance calculations. If local nutrient concentrations became too small to meet the ATP maintenance demand of a species, then the flux balance problem for the species became infeasible at that location. Once an infeasibility was detected, the death rate constant k_{dX} or k_{dY} was exponentially increased from zero to a fixed, non-zero value to simulate that the species would begin to die at that location. This approach ensured that the model equations remained smooth and could be integrated. *P. aeruginosa* has flagella for motility and can aerotaxis towards higher oxygen levels [100]. This capability was captured in the model by including a typical chemotaxis term [110] where O is the oxygen concentration (mmol/L) and k_A is the aerotaxis rate constant. Cell growth was restricted to a maximum cell concentration $Z_{\max}$ to account for cell crowding effects within the biofilm. No flux boundary conditions were imposed at the tissue-biofilm ($z = 0$) and biofilm-air ($z = W$) interfaces under the assumption that cells could not leave the biofilm via mechanisms such as dispersal.

P. aeruginosa secretes pyocyanin and other small molecules that are known to inhibit and lyse of competing bacteria such as *S. aureus* [111]. This lysis mechanism was included in the model through a pyocyanin concentration (P, mmol/L) dependent death term with rate constant k_L in the *S. aureus* mass balance in Equation (2.3). Pyocyanin synthesis by *P. aeruginosa* and diffusion through the biofilm was captured with the mass balance,

$$\frac{\partial P(z,t)}{\partial t} = v_P X + D_P \frac{\partial^2 P}{\partial z^2} \tag{2.4}$$
$$D_i \frac{\partial P(0,t)}{\partial z} = k_{m,P}[P_b - P(0,t)] \ , \ \frac{\partial P(W,t)}{\partial z} = 0$$

where v_P is the specific pyocyanin synthesis rate obtained from the flux balance calculation and D_P is the pyocyanin diffusion coefficient. A no flux boundary condition was imposed at the biofilm-air interface assuming that the pyocyanin was non-volatile. By contrast, a Robin boundary condition was imposed at the tissue-biofilm

interface to describe possibly mass transfer limited removal of pyocyanin, where $k_{m,P}$ is pyocyanin mass transfer coefficient and P_b is the bulk pyocyanin concentration in the tissue.

The glucose and oxygen mass balances were formulated under the assumptions that oxygen gas-liquid mass transfer was fast compared to oxygen uptake and that metabolites had negligible volatilities:

$$\frac{\partial G(z,t)}{\partial t} = v_{GX}X + v_{GY}Y + D_G\frac{\partial^2 G}{\partial z^2} \tag{2.5}$$
$$-D_G\frac{\partial G(0,t)}{\partial z} = k_{mG}[G_b - G(0,t)]\ ,\ \frac{\partial G(W,t)}{\partial z} = 0$$

$$\frac{\partial O(z,t)}{\partial t} = v_{OX}X + v_{OY}Y + D_O\frac{\partial^2 O}{\partial z^2} \tag{2.6}$$
$$\frac{\partial O(0,t)}{\partial z} = 0\ , D_O\frac{\partial O(W,t)}{\partial z} = k_{mO}[O_b - O(W,t)]$$

where G is the glucose concentration (mmol/L), the *P. aeruginosa* uptake fluxes v_{GX} and v_{OX} and the *S. aureus* uptake fluxes v_{GY} and v_{OY} were obtained from the flux balance calculations, and D_G and D_O are the glucose and oxygen diffusion coefficients. For glucose, a no flux boundary condition was imposed at the biofilm-air interface assuming glucose was not volatile and a Robin type boundary condition was imposed at the tissue-biofilm interface to model possibly mass transfer limited transport of glucose into the biofilm. Here k_{mG} is the glucose mass transfer coefficient and G_b is the bulk glucose concentration in the wound exudate. For oxygen, Robin type boundary conditions were imposed at both interfaces with oxygen mass transfer coefficient k_{mO}, oxygen concentration O_b at the tissue-biofilm interface and oxygen concentration O_a at the biofilm-air interface.

Mass balances on the three primary metabolic byproducts had the form,

$$\frac{\partial M_j(z,t)}{\partial t} = v_{M_jX}X + v_{M_jY}Y + D_{M_j}\frac{\partial^2 M_j}{\partial z^2} \tag{2.7}$$
$$-D_i\frac{\partial M_j(0,t)}{\partial z} = k_{m,j}[M_{b,j} - M_j(0,t)] \ , \ \frac{\partial M_j(W,t)}{\partial z} = 0 \ ,$$

where M_j is concentration (mmol/L) of the j-th byproduct (A = acetate, S = succinate, L = lactate), the secretion/consumption fluxes v_{M_JX} and v_{M_JY} were obtained from the flux balance calculations and D_{M_j} is the diffusion coefficient. No flux boundary conditions were imposed at the biofilm-air interface, while Robin type boundary conditions were imposed at the tissue-biofilm interface to allow removal of the byproducts. All biofilm diffusion coefficients were assumed to depend on the total biomass concentration Z such that diffusion was reduced in more dense regions of the biofilm [112].

2.2.2 Model parameters

We found a dearth of literature for determining species specific values for the 20 parameters needed to calculate uptake rates with respect to the five possible nutrients (glucose, oxygen, succinate, lactate, acetate). Consequently, the two species were assumed to have the same uptake parameter values. We used representative glucose [113, 114] and oxygen [114, 115] uptake parameter values reported for the model bacterium Escherichia coli under the assumption that *P. aeruginosa* and *S. aureus* should have similar values. Because we were not able to find reliable uptake parameter values for succinate, lactate and acetate, the associated $v_{\max}$ and K_m values were assumed to be equal to those for glucose (Table 2.1). Therefore, results focused on differences in metabolic network structure of the two species and not on differences in uptake properties.

Other parameter values for the biofilm model were obtained from the literature to the extent possible (Table 2.2). We utilized a typical biofilm thickness W=80μm and assumed wound exudate concentrations consistent with published values. The

Table 2.1: Nominal nutrient uptake parameters

Nutrient	$v_{\max}$	k_m
Glucose	10 mmol/gDW/h	0.5 mmol/L
Oxygen	20 mmol/gDW/h	0.003 mmol/L
Succinate	10 mmol/gDW/h	0.5 mmol/L
Lactate	10 mmol/gDW/h	0.5 mmol/L
Acetate	10 mmol/gDW/h	0.5 mmol/L

air oxygen concentration O_a was derived from the oxygen content of atmospheric air. *P. aeruginosa* and *S. aureus* cell death were implemented by exponentially increasing the death rate constants from zero to the values listed in Table 2.2 when local nutrient concentrations were not sufficient to meet ATP maintenance demands. The lower bound on the *P. aeruginosa* pyocyanin synthesis flux $v_{P,min}$ was tuned such that the average pyocyanin concentration within the biofilm was the same order of magnitude as that observed experimentally in [116]. The *S. aureus* inhibitor-mediated death constant k_L was tuned to achieve reasonable spatial distributions of the two species, which included *P. aeruginosa* dominance in the aerobic region of the biofilm, *S. aureus* dominance in the anaerobic region and a sharp spatial division between the two species [86, 117–119].

The maximum achievable biomass concentration $Z_{\max}$ was chosen to be within the large range of published values [85]. We established reasonable metabolite concentrations within the biofilm by adjusting a single mass transfer coefficient for glucose, acetate, succinate, lactate and pyocyanin such that their average concentrations were the same order of magnitude as those observed experimentally in [116] and [120] . The *P. aeruginosa* aerotaxis rate constant k_A was chosen such that *P. aeruginosa* was dominant in the aerobic region of the biofilm and a sharp spatial division between the two species was established as the biofilm matured towards a steady-state condition [82, 86, 124]. Initial conditions for each simulation were generated by first running a simulation with each species biomass concentration constrained to be 1 g/L

Table 2.2: Nominal model parameter values

Parameter	Description	Value	Reference
W	Biofilm thickness	80 μm	Specified
G_b	Bulk glucose concentration	7.5 mmol/L	[120]
O_a	O_2 conc. at the biofilm-air interface	0.21 mmol/L	[121]
O_b	O_2 conc. at the tissue-biofilm interface	0 mmol/L	Specified
S_b	Bulk succinate concentration	0 mmol/L	Specified
A_b	Bulk acetate concentration	0 mmol/L	Specified
L_b	Bulk lactate concentration	1 mmol/L	[120]
P_b	Bulk pyocyanin concentration	0 mmol/L	Specified
k_{dX}, k_{dY}	Death rate constants	0-0.01 h^{-1}	Calculated
k_L	Pyocyanin-associated death rate constant	0.4 mmol/gDW/h	Specified
k_{dP}	Pyocyanin flux bound	0.1 L/mmol/h	Specified
$Z_{\max}$	Maximum biomass concentration	200 g/L	[85]
X_0, Y_0	Initial biomass concentrations	1 g/L	Specified
k_A	Aerotaxis rate constant	5 x10^{-8} cm^2. L/mmol. s	Specified
D_G	Aq. diffusion coefficient for glucose	9.4x10^{-6} cm^2/s	[122]
D_O	Aq. diffusion coefficient for oxygen	26.8x10^{-6} cm^2/s	[122]
D_A	Aq. diffusion coefficient for acetate	16.2x10^{-6} cm^2/s	[122]
D_S	Aq. diffusion coefficient for succinate	12.6x10^{-6} cm^2/s	[122]
D_L	Aq. diffusion coefficient for lactate	12.1x10^{-6} cm^2/s	[123]
D_P	Aq. diffusion coefficient for pyocyanin	7.2x10^{-6} cm^2/s	Specified
$k_{m,i}$	Mass transfer coefficient	2x10^{-4} cm/s	Specified
$k_{m,O}$	Oxygen mass transfer coefficient	2x10^{-2} cm/s	Specified

and capturing the resulting steady-state solution. These initial conditions reflected a newly developed, nearly spatially homogeneous biofilm with small cell densities, high nutrient levels and low byproduct concentrations.

2.2.3 Model solution

The two species biofilm model consisted of a set of partial differential equations (PDEs) with mixed boundary conditions and embedded linear programs (LPs). The efficient and stable solution of such models is a challenging problem at the forefront of microbial metabolic modeling [125]. As described in our previous publications [92, 93], we pursued a spatial discretization approach based on converting the PDEs into a large set of ordinary differential equations (ODEs) in time with embedded LPs (Figure 2.1 B). The spatial domain $[0, W]$ was discretized using $N = 50$ node points at which the diffusion terms in Equations (2) - (7) were discretized using central difference approximations with second-order accuracy. The specified boundary conditions were incorporated into the central difference approximations at the boundary node points. This procedure yielded a set of 8 ODEs at each node point for the local concentrations of *P. aeruginosa* and *S. aureus* biomass, glucose, oxygen, acetate, succinate, lactate and pyocyanin.

This ODE system was solved using DFBAlab [126], a MATLAB tool that explicitly addresses problems associated with LP alternative optima and possible infeasibilities [127]. DFBAlab employs a lexicographic optimization strategy in which a series of LP problems are sequentially solved to ensure the determination of unique exchange fluxes necessary for a well-defined dynamic system. Each LP is solved subject to constraints that the previous objectives are equal to their optimal values, with the required number of LPs equal to the number of exchange fluxes. We specified the lexicographic optimization objectives to reflect known or anticipated physiology of the two species biofilm community (Table 2.3). We found that reordering these objectives had no noticeable effect on simulation results. Each node point was represented by 8 ODEs for the local species and metabolite concentrations and 12 LPs for lexicographic optimization. We employed 50 node points such that the discretized biofilm model consisted of 400 ODEs and 600 LPs.

Table 2.3: Lexicographic optimization.

Species	Number	Direction	Objective
P. aeruginosa	1	Maximize	Growth rate
P. aeruginosa	2	Minimize	Acetate secretion
P. aeruginosa	3	Minimize	Succinate secretion
P. aeruginosa	4	Maximize	Glucose uptake
P. aeruginosa	5	Maximize	Oxygen uptake
P. aeruginosa	6	Maximize	Lactate uptake
S. aureus	1	Maximize	Growth rate
S. aureus	2	Minimize	Acetate secretion
S. aureus	3	Minimize	Lactate secretion
S. aureus	4	Maximize	Glucose uptake
S. aureus	5	Maximize	Oxygen uptake
S. aureus	6	Maximize	Succinate uptake

All simulations were performed with MATLAB 8.5 (R2015a) using DFBAlab, the stiff MATLAB integrator ode15s for dynamic flux balance model solution and Gurobi 6.0 for linear program solution. A typical 1000-hour dynamic simulation for determining a steady-state solution required about 25 minutes running on an ASUS computer with Intel Core i7-960 processor and 24 GB RAM. As compared to alternative computational methods for spatiotemporal metabolic modeling based on table lookups of precomputed FBA solutions combined with integration of the PDEs on a coarse spatial grid [87–89] and real-time FBA solution combined with lattice-based descriptions of metabolite diffusion [90, 91], we believe our approach offers several important advantages including the use of DFBAlab, the ability to directly embed LPs within the discretized ODEs, and the flexibility to solve the ODE-LP system using stiff integrators with variable step size and error control.

2.3 Results and discussion

2.3.1 Metabolism of single species and multispecies biofilms

We first performed simulations for single species biofilms consisting of only *P. aeruginosa* or *S. aureus*. Initial conditions were chosen to reflect a nearly spatially homogeneous biofilm with low cell densities $X(z,0) = 1$ g/L or $Y(z,0) = 1$ g/L. For each species, biofilms of different thicknesses were simulated to determine the maximum thickness $W_{\max}$ that could be sustained according to the model. If the biomass concentration was below 10 g/L (5% of the maximum value $Z_{\max} = 200$ g/L) anywhere in the mature biofilm obtained after 1000 hours of simulation, the thickness was deemed too large and reduced. These simulations revealed that *S. aureus* could grow much thicker biofilms with $W_{\max} = 90$ μm compared to *P. aeruginosa* with $W_{\max} = 30$ μm, mainly due to superior *S. aureus* anaerobic growth rates.

Dynamic simulations were performed for two species biofilms consisting of *P. aeruginosa* and *S. aureus* using eight different hypothetical scenarios. Scenario 1 was the base case where the two bacteria competed for glucose and oxygen in the absence of byproduct crossfeeding, *P. aeruginosa* aerotaxis or pyocyanin-mediated lysis of *S. aureus*. We found the two species $W_{\max} = 80$ μm, which was slightly less that the *S. aureus* $W_{\max} = 90$ μm but substantially larger than the *P. aeruginosa* $W_{\max} = 30$ μm. The two species $W_{\max}$ was a linear combination of the single species $W_{\max}$ values weighted by the average biomass concentrations in the two species biofilm.

When the two species biofilm thickness was set equal to $W_{\max} = 80$ μm, pseudo steady-state solutions were obtained after only 50 hours of simulation (Figure 2.2A). These results are in-line with many experimental studies [128, 129]. Oxygen was quickly depleted throughout most of the biofilm, except near the biofilm-air interface where an aerobic region was established as observed experimentally [130]. Similarly, glucose was rapidly depleted in all regions except near the tissue-biofilm interface where a glucose rich region was maintained. *S. aureus* was predicted to quickly estab-

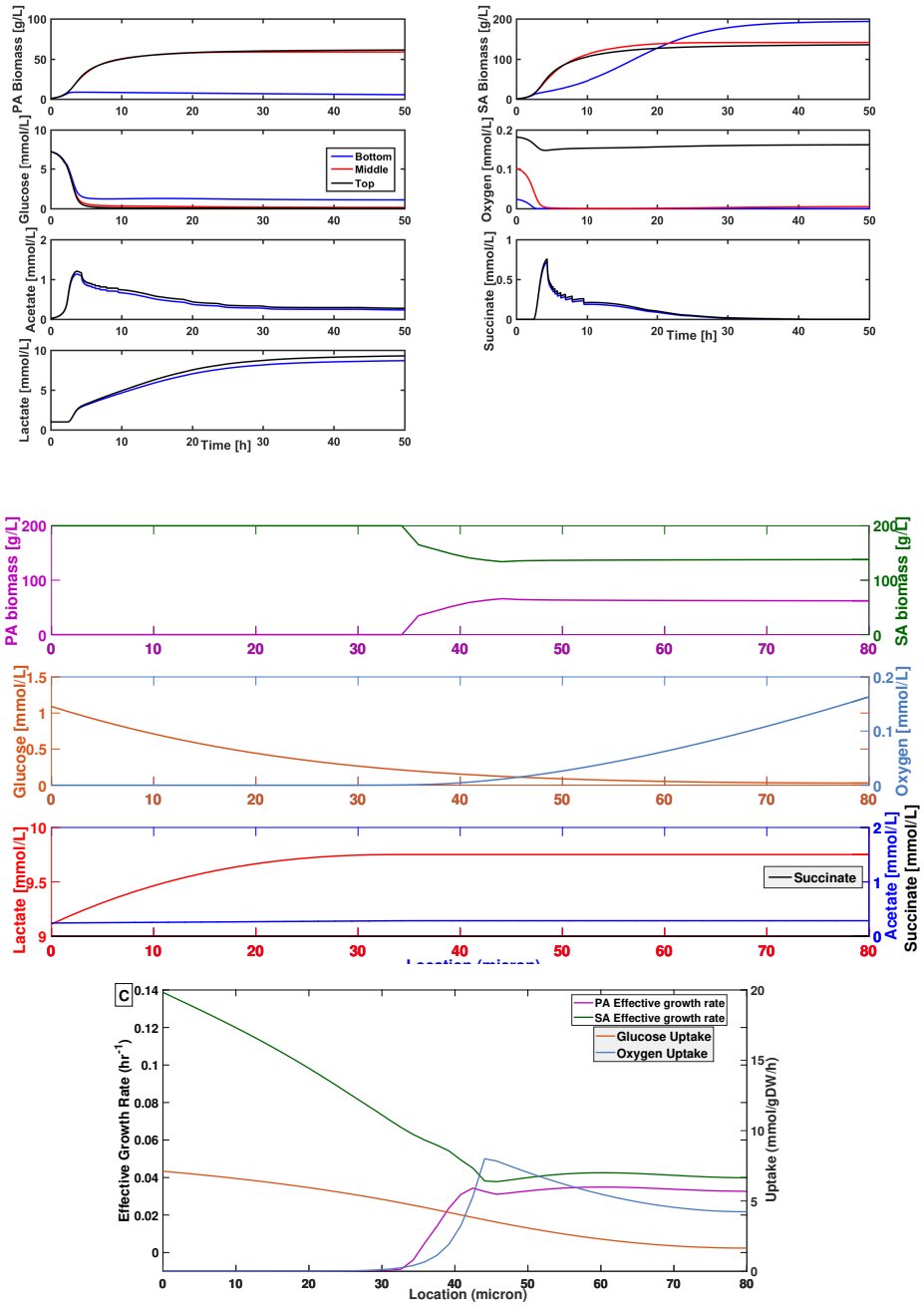

Figure 2.2: Predictions for a two species biofilm of thickness W = 80 μm (Base case scenario). (a) Time resolved predictions over the first 50 hours at the bottom, middle and top of the biofilm. (b) Spatially resolved biomass and metabolite concentration predictions after 1000 hours. (c) Spatially resolved effective growth and uptake rate predictions after 10 hours.

lish dominance throughout the biofilm due to its higher local growth rates, especially in the anaerobic region. Initially acetate and succinate levels increased but thereafter they were predicted to decrease due to metabolite removal at the tissue-biofilm boundary. Lactate levels were predicted to remain high throughout the biofilm due to *S. aureus* synthesis in the anaerobic region and diffusion into the aerobic region. Multispecies biofilm spatial profiles obtained after 1000 hours of simulation (Figure 2.2) were characterized by the presence of a glucose rich, anaerobic region near the tissue-biofilm interface and a glucose depleted, aerobic region near the biofilm-air interface. *S. aureus* was predicted to be dominant throughout the biofilm, especially in the anaerobic region, while *P. aeruginosa* was predicted to be present only in the aerobic region. Byproduct profiles were similar to those obtained for the *S. aureus* single species biofilm (not shown here) with high lactate levels, low acetate levels and no succinate production. We attributed this behavior to partitioning of *P. aeruginosa* to the aerobic region where the synthesis of byproducts was substantially reduced. These model predictions could be experimentally tested by measuring metabolite concentration profiles using spatially resolved metabolomics [131–133] and gene expression profiles using spatially revolved transcriptomics [134, 135].

To further analyze how multispecies metabolism depended on position in the biofilm, local effective growth rates and nutrient uptake rates were determined from the base case (BC) simulation data. For species i, the local effective growth rate was calculated as the difference between the biomass restricted growth rate $\mu_i(1-Z_i/Z_{\max})$ and the energy associated death rate k_{di} at a given position z. Consequently, the effective growth rate could be negative in nutrient lean regions. The calculations were performed using data collected at $t = 10$ hours because these initial rates offered insights into biofilm physiology. *S. aureus* growth rates exceeded *P. aeruginosa* growth rates at all positions, especially in the anaerobic region near the bottom of the biofilm where *P. aeruginosa* death was predicted (Figure 2.2C). Both species were predicted

to have constant growth rates in the upper aerobic region. The *P. aeruginosa* growth rate decreased rapidly in the lower half due to decreasing oxygen availability such that death occurred in the first 35 μm. By contrast, the *S. aureus* growth rate increased rapidly in this region due to the increasing availability of glucose to support anaerobic growth. As time progressed, these local growth rates resulted in *S. aureus* dominance throughout the biofilm and *P. aeruginosa* presence only in the aerobic region (Figure 2.2B). The glucose uptake rate increased monotonically from bottom to top of the biofilm, while the oxygen uptake rate was predicted to exhibit a maximum near the center because that location offered the optimal combined availability of glucose and oxygen to support consortium growth. The experimental determination of spatially resolved biomass concentrations [136] would be beneficial in this context.

2.3.2 Byproduct cross feeding

Cross feeding of secreted metabolic byproducts is common in bacterial communities [137, 138] and multispecies biofilms [139, 140]. For example, a cross feeding mechanism has been proposed for a polymicrobial infection system consisting of the two facultative anaerobes Aggregatibacter actinomycetemcomitans and Streptococcus gordonii [139]. We hypothesized that cross feeding of secreted metabolic byproducts (lactate, succinate, acetate) would enhance the competitiveness of *P. aeruginosa* in the aerobic portion of the biofilm. Except for the inability of *S. aureus* to consume acetate, experimental studies as well as our previously reported FBA results [141] show that the two species are capable of metabolizing these byproducts in the presence of sufficient oxygen. Therefore, we investigated the impact of putative cross feeding by allowing each species to enhance its growth through uptake of the three byproducts (C-f scenario). The two species were assumed to uptake each byproduct with the same kinetics (see Table 2.2) due to lack of data on species and substrate specific uptake parameters.

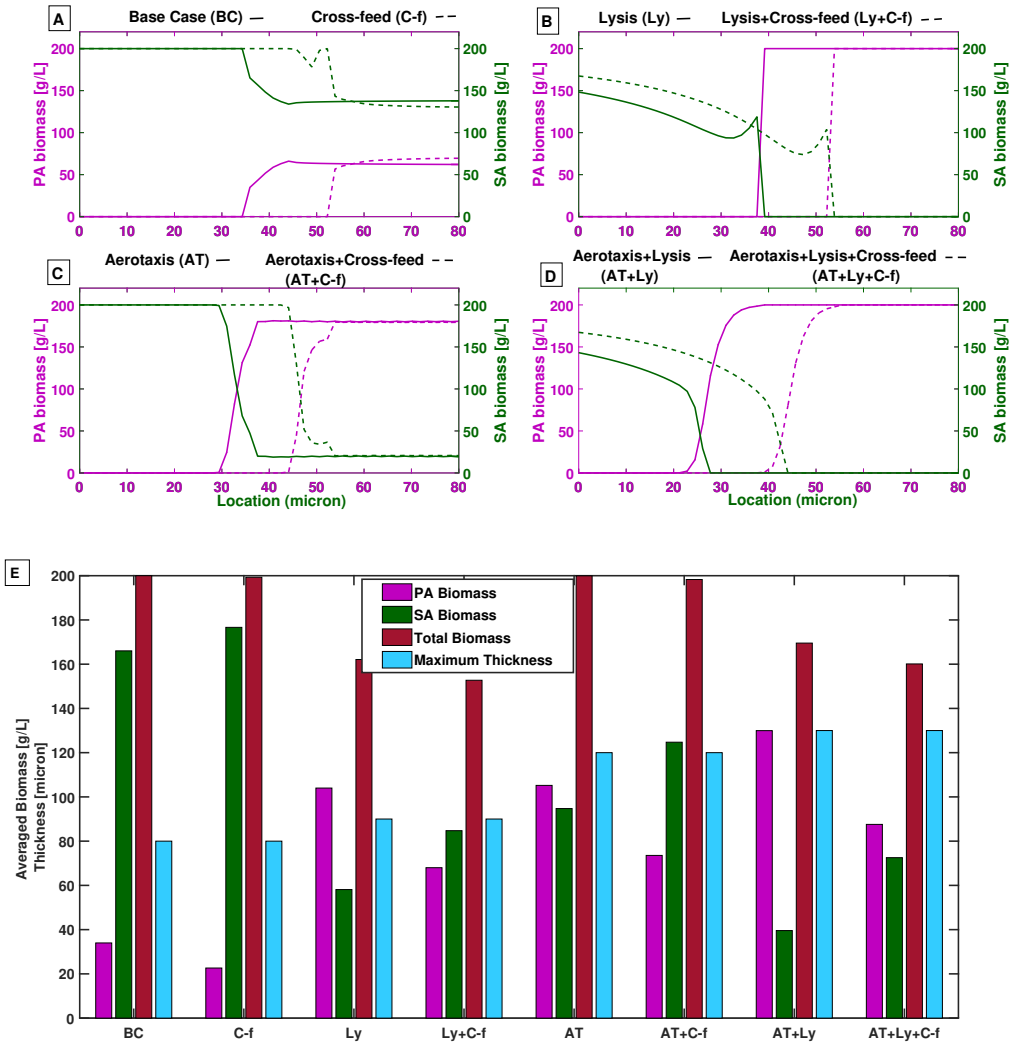

Figure 2.3: Predictions after 1000 hours for two species biofilms of thickness W = 80 μm with different species interaction mechanisms. (a)(A-D) Spatially resolved biomass concentrations and (E) *P. aeruginosa* (Pa), *S. aureus* (Sa), total biomass concentrations averaged across the biofilm and maximum thickness for the eight considered scenarios.

The cross-feed scenario model predicted that $W_{\max}$ remained 80 μm when byproduct cross feeding was incorporated. Because glucose was the more energetically favorable carbon source, most of the available oxygen was used for glucose oxidation and little oxygen remained for lactate oxidation. Contrary to our hypothesis, cross-feeding reduced the region where *P. aeruginosa* was present and did not substantially increase the *P. aeruginosa* biomass concentration within this region (Figure 2.3, panel A). To succinctly quantify this behavior, the *P. aeruginosa* and *S. aureus* biomass concentrations were averaged across the biofilm and compared to average concentrations obtained for the base case scenario without cross feeding. While the total biomass concentration was not affected, cross-feeding increased the fraction of *S. aureus* relative to *P. aeruginosa* (Figure 2.3E). Since lactate was the primary byproduct of the two species biofilm, we attributed this behavior to *S. aureus* having more efficient lactate metabolism. Previously reported single species FBA results showed that *S. aureus* had higher growth rates on lactate under oxygen sufficient and oxygen limited conditions [141]. Because similar behavior was observed for glucose metabolism in single species biofilms, the addition of lactate consumption was predicted to further increased *S. aureus* dominance in the aerobic region where sufficient oxygen was available for lactate oxidation.

Byproduct cross feeding in *P. aeruginosa/S. aureus* chronic wound biofilms has not been experimentally studied to our knowledge and represents a promising area of research. Experimental studies with *P. aeruginosa* biofilms in the cystic fibrosis lung show that lactate actually can be a preferred carbon source to glucose [142, 143], suggesting enhanced lactate uptake capabilities. This environmental dependence emphasizes the importance of conducting uptake experiments and studying cross feeding under chronic wound relevant conditions. Well controlled planktonic growth experiments are needed to accurately estimate ATP maintenance demands of the two

species, since lactate oxidation might confer a growth advantage to *P. aeruginosa* if the energetics are more favorable than those modeled.

2.3.3 *P. aeruginosa* inhibition of *S. aureus*

P. aeruginosa secretes a wide variety of inhibitory compounds that have been shown to enhance its competitiveness against competing bacteria in multispecies biofilm communities [144–146]. *P. aeruginosa* is known to secrete pyocyanin which inhibit and lyse competing bacteria such as *S. aureus*. Additional simulations were performed to explore the impact of a putative pyocyanin-mediated lysis mechanism on the two species biofilm. When this mechanism was combined with nutrient competition (Ly scenario), the model predicted that $W_{\max}$ was slightly increased to 90 μm. Reduction of *S. aureus* biomass in the anaerobic region resulted in slightly higher glucose levels throughout the biofilm, allowing increased *P. aeruginosa* growth in the upper aerobic region and a greater biofilm thickness.

To allow direct comparison with the other species interaction scenarios, simulations also were performed for an 80 μm thick biofilm. Spatial profiles showed sharp partitioning of the two species with *P. aeruginosa* dominant in the upper aerobic region of the biofilm (Figure 2.3, panel C). This effect was achieved at the expense of the *S. aureus* biomass concentration, which was substantially reduced in the lower anaerobic region and dropped to zero at 40 μm.

The metabolic burden of synthesizing pyocyanin was predicted to have a minimal effect on *P. aeruginosa* growth due to the small enforced bound of 0.1 mmol/gDW/h. At a maximum glucose uptake rate of 10 mmol/gDW/h, only 2.2% of available carbon was used for pyocyanin synthesis. While we tuned our model to obtain reasonable extracellular pyocyanin concentrations [117], key parameters (i.e. synthesis rate, diffusion coefficient, killing rate) associated with the mechanism are unknown and need

to be experimentally determined to accurately quantify the effect in chronic wound environments.

Combining byproduct cross feeding and the lysis mechanism (Ly+C-f scenario) did not change $W_{\max}$ from the pyocyanin-free case (C-f scenario) but did increase *S. aureus* competitiveness by shifting the location where the species partitioned approximately 15 μm towards the biofilm-air interface (Figure 2.3, panel B). The addition of cross feeding resulted in average biomass concentrations that were roughly equal, while total biomass was reduced (Figure 2.3E). We hypothesized that this unexpected effect was due to increased oxygen utilization by *S. aureus* for lactate oxidation. Although *S. aureus* biomass was simultaneously reduced by pyocyanin- mediated lysis, the oxygen used for *S. aureus* growth was not available for *P. aeruginosa* oxidative growth and total biomass decreased. Therefore, the pyocyanin mechanism was interpreted as an antagonistic mechanism by which *P. aeruginosa* increased its own competitiveness.

2.3.4 *P. aeruginosa* aerotaxis

P. aeruginosa has a single flagellum that may allow motility in complex, heterogeneous environments such as biofilms [147] while *S. aureus* is generally viewed as non-motile [148]. More specifically, *P. aeruginosa* has been observed to chemotax towards higher oxygen environments, a process known as aerotaxis, which offer more favorable growth conditions [100]. To explore the impact of this putative aerotaxis mechanism on two species biofilm metabolism, the *P. aeruginosa* biomass equation included a chemotaxis term (see Equation 2.2) and simulations were performed with both nutrient competition and aerotaxis (AT scenario). The energy requirements for chemotaxis were assumed negligible compared to growth. When aerotaxis was combined with nutrient competition, the model predicted that $W_{\max}$ was increased to 120 μm and nearly complete species partitioning as observed experimentally [86, 149], with *P. aeruginosa* dominant in the upper aerobic half and only *S. aureus* present

in the lower anaerobic region. Aerotaxis increased spatial partitioning of the two species (see Figure 2.3, panel C) such that *P. aeruginosa* had access to more oxygen for lactate respiration, resulting in a thicker biofilm.

Spatial profiles generated for an 80 μm biofilm show almost complete partitioning of the two species, with *P. aeruginosa* dominating in the upper aerobic half, only *S. aureus* present in the lower anaerobic region, and the two species coexisting for about 10 μm near the middle of the biofilm (Figure 2.3, panel C). Aerotaxis allowed *P. aeruginosa* to substantially improve its competitiveness by increasing its concentration in the upper portion of the biofilm rather than by moving the transition region between the two species (see Figure 2.2B). When averaged across the biofilm, the biomass concentrations of the two species were approximately equal while total biomass was unaffected compared to the aerotaxis-free case (Figure 2.3E). Unlike pyocyanin-mediated lysis, aerotaxis can be viewed as an antagonistic mechanism by which *P. aeruginosa* increased its own competitiveness without reducing total cell densities. Biofilm reactor experiments aimed at demonstrating and quantifying the aerotactic response would be highly beneficial. Experimental testing could be achieved through a combination of traditional and spatially resolved omics technologies [133, 134, 150].

When byproduct cross feeding was added to *P. aeruginosa* aerotaxis and nutrient competition (AT+C-f scenario), the model predicted $W_{\max} = 120$ μm, the same value obtained in the absence of cross feeding. When simulations were performed for an 80 μm thick biofilm, the addition of cross feeding substantially increased *S. aureus* biomass in the biofilm while having a small negative impact on total biomass (Figure 2.3E). Of the eight scenarios investigated, a maximum $W_{\max} = 130$ μm was predicted when nutrient competition and aerotaxis were combined with pyocyanin-mediated lysis of *S. aureus* (AT+Ly scenario). In this case, *P. aeruginosa* had access to increased glucose due to *S. aureus* death in the anaerobic region and increased lac-

tate due to the absence of *S. aureus* in the aerobic region, which combined to enhance *P. aeruginosa* growth and allow a thicker biofilm. For a nominal biofilm thickness of 80 μm, only *P. aeruginosa* was present in the upper 50 μm of the biofilm and the amount of *S. aureus* was relatively small in the lower anaerobic region (Figure 2.3, panel D). The further addition of byproduct cross feeding did not affect $W_{\max}$ but did increase *S. aureus* competitiveness (AT+Ly+C-f scenario) (Figure 2.3E). Collectively, these predictions suggest that both pyocyanin-mediated lysis and aerotaxis are potentially powerful mechanisms for *P. aeruginosa* to enhance its competitiveness in multispecies biofilms with the faster growing facultative anaerobe *S. aureus*.

2.4 Conclusions

Chronic wounds are often colonized by bacteria consortia growing as biofilms on a complex mixture of wound exudate. Improved understanding of these complex multispecies systems is required to develop more rational and effective antibiotic therapies for biofilm eradication. We developed genome-scale spatiotemporal models of a two species consortium comprised of the chronic wound isolates *Pseudomonas aeruginosa* and *Staphylococcus aureus* to investigate the impact of putative species interaction mechanisms on biofilm physiology. The models were used to analyze the metabolic differences between single species and two species biofilms and to investigate the impact of nutrient competition, byproduct cross feeding, *P. aeruginosa* inhibition of *S. aureus* growth and *P. aeruginosa* aerotaxis on the relative abundance and spatial distribution of each species. The key predictions of the computational modeling study were:

- The two species system was predicted to support a maximum biofilm thickness much greater than *P. aeruginosa* alone but slightly less than *S. aureus* alone, suggesting an antagonistic metabolic effect of *P. aeruginosa* on *S. aureus*.

- Nutrient gradients imposed by supplying glucose at the bottom and oxygen at the top of the biofilm induced spatial partitioning of the two species, with *S. aureus* most concentrated in the lower anaerobic region and *P. aeruginosa* present only in the upper aerobic region.

- When each species was allowed to enhance its growth through consumption of secreted metabolic byproducts assuming identical uptake kinetics, the competitiveness of *S. aureus* was further enhanced due to its more efficient lactate oxidative metabolism.

- Lysis of *S. aureus* by the small molecule inhibitor pyocyanin secreted from *P. aeruginosa* and/or *P. aeruginosa* aerotaxis towards high oxygen levels were predicted to enhance spatial portioning of the two species and to increase *P. aeruginosa* competitiveness in the aerobic region.

These model predictions require further validation through the execution of targeted experiments that augment existing results in the literature that support our conclusions. *P. aeruginosa* lysis of *S. aureus* combined with nutrient competition is a particularly relevant scenario for which model predictions could be tested experimentally.

CHAPTER 3

MODELING OF SPATIOTEMPORAL METABOLIC INTERACTIONS IN AUTOTROPH-HETEROTROPH CONSORTIA

3.1 Introduction

The environmental communities play an important role in production and utilization of organic matter, degradation of toxic compounds and the cycling of nitrogen, sulfur and other metals [151, 152]. The interactions between the species in community through exchanges of metabolites, scavenging of toxins shape the community structure and abundances. It is very important to understand the interspecies interactions to analyze and interpret the dynamics of community formation, the functional relationships between these species and the complex metabolic processes within the community. As a typical example, cyanobacteria and heterotrophic species in nature form stable microbial mats or biofilms by developing synergistic relationships. The cyanobacteria are photoautotrophs that convert inorganic matter with the help of light energy into useful organic compounds and oxygen, which are then consumed by the heterotrophic species in the vicinity [153]. Cyanobacteria also benefit from the presence of their partners because heterotrophs produce carbon dioxide - a major carbon source for cyanobacteria - and remove the toxins that otherwise may inhibit the growth of cyanobacteria. For controlling the dynamics of these communities, it is critical to understand how metabolic interactions between autotrophs and heterotrophs occur and, how they are constrained in space and time, and how those constraints affect community dynamics and biochemical function. Predictive mathematical models such as community metabolic networks can serve as a useful tool for this purpose.

Here, We would be using mathematical models to analyze and interpret the interactions within this community. Mathematical simulation is a useful tool to evaluate the growth and abundances of species in 3D biofilm spatial structures. The main objective of this study is to develop a mathematical model to analyze the autotrophic and heterotrophic growth, to account for interspecies interactions through metabolite exchanges and to predict spatial arrangements of the species in the biofilm. The multispecies biofilm model will be validated by using experimental data available from the study on photoautotroph-heterotroph biofilms [154]. The validated model will be used to predict the important interactions for the community stability and development of metabolic niche in the environment. The model will be a useful tool to study various autotrophic-heterotrophic interactions. It will help to engineer the specific communities like biofuel producing communities, to analyze the biogeochemical cycles in the nature and to understand the role of autotroph-heterotrophs in ecology.

3.2 Material and methods

3.2.1 System description

For model development, we chose microbial-mat-derived unicyanobacterial consortia previously studied by [154]. in which the biofilms were grown in the tissue culture flasks, the metabolomics, dry weight, composition, total protein and cell counts were measured. This study concluded that two consortia had distinct species of cyanobacteria which were primary producers along with nearly identical heterotrophs present in both the systems. The metabolomic study detected glucose in all the samples. Inorganic carbon was the sole carbon source supplied to the consortia. The biofilms were grown for 28 days under continuous photon flux of 35 μE/m^2/s. The autotroph and heterotroph biomass obtained from the published study are shown in Figure 3.1B (UCCA) and Figure 3.1C (UCCO). The study concluded that UCCA produced higher autotroph biomass as compared to UCCO.

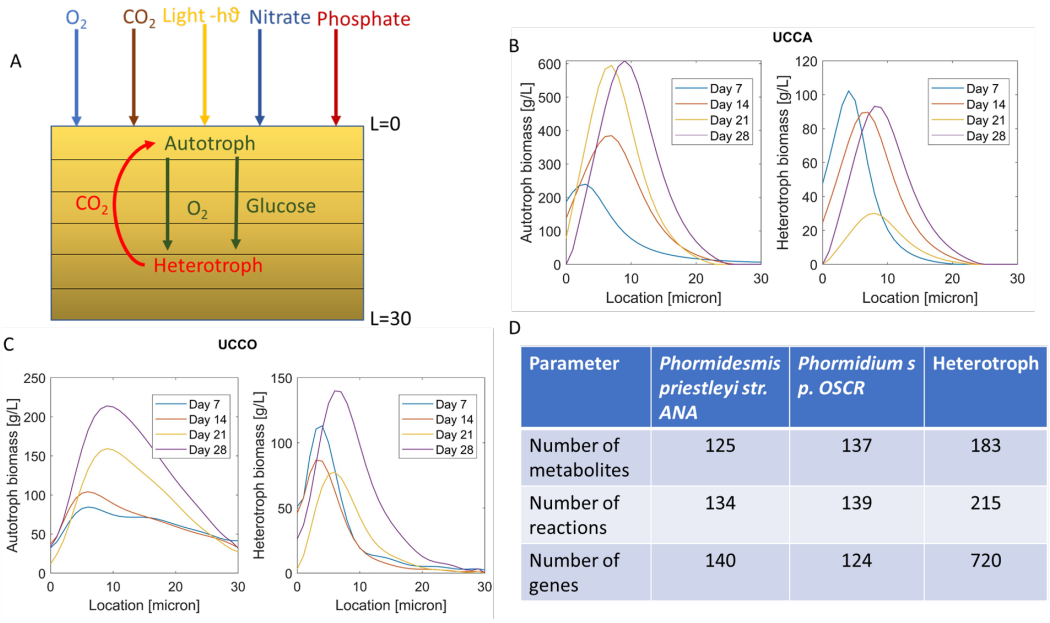

Parameter	*Phormidesmis priestleyi str. ANA*	*Phormidium s p. OSCR*	Heterotroph
Number of metabolites	125	137	183
Number of reactions	134	139	215
Number of genes	140	124	720

Figure 3.1: Formulation of the multispecies biofilm metabolic model. (A) Schematic representation of the autotroph-heterotroph biofilm model of constant thickness L with CO_2, photon, O_2, nitrate and phosphate provided at the $L = 0$ μm. (B) Experimental UCC-A autotroph and heterotroph biomass concentration (g/L) plotted at various locations in the biofilm at different time points. (C) Experimental UCC-O autotroph and heterotroph biomass concentration (g/L) plotted at various locations in the biofilm at different time points. (D) Number of reactions, metabolites and genes present in core metabolic network model of considered autotrophs and heterotroph.

3.2.2 Model formulation

The multispecies biofilm model was constructed for autotroph and heterotroph community in microbial mat derived unicyanobacterial consortia. The biofilm was assumed to be formed on the flask surface as described in previous publication [154], this interface was termed as bottom of the biofilm ($L = 30\mu$m) (Figure 3.1A). The metabolites such as inorganic carbon in the form of CO_2, O_2, nitrate and phosphate were supplied at the top of the biofilm ($L = 0\mu$m). The biofilm was assumed to be growing under constant photon incidence rate supplied at top of the biofilm. The autotrophs in the community were assumed to convert CO_2 in presence of photon energy to organic carbon (glucose) and oxygen which were consumed by heterotrophs in the community. Heterotrophs generated CO_2 as a metabolic byproduct which was consumed by autotrophs in the community. Diffusion was assumed to occur only in the axial direction of the biofilm such that spatial variations could be captured with a single variable z (Figure 3.1A). For simplicity, the biofilm was assumed to have a fixed thickness L over which the nutrients diffused, and cell growth occurred. Therefore, the models were most appropriate for predicting the metabolism of biofilms of a specified thickness.

The spatiotemporal models for photoautotroph-heterotroph consortia were constructed by combining core metabolic network models with nutrient uptake kinetics and reaction-diffusion equations for species biomass, supplied substrates and synthesizes metabolic byproducts.

The species biomass was calculated by using,

$$\frac{\partial X_i(z,t)}{\partial t} = \mu_i X_i + D_{X_i}\frac{\partial^2 X_i}{\partial z^2} \tag{3.1}$$

$$-D_i\frac{\partial X_i(0,t)}{\partial z} = k_{X_i,0}[X_{i,b} - X_i(0,t)]\ ,\ -D_i\frac{\partial X_i(L,t)}{\partial z} = k_{X_i,L}[0 - X_i(L,t)]$$

where X_i was the biomass concentration (g/L) of i-th species. μ_i is the growth rate (h^{-1}) of the i-th species. The biomass was assumed to be diffused with diffusion

coefficient (D_{X_i}) and removed from the both ends of the biofilm at the mass transfer rates ($k_{X_{i,0}}$ and $k_{X_{i,L}}$).

The metabolite concentrations (CO_2, phosphate, nitrate, glucose and oxygen) were calculated by using,

$$\frac{\partial M_j(z,t)}{\partial t} = v_{M_jX_i}X_i + D_{M_j}\frac{\partial^2 M_j}{\partial z^2} \tag{3.2}$$

$$-D_{M_j}\frac{\partial M_j(0,t)}{\partial z} = k_{mM_j}[M_{j,b} - M_j(0,t)] \ , \ -D_{M_j}\frac{\partial M_j(L,t)}{\partial z} = k_{mM_j}[0 - M_j(L,t)]$$

where M_j was the concentration (mmol/L) of j-th metabolite (CO_2, phosphate, nitrate, glucose, O_2). The uptake fluxes $v_{M_jX_i}$ of j-th metabolite for i-th species was calculated from flux balance calculations. The metabolites were assumed to be diffused at the rate of D_{M_j} and removed from the bottom of the biofilm at the mass transfer rate, k_{m,M_j}. $M_{j,b}$ was bulk concentration of the metabolite at the air-biofilm interface. We supplied CO_2, phosphate, nitrate and O_2 at the top of the biofilm and the accumulated metabolites were removed from the bottom of the biofilm.

Uptake kinetics were specified for the four primary metabolites: CO_2, photon, glucose and oxygen. The uptake kinetics for each metabolite were assumed to follow Michaelis-Menten expressions.

$$v_i = \frac{v_{\max,i}S_i}{K_{m,i} + S_i} \tag{3.3}$$

where v_i is the uptake rate (mmol/gDW/h) of the i-th substrate, S_i is the extracellular concentration (mmol/SL) of the i-th substrate, $v_{\max,i}$ is the maximum uptake rate and $K_{m,i}$ is the half saturation constant. Equation (2.1) was used to establish transport bounds on the uptake rates with the actual uptake rates being determined by solution of the intracellular flux balance problem. Both $v_{\max,i}$ and $K_{m,i}$ were important parameters due to the large nutrient spatial gradients induced by diffusion through the biofilm.

The uptake kinetics of phosphate and nitrate had the form,

$$v_p = \alpha_P \frac{v_{\max,p} P}{K_{m,p} + P} \tag{3.4}$$

$$v_n = \alpha_n \frac{v_{\max,n} N}{K_{m,n} + N} \tag{3.5}$$

where v_p and v_n are the uptake rates (mmol/gDW/h), P and N are the extracellular concentrations (mmol/L), $v_{max,p}$ and $v_{max,n}$ are the maximum uptake rates and $K_{m,p}$ and $K_{m,n}$ are the half saturation constants of the phosphate and nitrate respectively. Equations (3.4 and 3.5) were used to establish transport bounds on the uptake rates with the actual uptake rates being determined by solution of the intracellular flux balance problem. The parameters α_p and α_n were added to evaluate the effect of restricted phosphate and nitrate uptakes on biomass concentration and species interactions.

The photon incidence rate was calculated by using Beer-Lambert law,

$$I = I_{in} e^{-(k_{tot}(L-z))} \tag{3.6}$$

Where I_{in} is the initial photon incident rate (μE/m^{2}s). The attenuation coefficient, k_{tot} was adjusted to achieve enough penetration of light into the biofilm. The photon incidence rate obtained from this equation was used to calculate the lower bound on photon uptake rate by using nutrient uptake kinetics. The lower bound of photon uptake rate along with other nutrient bounds were used for solving core metabolic model and the corresponding growth rates of autotrophs were obtained.

The core metabolic network models were obtained by supplying genomes of the considered species to Kbase. Kbase platform was used to gapfill the core metabolic network models. The autotrophic cyanobacterium Phormidesmis priestleyi ANA and cyanobacterium Phormidium sp. OSCR core metabolic models were gapfilled using Kbase tool Gapfill Metabolic Model. The heterotroph model was generated by

combining genomes of most abundant species in consortia Bin 01 (Bacteriodetes), Bin18 (Rhodo), Bin10 (HL-49), Bin 04 (Plasmid), Bin 02 (HL-53) and Bin 05 (HL-91) [155]. The autotroph-1 model accounts for 140 genes, 125 metabolites and 134 reactions whereas autotroph-2 model accounts for 124 genes, 137 metabolites and 139 reactions. The core scale metabolic networks for autotrophs have been shown to provide good agreement with experimentally obtained biomass growth rates on photon and CO_2. Our preliminary flux balance calculations with maximum growth objective showed that the autotroph produced glucose and oxygen as byproducts. The heterotroph core metabolic model was examined for various glucose and oxygen uptake rates and found to be in good agreement with experimental growth rates. The major byproduct of heterotroph metabolism was CO_2.

3.2.3 Solving model equations

The biofilm model was consisting of a set of partial differential equations (PDEs) with mixed boundary conditions and embedded LPs. We converted those PDEs to ordinary differential equations (ODEs) by discretizing in space. The algebraic equation (AE) for photon balance equation combined with the ODEs led to system of differential algebraic equations (DAEs). The DAE system was solved using DFBAlab, a MATLAB tool that explicitly addresses problems associated with LP alternative optima and possible infeasibilities. DFBAlab employs a lexicographic optimization strategy in which a series of LP problems are sequentially solved to ensure the determination of unique exchange fluxes necessary for a well-defined dynamic system. We specified the lexicographic optimization objectives to reflect the anticipated physiology of the autotroph-heterotroph biofilm (Table 3.1. We used 30 spatial node points to achieve fast and accurate solutions. We solved 210 ODEs, one 1 algebraic equation for photon balance and 390 LPs in MATLAB 2017b using DFBAlab, stiff ode integrator ode15s and Gurobi 7.5.2 as a LP solver [93, 141].

Table 3.1: Lexicographic objective functions

Species	Number	Direction	Objective
Autotroph	1	Maximize	Growth rate
Autotroph	2	Minimize	Glucose secretion
Autotroph	3	Minimize	Oxygen secretion
Autotroph	4	Maximize	CO2 uptake
Autotroph	5	Maximize	Photon uptake
Autotroph	6	Maximize	Nitrate uptake
Autotroph	7	Maximize	Phosphate uptake
Heterotroph	1	Maximize	Growth rate
Heterotroph	2	Maximize	CO2 secretion
Heterotroph	3	Minimize	Glucose uptake
Heterotroph	4	Maximize	Oxygen uptake
Heterotroph	5	Maximize	Phosphate uptake

3.2.4 Model parameters

For determining parameter values, we used the species abundance data available at various depths in the biofilms of UCC-A and UCC-O at different times (see Figure 3.1B and 3.1C). The spatial data available for the fraction of biomass was converted to the biomass concentration at various locations by using biofilm density. The concentration of autotrophs and heterotrophs vary in space and time. We used day 7 spatial data as an initial condition for the model and validated the model for day 14, day 21 and day 28. We used least square curve (lscurvefit) fitting technique in MATLAB to fit the experimental data and validate the biofilm model. The lower bound and upper bounds on the parameters were chosen based on the available literature values. The global optima were ensured by using multistart option in MATLAB. This approach chose various starting points in from the lower and upper bounds. The parameters used in the biofilm model are shown in Table 1. The kinetic parameters (v_{max} and K_m) for the metabolites were obtained from model fitting. We have used the values obtained from literature as the initial guesses for v_{max} and K_m [114, 156, 157]. The aqueous diffusion coefficients for substrates and byproducts were converted to the biofilm diffusion coefficients using appropriate coefficients [122]. The

diffusion coefficients and the mass transfer rate constant for biomass were obtained from the validation of the biofilm experimental data.

Table 3.2: Nominal model parameter values

L	Biofilm thickness	30 μm	[154]
C_b	Bulk CO_2 concentration	10 mmol/L	Specified
I_{in}	Initial photon incidence rate	35 μE/m^{2}s	[154]
N_b	Nitrate bulk concentration	17.6 mmol/L	[158]
P_b	Bulk phosphate concentration	1 mmol/L	Specified
G_b	Bulk glucose concentration	0 mmol/L	Specified
O_b	Bulk O_2 concentration	0.21 mmol/L	Specified
D_{CO2}	Diffusion coefficient for CO_2	7.9x10^{-6} cm^2/s	[122]
D_G	Diffusion coefficient for glucose	1.8x10^{-6} cm^2/s	[122]
D_O	Diffusion coefficient for oxygen	1.8x10^{-5} cm^2/s	[122]
$k_{m,co2}$	CO_2 mass transfer coefficient	1x10^{-4} cm/s	Specified
$k_{m,i}$	Mass transfer coefficient for glucose and O_2	2x10^{-4} cm/s	Specified
$v_{max,co2}$	Maximum CO_2 uptake rate (mmol/gDW/h)	5 (UCC-A), 5 (UCC-O)	Fitted
$k_{m,co2}$	CO_2 half saturation constant (mmol/L)	0.5 (UCC-A), 0.5 (UCC-O)	Fitted
$v_{max,photon}$	Maximum Photon uptake rate (mmol/gDW/h)	1.16 (UCC-A), 1.1 (UCC-O)	Fitted
$k_{m,photon}$	Photon half saturation constant (mmol/L)	0.29 (UCC-A), 0.45 (UCC-O)	Fitted
$v_{max,N}$	Maximum Nitrate uptake rate (mmol/gDW/h)	0.3 (UCC-A), 0.027 (UCC-O)	Fitted
$k_{m,N}$	Nitrate half saturation constant (mmol/L)	2.7 (UCC-A), 0.001 (UCC-O)	Fitted
$v_{max,P}$	Maximum Phosphate uptake rate (mmol/gDW/h)	0.25 (UCC-A), 0.24 (UCC-O)	Fitted
$k_{m,P}$	Phosphate half saturation constant (mmol/L)	2 (UCC-A), 10 (UCC-O)	Fitted
$v_{max,G}$	Maximum Glucose uptake rate (mmol/gDW/h)	2.42 (UCC-A), 6.64 (UCC-O)	Fitted
$k_{m,G}$	Glucose half saturation constant (mmol/L)	1 (UCC-A), 0.5 (UCC-O)	Fitted
$v_{max,O2}$	Maximum O_2 uptake rate (mmol/gDW/h)	20	Fitted
$k_{m,O2}$	O_2 half saturation constant (mmol/L)	0.003	Fitted
$v_{maxh,P}$	Maximum CO_2 uptake rate (mmol/gDW/h)	0.25 (UCC-A), 0.42 (UCC-O)	Fitted
$k_{mh,P}$	Phosphate half saturation constant (mmol/L)	2 (UCC-A), 0.72 (UCC-O)	Fitted
D_a	Diffusion coefficient for Autotroph (μm^2/s)	0.021 (UCC-A), 0.013 (UCC-O)	Fitted
D_h	Diffusion coefficient for Heterotroph (μm^2/s)	0.031 (UCC-A), 0.023 (UCC-O)	Fitted
$k_{a,0}$	Autotroph mass transfer coefficient at $L = 0$ (μm/s)	0.25 (UCC-A), 0.01 (UCC-O)	Fitted
$k_{a,L}$	Autotroph mass transfer coefficient at $L = 30$ (μm/s)	1 (UCC-A), 0.01 (UCC-O)	Fitted
$k_{h,0}$	Heterotroph mass transfer coefficient at $L = 0$ (μm/s)	0.6 (UCC-A), 0.053 (UCC-O)	Fitted
$k_{h,L}$	Heterotroph mass transfer coefficient at $L = 30$ (μm/s)	0.98 (UCC-A), 0.42 (UCC-O)	Fitted
k_{tot}	Photon attenuation coefficient (μ^{-1})	1x10^{-3}	Fitted

3.3 Results

3.3.1 Biofilm model validation

The autotrophs were able to convert inorganic carbon into glucose and oxygen in presence of light energy. The glucose and oxygen diffused in the biofilm and heterotrophs used these as the substrates for their growth and increased their abundances. The phosphate uptake limitations in UCC-A model were added by choosing α_p value (equation 3.4, Model formulation) . The model fittings with and without

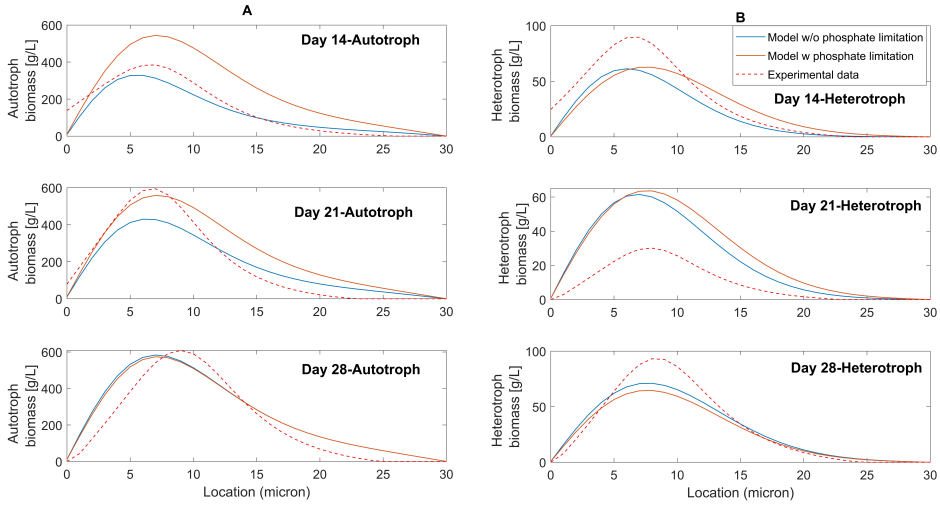

Figure 3.2: Spatially resolved model fitting for UCC-A autotroph-heterotroph biofilms with (red solid lines) and without (blue lines) nitrate and phosphate limitations. (A) Autotroph biomass (g/L) at day 14, 21 and 28 for biofilm of thickness L = 30 μm. (B) Heterotroph biomass (g/L) at day 14, 21 and 28 for biofilm of thickness L = 30 μm.

phosphate uptake limitation were compared. The model predicted that with phosphate limitations for day 14 and day 21, the biomass concentrations were higher than those without phosphate limitations. The day 28 predictions with and without phosphate were qualitatively similar. The model fittings were compared at $\alpha_p = 0.75$ and the fitting parameters were calculated.

Our biofilm model qualitatively captured the experimental behavior of the photoautotroph-heterotroph biofilms from hot lake (Figure 2 and Figure 3). The UCC-A model depicted the qualitative peak locations for the day 14 (Figure 3.2A and Figure 3.2B, top panels) and day 28 (Figure 3.2A and Figure 3.2B, bottom panels) for autotrophs and heterotrophs. The model also captured the shifting of temporal peak locations for autotrophs and heterotrophs. The model could not successfully fit the heterotroph data for day 21 (Figure 3.2B, middle panel). The possible reasons for this data would be an error in experimental behavior or the lack of details in the modeling framework.

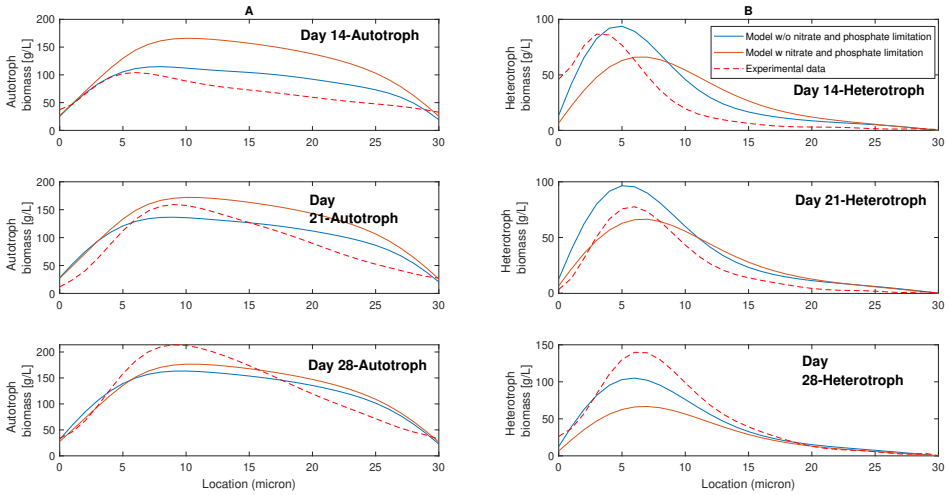

Figure 3.3: Spatially resolved model fitting for UCC-O autotroph-heterotroph biofilms with (red solid lines) and without (blue lines) nitrate and phosphate limitations. (A) Autotroph biomass (g/L) at day 14, 21 and 28 for biofilm of thickness L = 30 μm. (B) Heterotroph biomass (g/L) at day 14, 21 and 28 for biofilm of thickness L = 30 μm.

The UCC-O model predictions for autotroph and heterotrophs biomass were plotted with and without nitrate and phosphate limitations. The nitrate limitations for UCC-O was added to incorporate the ability of UCC-O to secrete extracellular polymeric substances which puts additional burden on UCC-O metabolism. We chose α_p =0.75 and α_n =0.75 to compare the model fittings with and without phosphate and nitrate uptake limitations. The autotroph biomass concentrations with nitrate and phosphate limitations were higher as compared with those without nitrate and phosphate limitations. The heterotroph concentrations without nitrate and phosphate limitations were higher than those with nitrate and phosphate limitations. The model fittings improved in presence of nitrate and phosphate limitations as this incorporates important metabolite exchanges in the system.

The UCC-O model captured the qualitative peak locations for autotrophs and heterotrophs for day 14 (Figure 3.3A and Figure 3.3B, top panels) and day 28 (Figure 3.3A and Figure 3.3B, bottom panels). The UCC-O model predicted lower

heterotroph biomass concentrations for day 14, day 21 and day 28 as compared to the experimental observation. Like UCC-A model, the UCC-O model also successfully captured the temporal shifts of peak locations for autotrophs and heterotrophs

The models predicted the concentration profiles for the metabolites. We did not have the experimental data for the metabolites, the metabolite profiles were in line with previous studies [159–161]. We would be using the fitted the parameters (Table 3.2) to predict the interspecies interactions, species organization, rate of byproduct formation at various CO_2 and photon concentrations.

3.3.2 Effect of CO_2

The validated model was used to predict the interactions between autotrophs and heterotrophs at various CO_2 concentrations under restricted phosphate and nitrate uptakes by autotrophs. Reduced nitrate and phosphate uptakes are observed during succession for UCC-O and reduced phosphate uptakes were observed for UCC-A [155]. This effect was incorporated by adding parameters for phosphate (α_p) and nitrate (α_n) in calculation of uptakes for autotrophs. We chose various values of α_p between 0 and 1 and the respective community biomass were calculated. For UCC-A, the biomass concentration was constant for α_p=1, 0.75, 0.5 but it decreased at α_p=0.25. In case of UCC-O the biomass concentration was very sensitive to α_p, the concentration dropped with decrease in α_p. Cyanobacterium Phormidium sp. OSCR is known to produce more extracellular polymeric substances (EPS) than cyanobacterium Phormidesmis priestleyi ANA. The core metabolic model lacked the fluxes for EPS secretions hence we have accounted for this behavior by restricting nitrate uptake for autotrophs in UCC-O by setting α_n =0.75. We have considered α_p=0.25 for UCC-A and UCC-O and evaluated the effect of CO_2 concentration on community abundances. We varied the concentration of CO_2 supplied at the top of the biofilm (L=0) from 0.1 mmol/L to 10 mmol/L under the photon incidence rate of 35 μE/m^{2}s. We have plotted the average

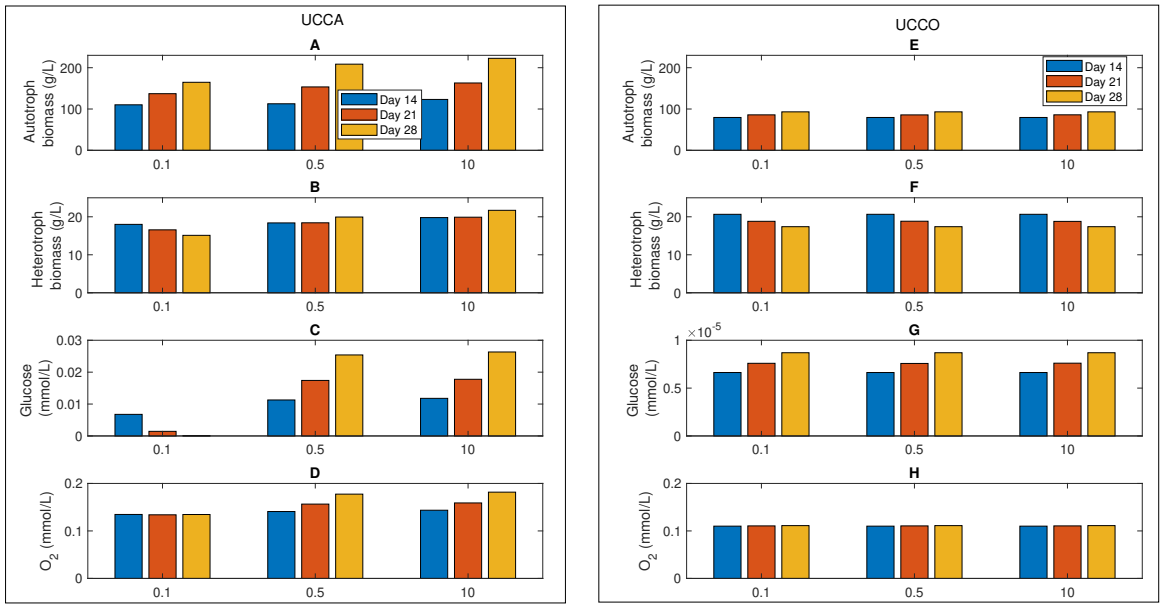

Figure 3.4: Predictions after 14, 21 and 28 days for UCC-A and UCC-O biofilms of thickness L = 30 μm at various C_2 concentration and constant photon incidence (35 $\mu E/m^2s$). 0.1: CO_2 concentration 0.1 mmol/L. 0.5: C_2 concentration 0.5 mmol/L. 10: C_2 concentration 10 mmol/L. (A) UCC-A: Autotroph biomass concentrations averaged across the biofilm. (B) UCC-A: Heterotroph biomass concentrations averaged across the biofilm. (C) UCC-A: Glucose concentrations averaged across the biofilm. (D) UCC-A: Oxygen concentrations averaged across the biofilm. (E) UCC-O: Autotroph biomass concentrations averaged across the biofilm. (F) UCC-O: Heterotroph biomass concentrations averaged across the biofilm. (G) UCC-O: Glucose concentrations averaged across the biofilm. (H) UCC-O: Oxygen concentrations averaged across the biofilm.

biomass concentrations and average metabolite (glucose and O_2) concentrations at the end of day 14, day 21 and day 28 for UCC-A and UCC-O biofilms.

The average autotroph biomass concentrations for UCC-A increased from day 14 to day 28 for various CO_2 concentrations whereas that of heterotrophs decreased for 0.1 mM of CO_2 and increased for all other CO_2 concentrations (Figure 3.4A and 3.4B). The highest autotroph biomass concentration (222.8 g/L at 28 days) and heterotroph biomass concentration (21.7 g/L at 28 days) were obtained for CO_2 concentration 10 mM. This suggests that the CO_2 concentration played an important

role in autotroph growth and biomass accumulation. Autotrophs secreted less amount of glucose for CO_2 level 0.1 mM as compared to CO_2 levels 0.5 mM and 10 mM. The accumulation of glucose at 0.1 mM of CO_2 was the least due to its faster consumption by heterotrophs. O_2 secretion increased with increase in supplied CO_2. Heterotroph growth was mainly limited by glucose secretion than that of O_2.

For UCC-O, autotroph biomass concentration increased from 79.5 g/L (at day 14) to 93 g/L (at day 28) for all CO_2 concentrations considered here (Figure 3.4E). This indicated that the CO_2 was not a limiting substrate for autotroph growth. Exact opposite trend was observed for heterotroph biomass concentration, it decreased from 20.7 g/L (at day 14) to 17.4 g/L (at day 28) (Figure 3.4F). The accumulation of glucose increased from day 14 to day 28 whereas that of O_2 was constant for all CO_2 levels. The model predicted that CO_2 concentration doesn't change the community composition in UCC-O.

3.3.3 Effect of light incidence rate

The model was further used to predict the impact of photon incidence on the community stability and dynamics. We evaluated three different photon incidence rates (10 μE/m^{2}s, 35 μE/m^{2}s and 50 μE/m^{2}s) at constant CO_2 concentration (10 mmol/L). The averaged species and metabolite concentrations were plotted at the end of 14, 21 and 28 days for UCC-A and UCC-O biofilms.

The autotroph concentration in case of UCC-A biofilms increased from day 14 to day 28 with increase in photon incidence rate from 10 μE/m^{2}s to 50 μE/m^{2}s (Figure 3.5A) with the highest concentration of 282.5 g/L was obtained at day 28 for photon incidence rate of 50 μE/m^{2}s. The amount of glucose secreted by autotrophs increased for photon incidence rate of 10 μE/m^{2}s and 35 μE/m^{2}s but it decreased for photon incidence rate 50 μE/m^{2}s (Figure 3.5C). The amount of O_2 secreted by autotrophs increased for all photon incidence rates (Figure 3.5D). Heterotrophs utilized the

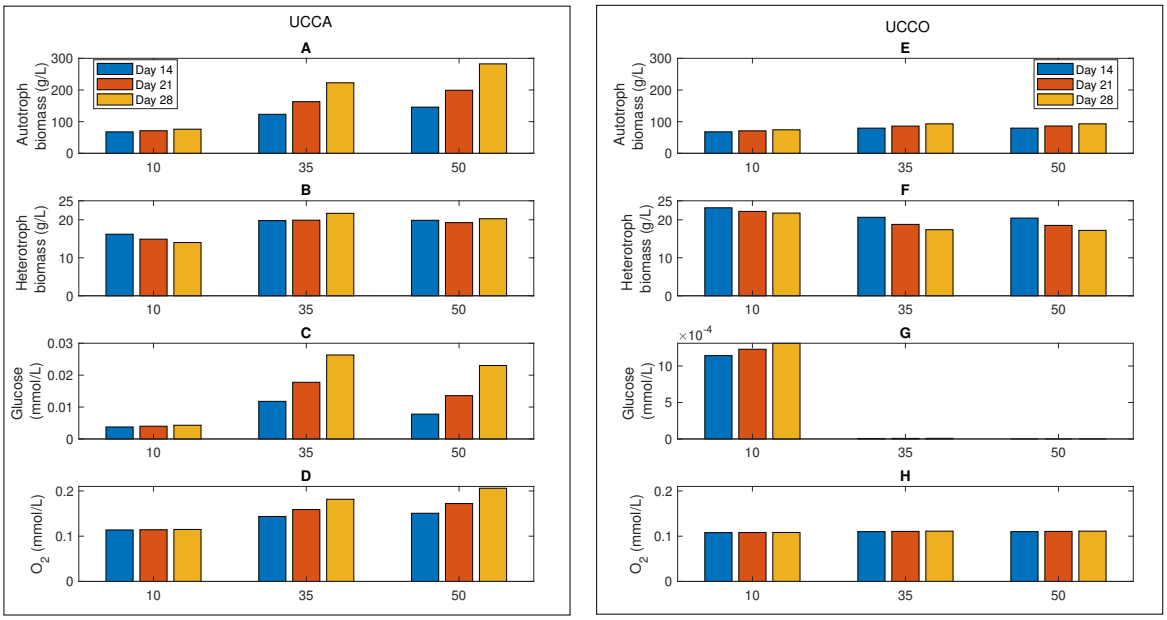

Figure 3.5: Predictions after 14, 21 and 28 days for UCC-A and UCC-O biofilms of thickness L = 30 μm at various photon incidence rates and constant C_2 concentration (10 mmol/L). 10: photon incidence rate 10 μE/m^{2}s. 35: photon incidence rate 35 μE/m^{2}s. 50: photon incidence rate 50 μE/m^{2}s. (A) UCC-A: Autotroph biomass concentrations averaged across the biofilm. (B) UCC-A: Heterotroph biomass concentrations averaged across the biofilm. (C) UCC-A: Glucose concentrations averaged across the biofilm. (D) UCC-A: Oxygen concentrations averaged across the biofilm. (E) UCC-O: Autotroph biomass concentrations averaged across the biofilm. (F) UCC-O: Heterotroph biomass concentrations averaged across the biofilm. (G) UCC-O: Glucose concentrations averaged across the biofilm. (H) UCC-O: Oxygen concentrations averaged across the biofilm.

glucose and oxygen efficiently and increased their abundances from 14 g/L (at day 28) to 21.7 g/L (at day 28) for the case of 10 μE/m^{2}s and 35 μE/m^{2}s respectively but later the abundance decreased to 20.3 g/L (at day 28) for incidence rate 50 μE/m^{2}s (Figure 3.5B). This suggested that the heterotroph concentration directly depended on autotroph concentration until photon incidence rate of 35 μE/m^{2}s but later it decreased for 50 μE/m^{2}s. The autotroph concentration increased with increase in photon incidence rate.

The autotroph concentration in case of UCC-O biofilms increased from day 14 to day 28 with increase in photon incidence rate from 10 $\mu E/m^2s$ to 50 $\mu E/m^2s$ (Figure 3.5E) with the highest concentration of 93.1 g/L was obtained at day 28 for photon incidence rate of 35 and 50 $\mu E/m^2s$. The amount of glucose accumulated decreased for photon incidence rates of 35 $\mu E/m^2s$ and 50 $\mu E/m^2s$ but it increased for photon incidence rate 10 $\mu E/m^2s$ (Figure 3.5G). The amount of O_2 accumulated in biofilm was constant for all photon incidence rates (Figure 3.5H). Heterotrophs utilized the glucose and oxygen increased their abundances initially for day 14 but it decreased due to low glucose availability. Time averaged heterotroph concentration dropped from 22.4 g/L to 18.7 g/L with increase in photon incidence rate. This suggested that the photon incidence rate positively affected the autotroph concentrations but negatively impacted the heterotroph abundances.

3.3.4 Species coexistence

The species coexistence was predicted based on available CO_2 and photon incidence rate. We varied supplied CO_2 concentration within the range 0.01 mmol/L and 1 mmol/L. The photon incidence rate was varied from 10 $\mu E/m^2s$ to 50 $\mu E/m^2s$. We ran 81 simulations each for UCC-O and UCC-A and plotted the results at the end of 28 days to find out the conditions feasible for coexistence of autotrophs and heterotrophs in the community. We concluded that species coexisted if the average concentration of autotroph was more than 70 g/L and that of heterotroph was at least 15 g/L.

For UCC-A biofilms, at the lowest photon incidence rate (10 $\mu E/m^2s$) and at the lowest CO_2 concentration (0.01 mM), the autotroph biomass concentrations were less than 70 g/L (Figure 3.6A) and that of heterotrophs were less than 15 g/L (Figure 3.6B). Hence at lowest photon incidence rate (10 $\mu E/m^2s$) and at lowest CO_2 concentration (0.01 mM), the species could not coexist. At photon incidence

rate of 15 μE/m^{2}s, the species coexist if CO_2 concentration was above 0.05 mM. The species could coexist for CO_2 level 0.075 until the photon incidence rate reached to 25 μE/m^{2}s. The autotroph biomass increased with increase in photon incidence rate and increase in CO_2 levels. However, the heterotroph biomass concentrations largely depended on the photon incidence rate, as photon concentration impacts the secretion of glucose by autotrophs (see Supplementary figure 2). The glucose secretion increased with increase in CO_2 concentrations. The secretion of glucose increased initially with increase in photon incidence rate, but it decreased later with increase in incidence rates. This behavior is in line with the typical cyanobacteria metabolism (Clark et al., 2018). The higher photon incidence rates required high CO_2 levels for species coexistence. The highest autotroph biomass (282.5 g/L) was obtained when the photon incidence rate was 50 μE/m^{2}s and CO_2 concentration was greater than 0.5 mM. The highest heterotroph biomass concentration (22 g/L) was obtained for photon incidence rate 40 μE/m^{2}s and CO_2 concentration greater than 0.5 mM. The model predicted that the UCC-A community stability will be governed by carbon availability than the photon incidence rate.

The UCC-O biofilm coexistence map showed that the species cannot coexist at the lowest CO_2 concentration 0.01 mM (Figure 3.6C and 3.6D). At the CO_2 concentration the autotroph biomass was 66.3 g/L and that of heterotroph was 17.2 g/L. Once the CO_2 concentration reaches 0.025 mM, the species coexistence was observed for all photon incidence rates. The highest autotroph biomass concentration was observed when photon incidence rate was greater than 20 μE/m^{2}s and CO_2 concentration was higher than 0.05 mM. However, the highest heterotroph biomass was observed when photon incidence rate was 20 μE/m^{2}s and CO_2 concentration was greater than 0.05 mM. Higher concentrations of photon helped autotrophs to increase their abundances, but the heterotroph concentration increased initially with increase in photon incidence but decreased for higher values of incidence rates. The model predicted

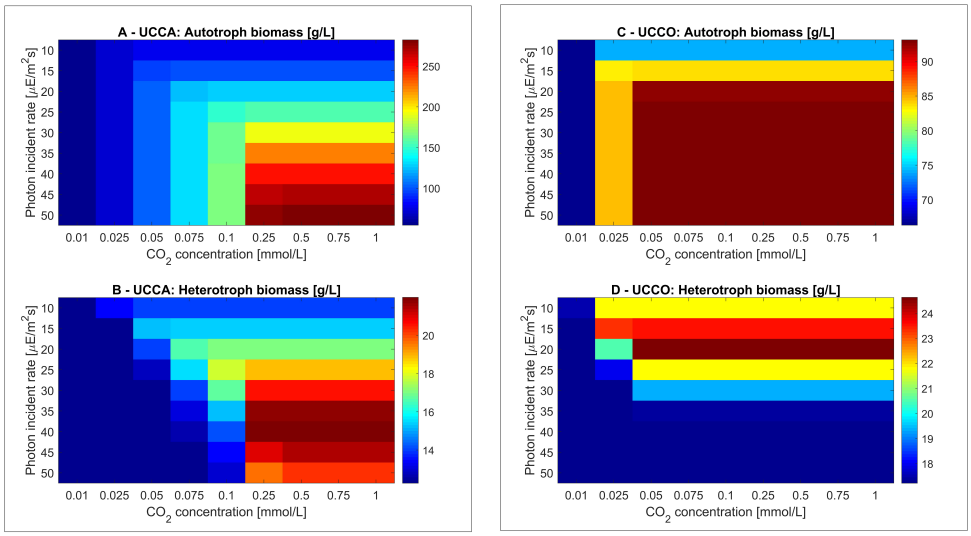

Figure 3.6: Model predictions for coexistence of autotrophs and heterotrophs for UCC-A and UCC-O (A) UCC-A: Autotroph biomass concentration (g/L) at various C_2 and photon incidence rates for biofilm of thickness L= 30m. (B) UCC-A: Heterotroph biomass concentration (g/L) at various C_2 and photon incidence rates for biofilm of thickness L= 30m. (C) UCC-O: Autotroph biomass concentration (g/L) at various C_2 and photon incidence rates for biofilm of thickness L= 30m. (D) UCC-O: Heterotroph biomass concentration (g/L) at various C_2 and photon incidence rates for biofilm of thickness L= 30m.

that the UCC-O community stability will be governed by the photon incidence rate than the carbon availability.

3.4 Discussion

The cyanobacteria present in the hot lake microbial mat use sunlight and CO_2 and produce valuable organic compounds such as glycerol, glucose, ethanol and oxygen. These valuable compounds are further utilized by heterotrophs in the vicinity and heterotrophs generate CO_2 and scavenge toxic compounds. These mutualistic relationship benefits both the members in the community [162, 163, 15].

We have developed a biofilm model to study the interactions within the autotroph-heterotroph community found in unicyanobacterial consortia in microbial mat. The model was developed using core metabolic constructions of UCC-A/UCC-O and a mixed bag model of 5 dominant heterotrophs. The models were generated in Kbase database by using the respective genomes of the species. The Kbase database was further used to gapfill the models and to analyse the growth conditions of the models. The metabolic models combined with reaction diffusion equations were solved to get species abundances. We validated the models by using an experimental data available for photoautotroph-heterotroph community found in microbial mat. The autotrophs interacted with heterotrophs through metabolite exchanges (glucose and oxygen). These metabolites were secreted by autotrophs in presence of CO_2 and photon.

The models were used to predict the effect of CO_2 and photon on interactions within the community and the species coexistence. UCC-A model predicted that the autotroph biomass increased by 35%, and the heterotroph biomass by 43% when CO_2 concentration increased from 0.1 mM to 10 mM at constant photon rate (35). This suggested that the CO_2 concentration significantly impacted the community biomass and the species interactions. In case of UCC-O community, CO_2 concentration did not change the individual biomass concentrations, suggesting that the community

is robust to the change in the concentration of available carbon at constant photon rate. When we varied the photon rates at constant CO_2 concentration (10 mM), we found that for UCC-A and UCC-O, autotroph biomass increased monotonically. The heterotroph biomass in UCC-A increased with increase in photon (10 $\mu E/m^2s$ to 35 $\mu E/m^2s$) but decreased at higher incidence rate (35 $\mu E/m^2s$). This effect is more pronounced for heterotrophic community in UCC-O.

The model used for prediction of the species interactions at various depths in the hot lake environment. The high photon incidence rate would be present at the lower depths, the photon penetration decreased at higher depths in the lake [164, 165]. Our models captured the species interactions at various depths in hot lake and predicted the species abundances and coexistence. This will help to further analyse the species behaviour in the community and role of species in ecology. The complexity of the models can be further increased by adding more specific interactions such as chemotaxis. The cyanobacteria are known to secret biofuels and chemicals efficiently with the help of CO_2 and light energy [166–169]. Our models can be used to predict and evaluate conditions favourable for the higher production of these chemicals and biofuels by helping in designing of community with maximum interactions.

CHAPTER 4

METABOLIC MODELING OF *CLOSTRIDIUM DIFFICILE* ASSOCIATED DYSBIOSIS OF THE GUT MICROBIOTA

4.1 Introduction

Numerous experimental studies have demonstrated that *C. difficile* [170–173] can form biofilms *in vitro*. The other commensal bacteria [8, 174] can form biofilms *in vivo* which are well known to exhibit phenotypes distinct from planktonic cultures. Mechanistic understanding of the relationships between biofilm spatial variations, species-species interactions and host-species interactions remains inadequate to systematically analyze and rationally treat CDI [175]. To address these challenges, we added *C. difficile* to our previous multispecies biofilm model [176, 177] consisting of three representative species from the phyla Bacteroidetes (*Bacteroides thetaiotaomicron*), Firmicutes (*Faecalibacterium prausnitzii*) and Proteobacteria (*Escherichia coli*). Model simulations were performed to connect host induced nutrient changes in the gut environment with observed alternations of species abundances and SCFA levels [178–180] to unravel the metabolic determinants of CDI.

This work is published as: Phalak, Poonam, and Michael A. Henson. "Metabolic Modeling of *Clostridium difficile* Associated Dysbiosis of the Gut Microbiota." *Processes* 7, no. 2 (2019): 97.

4.2 Materials and methods

4.2.1 Biofilm model formulation and solution

The multispecies biofilm model was constructed by combining genome-scale metabolic reconstructions of *C. difficile* (strain 630Δerm) [181] and three commensal gut species: *B. thetaiotaomicron* [182], *F. prausnitzii* (strain A2-165) [183] and *E. coli* (strain K-12 MG1655) [184]. The biofilm was considered to be attached to the colon lining defined as top of the biofilm (Figure 4.1A). A minimal defined media (MDM) containing glucose, cysteine, isoleucine, leucine, methionine, proline, serine, tryptophan and valine along with essential vitamins and minerals was used for all simulations. The amino acids cysteine, isoleucine, leucine, proline, serine and tryptophan are essential for *in vivo C. difficile* growth [185, 186], while the amino acids methionine, tryptophan and serine are essential for *in vivo F. prausnitzii* growth [187]. To simulate various host-microbiota perturbations, the primary bile acid taurocholate and/or the electron acceptor nitrate were added to the media. The diffusion of nutrients, byproducts and species biomass was assumed to occur only in the axial direction z. Therefore, each variable was considered to be changing with respect to space z and time t over a fixed biofilm thickness L.

The nutrients were supplied at the top of the biofilm (Figure 4.1A). SCFAs, ethanol, organic acids and CO_2 produced by the four species were allowed to diffuse and be removed from both ends of the biofilm. Biomass was assumed to slowly move through the biofilm by a diffusion and be removed from the biofilm-stool interface according to a continuous erosion mechanism, as described in our previous publications [176, 177, 188]. This assumption provided a reasonable mechanism to ensure that biomass generation would be balanced by biomass loss such that steady-state solution could be obtained. The multispecies biofilm model was tuned with nominal glucose and amino acid concentrations to reproduce species abundances and SCFA levels consistent with experimental studies on healthy individuals [189, 190]. This

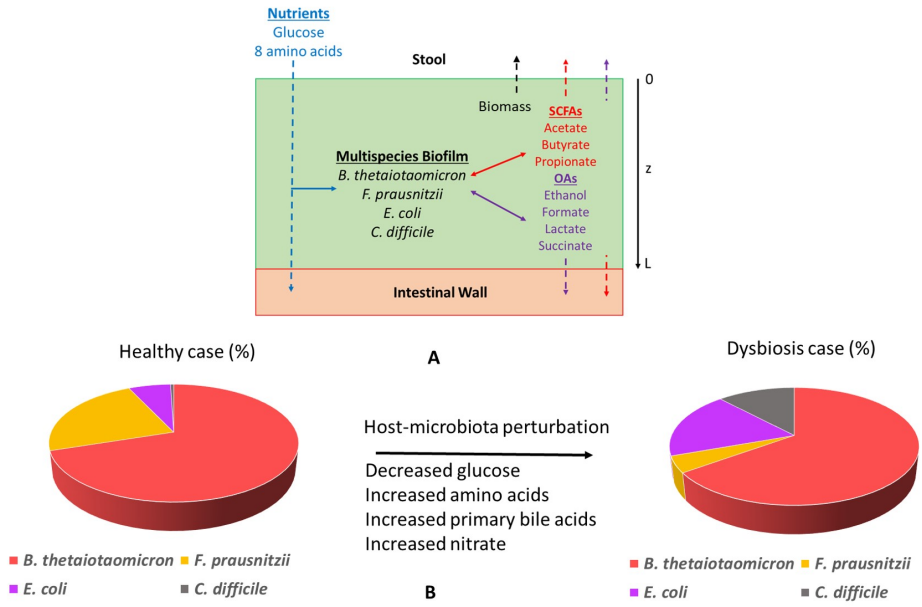

Figure 4.1: Schematic representation of the *in silico* gut community. (A) The model assumed biofilm attachment to the intestinal wall and described diffusion of glucose, amino acids, short-chain fatty acids, organic acids, ethanol, CO_2 and species biomass in and/or out of the biofilm along the axial direction z. (B) Host-microbiota perturbations were modeled through changes in the bulk concentrations of glucose, amino acids, primary bile acids and nitrate at the biofilm-stool interface to predict species abundances in healthy and *C. difficile* infected guts.

tuned model was referred to as the "healthy case". Host-microbiota perturbations were simulated by altering glucose/amino acid concentrations, and/or by introducing primary bile acids and nitrate as nutrients to predict the resulting species abundances (Figure 4.1B). These models were collectively referred to as the "dysbiosis case." In vivo concentrations of glucose and AA in the guts of healthy and C. difficile infected patients are not commonly available. We have specified the glucose and AA concentrations for the healthy case based on limited experimental data [28, 191–194] and have reduced the glucose concentration and increased AA concentrations for the dysbiosis case consistent with experimental observation [49, 195]. We performed a sensitivity analysis of these concentrations to show that similar behavior (i.e. healthy state) as that reported for the nominal values occurs if the glucose to AA ratio was sufficiently large (not shown here). By contrast, a CDI dysbiosis-like state was obtained when the glucose to AA ratio was sufficiently small.

Uptake rates of nutrients and byproducts were assumed to follow Michaelis-Menten kinetics. Due to lack of available data, maximum uptake rates and Michaelis-Menten constants were assumed to be independent of species and metabolite. Calculated uptake rates were imposed as lower bounds of the exchange fluxes in the species metabolic reconstructions. The calculated growth rate, uptake fluxes and secretion fluxes from each reconstruction served as inputs to reaction-diffusion type equations for the biomass concentration of each species and the molar concentration of each nutrient and byproduct. This formulation yielded a set of 23 partial differential equations (PDEs) in time and the axial direction z with embedded linear programs (LPs) for species metabolism. Following on our previous methodology [176, 177], lexicographic optimization with growth rate maximization as the primary objective was used to avoid alternative optima that would render the biofilm model non-smooth. This approach yielded a total of 71 LPs.

The biofilm model equations were solved by spatially discretizing the PDEs into a large set of ordinary differential equations (ODEs) [93, 141]. We used 25 spatial node points to achieve a suitable compromise between solution accuracy and computational efficiency, which produce a discretized model with 575 ODES and 1,775 LPs that was solved with the MATLAB code DFBAlab [126]. We used Gurobi 6.5.2 for LP solution, the stiff MATLAB solver ode15s for ODE integration and DFBAlab running in MATLAB 9.0 (R2016a).

4.2.2 Biofilm model parameterization and tuning

Nominal parameter values used in the multispecies biofilm model are shown in Table 4.1. The parameters were obtained from the experimental literature to extent possible and from our previous modeling studies [176, 177] as necessary. The bulk glucose and amino acid concentrations at the biofilm-stool interface were specified to reflect healthy gut conditions. Due to lack of species-specific uptake data, we used published kinetic parameters reported for *E. coli* [114]. Due to lack of data, all eight byproducts were assumed to have the same uptake parameters as glucose. For simplicity, all eight amino acids were assumed to have the same uptake parameters obtained as the average of amino acid dependent values reported for *E. coli* [114].

With all other parameter values fixed, the biofilm model was qualitatively tuned to achieve biomass and SCFA fractions within experimental ranges for a healthy patient. The species abundances were tuned by adjusting the non-growth associated ATP maintenance (ATPM) values of the four metabolic reconstructions following our previous studies [176, 177]. Our justification for tuning these values was the simple nature of the biofilm model, which neglected other phyla (e.g. Actinobacteria), other nutrients (e.g. oligosaccharides, fats), other species interactions (e.g. Actinobacteria cross feeding of SCFAs and organic acids) as well as host metabolism present in the actual gut environment. These ATPM values listed in Table 4.1 produced *B.*

thetaiotaomicron:*F. prausnitzii*:*E. coli*:*C. difficile* abundances of 71%:21%:7%:1%, which were deemed reasonable based on published data [189, 190]. We found that coexistence of the four species was achieved over a range of ATPM values (not shown here).

We adjusted the SCFA mass transfer coefficients controlling metabolite removal from the biofilm to tune the acetate, butyrate and propionate concentrations for the healthy case. Starting with a value of $5\text{x}10^{-6}$ cm/s, the butyrate and propionate values were decreased until approximate fractions of 60%:20%:20% consistent with published data [21, 196] was obtained. We justified the use of SCFA-dependent values by noting that our model neglected host-microbiota interactions which would be expected to strongly affect SCFA levels *in vivo*. Biofilm simulations were performed for four combinations of bulk glucose, amino acid, nitrate and taurocholate concentrations chosen to mimic a healthy gut environment and three unhealthy nutrient environments (high amino acids, high primary bile acids, high nitrate) experimentally correlated to *C. difficile* associated dysbiosis (Table 4.2). We deemed the actual concentrations used to be less important than the concentration trends (*e.g.* decreasing glucose and increasing amino acids in the high amino acids case) since our goal was to qualitatively assess the effects of nutrient levels on community behavior.

4.3 Results

4.3.1 Discovery of putative byproduct crossfeeding relationships

Our previous modeling study [176] without *C. difficile* generated three byproduct crossfeeding relationships that were predicted to be necessary and sufficient for coexistence of the three species: *B. thetaiotaomicron* consumption of ethanol secreted by *E. coli* and *F. prausnitzii* consumption of acetate and succinate secreted by *B. thetaiotaomicron* and *E. coli*. Preliminary flux balance analysis (FBA) with the *C. difficile* reconstruction showed acetate, butyrate and propionate were the major byproducts

Table 4.1: Nominal parameter values for the multispecies biofilm model.

Symbol	Parameter	Value	Source
L	Biofilm thickness(μm)	40	[85]
X_b	Biomass bulk concentrations (g/L)	0	[176]
P_b	Byproduct bulk concentrations (mmol/L)	0	[176]
D_i	Diffusion coefficient (cm^2/s)		
D_X	Biomass	$2x10^{-10}$	[176]
D_N	Glucose	$2.01x10^{-6}$	[122]
	Cysteine	$2.45x10^{-6}$	[122]
	Isoleucine	$2.19x10^{-6}$	[122]
	Leucine	$2.19x10^{-6}$	[122]
	Methionine	$2.21x10^{-6}$	[122]
	Proline	$2.51x10^{-6}$	[122]
	Serine	$2.64x10^{-6}$	[122]
	Tryptophan	$1.89x10^{-6}$	[122]
	Valine	$2.49x10^{-6}$	[122]
D_P	Acetate	$3.03x10^{-6}$	[122]
	Butyrate	$1.74x10^{-6}$	[122]
	CO_2	$1.15x10^{-5}$	[122]
	Ethanol	$3.97x10^{-6}$	[122]
	Formate	$4.23x10^{-6}$	[122]
	Lactate	$3.1x10^{-6}$	[122]
	Propionate	$4.03x10^{-6}$	[122]
	Succinate	$2.82x10^{-6}$	[122]
	Nitrate	$1.29x10^{-5}$	[122]
	Taurocholate	$7.29x10^{-7}$	[122]
	Mass transfer coefficient (cm/s)		
k_X	Biomass	$6x10^{-7}$	[176]
k_N	Glucose	$2x10^{-4}$	[176]
	Amino acid	$2x10^{-4}$	[176]
k_P	Byproduct	$5x10^{-6}$	[176]
	Butyrate	$8.5x10^{-5}$	Tuned
	Propionate	$1.35x10^{-5}$	Tuned
	Nitrate	$1.5x10^{-5}$	Tuned
	Taurocholate	$2x10^{-3}$	Tuned
v_{max}	Maximum uptake rate (mmol/gDW/h)		
	Glucose	10	[114]
	Amino acid	1	[114]
	Byproduct	10	[176]
K_m	Michaelis-Menten constant (mmol/L)		
	Glucose	0.5	[114]
	Amino acids	0.1	[114]
	Byproduct	0.5	[176]
$ATPM$	ATP maintenance (mmol/gDW/h)		
	B. thetaiotaomicron	4.25	Tuned
	F. prausnitzii	3.4	Tuned
	E. coli	2.75	Tuned
	C. difficile	8.43	Tuned

Table 4.2: Nutrient concentrations used for healthy and three dysbiosis simulation cases in mmol/L.

Nutrient	**Healthy**	**High amino acids, low glucose**	**High primary bile acids**	**High nitrate**
Glucose	8.0	4.0	8.0	4.0
Cysteine	0.5	1.0	0.5	1.0
Isoleucine	0.5	1.0	0.5	1.0
Leucine	0.5	1.0	0.5	1.0
Methionine	0.5	1.0	0.5	1.0
Proline	0.5	1.0	0.5	1.0
Serine	0.5	1.0	0.5	1.0
Tryptophan	0.5	1.0	0.5	1.0
Valine	0.5	1.0	0.5	1.0
Nitrate	0	0	0	0.4
Taurocholate	0	0	1.5	1.5

and succinate and formate could be uptaken as carbon sources in the presence of glucose. With this knowledge, the four-species biofilm model was analyzed to discover additional crossfeeding relationships that support *C. difficile* coexistence with the three commensal species. Each species was allowed to consume glucose, the eight amino acids and any available byproduct (acetate, CO_2, ethanol, formate, lactate and succinate) assuming no differences in uptake kinetics across species and byproducts (see Materials and Methods). Simulations with a biofilm thickness of 40 microns and bulk concentrations of 8 mmol/L glucose and 0.5 mmol/L each amino acid at the biofilm-stool interface corresponding to the healthy case (Table 4.2) were run for 300 hours to ensure a steady-state solution consistent with a mature biofilm was obtained. A particular crossfeeding relationship was deemed significant if at least one uptake or secretion flux exceeded 1 mmol/gDW·h.

The biofilm model predicted significant crossfeeding of acetate, ethanol, formate and succinate between the four species (Figure 4.2A). Lactate and CO_2 crossfeeding were insignificant. Importantly for this study, *C. difficile* was predicted to: (1) con-

sume formate secreted by *F. prausnitzii* and *E. coli*; (2) compete with *F. prausnitzii* for succinate secreted by *B. thetaiotaomicron*; and (3) synthesize acetate for consumption by *F. prausnitzii* (Figure 4.2B). Experimentally, *C. difficile* has been shown to uptake succinate and produce butyrate [197] and to produce acetate by consuming formate directly or indirectly by uptaking CO_2 and H_2 [198]. Consequently, we hypothesized that formate and succinate crossfeeding could play a role in *C. difficile* propagation *in vivo*.

To test community stability and robustness in the absence of *C. difficile*, the same simulation was performed with the initial *C. difficile* biomass concentration set to zero. The resulting three-species community remained stable with *B. thetaiotaomicron*:*F. prausnitzii*:*E. coli* abundances of 66%:27%:7% consistent with a healthy gut community. These predictions were aligned with our previous study [176].

4.3.2 Characterization of healthy gut microbiota

With the putative crossfeeding relationships (Figure 4.2B) included, the multispecies biofilm model was simulated for a biofilm thickness of 40 microns and the healthy nutrient levels (Table 4.2). The model was tuned such that the mature biofilm obtained after 300 hours of simulation produced *B. thetaiotaomicron*:*F. prausnitzii*:*E. coli*:*C. difficile* abundances of 71%:21%:7%:1% when averaged across the biofilm (see Materials and Methods). These abundances were consistent with data from *in vivo* studies [189, 190].

We analyzed species biomass concentrations (Figure 4.3A) and local growth rates (Figure 4.3B) with respect to location in the biofilm with nutrients supplied at the biofilm-stool interface ($z = 0$). *C. difficile* was predicted to have the highest growth rates in the nutrient-rich bottom half of the biofilm but the lowest growth rates in the nutrient-lean top half. The local growth rates of the three commensal bacteria were comparable across the biofilm, with *B. thetaiotaomicron* having the highest growth

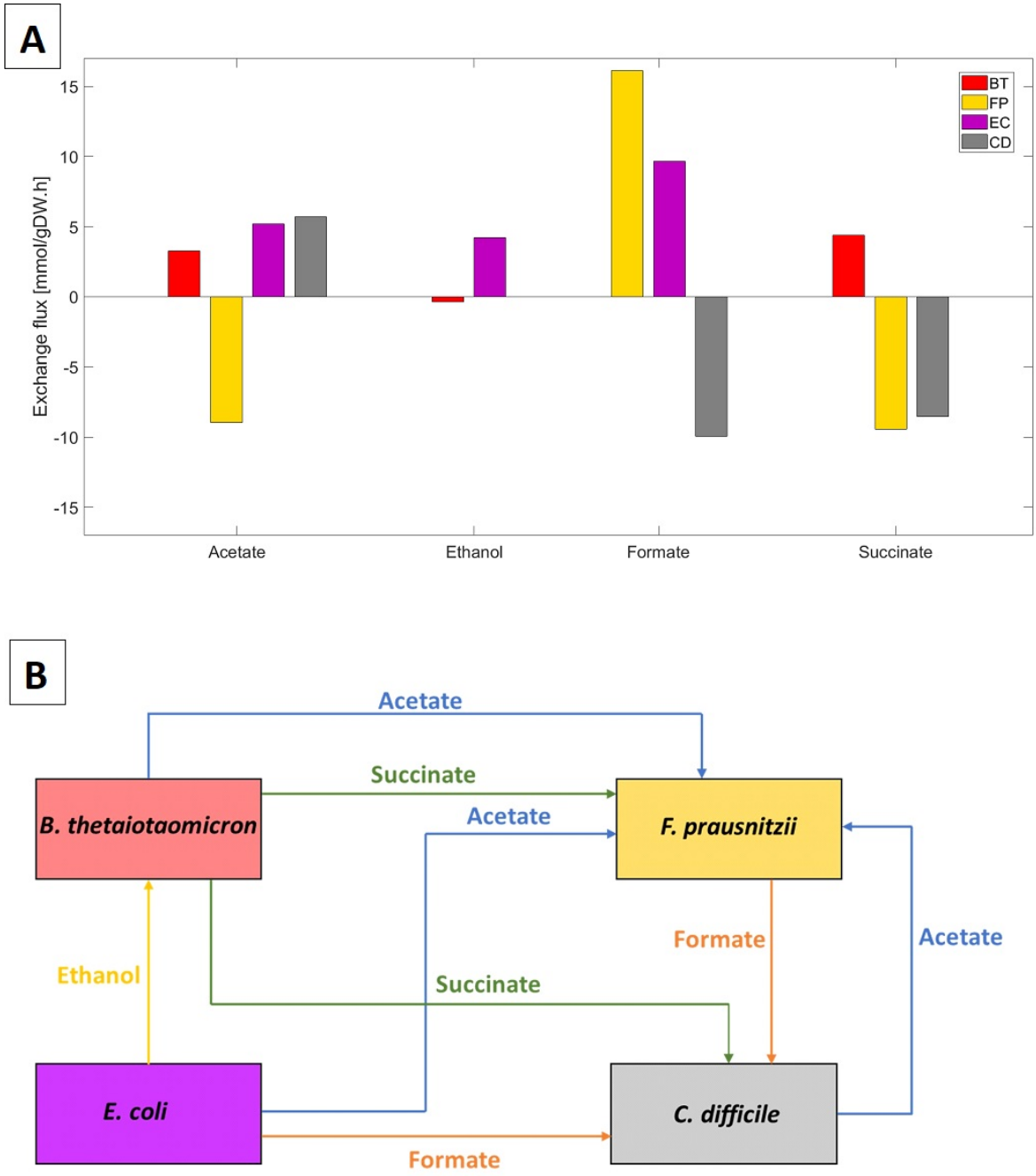

Figure 4.2: Predicted cross feeding of byproducts between the four species. (A) Species exchange rates specified in mmol/gDW/h. Secretion rates are positive and uptake rates are negative. (B) Byproduct cross-feeding patterns identified from the species uptake and secretion fluxes in Figure 4.2 A.

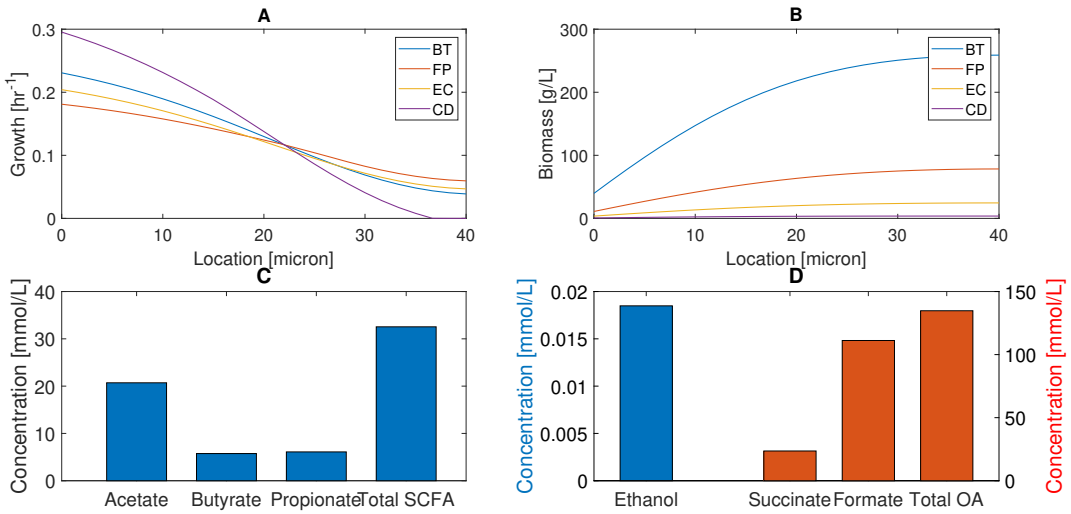

Figure 4.3: Predicted multispecies biofilm behavior in the absence of host-microbiota perturbations. (A) Species biomass concentrations across the thickness of the biofilm with nutrients supplied and biomass removed at $z = 0$ microns. (B) Local species growth rates across the thickness of the biofilm. (C) Acetate, butyrate, propionate and total SCFA concentrations averaged across the biofilm. (D) Ethanol, succinate, formate and total OA levels averaged across the biofilm.

rates in the bottom half and *F. prausnitzii* having a slight advantage in the top half. Due to its growth advantage in the nutrient-rich bottom half and slow cellular diffusion, *B. thetaiotaomicron* produced much higher biomass concentrations across the entire biofilm. *F. prausnitzii* and *E. coli* established lower biomass concentrations, while *C. difficile* was present at small concentrations due to its very small growth rate in the nutrient-lean top half. The spatial distributions of supplied nutrients, species biomass and secreted byproducts were similar to those reported in our previous studies [176, 177] and are omitted here. This simulation suggests that the commensal bacteria can sublimate *C. difficile* propagation through nutrient competition and may help explain how healthy individuals can be asymptomatically colonized.

The biofilm model also was tuned for healthy nutrient levels to produce acetate:propionate:butyrate fractions of 60%:20%:20% when averaged across the biofilm to be consistent with *in vivo* studies [21, 196] (See Materials and Methods). The model

predicted the total SCFA concentration to be 32.5 mmol/L (Figure 4.3C), which was in reasonable agreement with an *in vivo* study with control diet that yielded 41.1 mmol/L of total SCFAs [199]. One possible explanation for the lower SCFA levels predicted by our model is the simplified diet (glucose, eight amino acids) compared to the control diet used experimentally.

Ethanol was present at a very low level (Figure 4.3D) due to limited synthesis by the small *E. coli* population and high consumption by the large *B. thetaiotaomicron* population. Of the two organic acids (OAs) produced, formate was predicted to be present at a high level because synthesis by *F. prausnitzii* and *E. coli* substantially exceeded consumption by *C. difficile*. Succinate was present at a moderate level since it was consumed by both *C. difficile* and *F. prausnitzii*. These predictions suggest that plentiful formate and succinate could be available to promote *C. difficile* propagation under *in vivo* perturbations.

4.3.3 Glucose and amino acid perturbations

Various *in vivo* studies have shown that glucose concentration decreases and amino acid concentrations increase in the gut during *C. difficile* and other types of dysbiosis [28, 191–194]. To investigate the effects of altered nutrient levels associated with host-microbiota perturbations, we performed simulations for a 40 micron biofilm with elevated amino acid and reduced glucose bulk concentrations (Table 4.2) under the assumption that *C. difficile* expansion is driven by these experimentally-observed nutrient changes. While *in vivo* nutrient levels are impacted by diet, host metabolism and microbiota, this assumption was deemed reasonable given the simplified nature of our model. Given the uncertainty associated with the bulk nutrient concentrations, we performed a sensitivity analysis to explore their effects .with respect to the species abundances (not shown here). This analysis was consistent with the model predictions reported below as long as the glucose to amino acid ratio was sufficiently

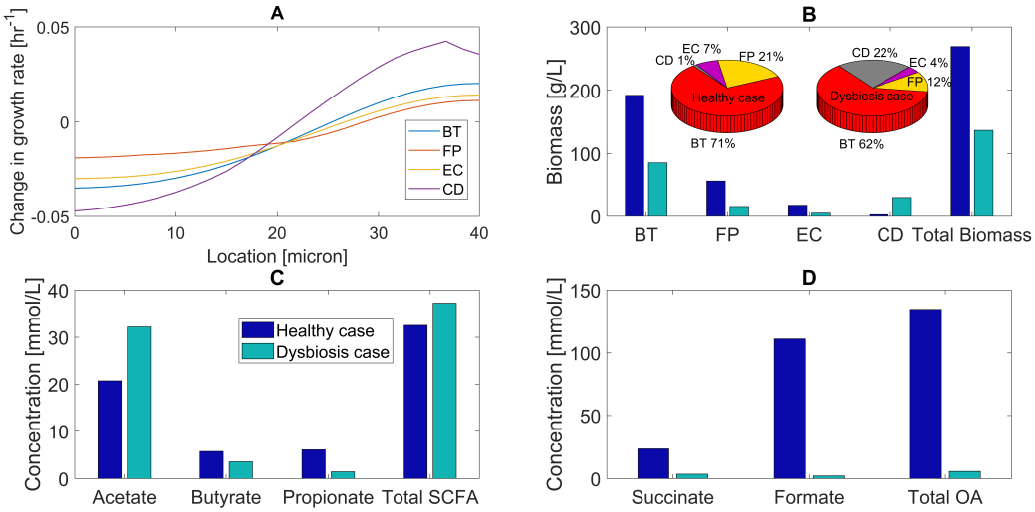

Figure 4.4: Predicted multispecies biofilm dysbiosis resulting from host-microbiota perturbations in glucose and amino acid concentrations. (A) Change in species growth rates across the biofilm plotted as the difference between the growth rates for the healthy and dysbiosis cases. (B) Biomass concentrations (bar graphs) and species abundances (pie chart) averaged across the biofilm for healthy and dysbiosis case. (C) Acetate, butyrate, propionate and total SCFA concentrations averaged across the biofilm. (D) Succinate, formate and total OA concentrations averaged across the biofilm.

large. Compared to the healthy case, the local *C. difficile* growth rate decreased in the bottom half of the biofilm but increased in the top half (Figure 4.4A). Similar trends were predicted for the three commensal species, which we attributed to reduced glucose but increased amino acid penetration into the biofilm. *C. difficile* is known to grow efficiently on amino acids due to its ability to use amino acid pairs such as leucine and proline to generate ATP via Stickland metabolism [200, 185, 186].

As a result of its enhanced growth in the top half of the biofilm compared to the commensal species, *C. difficile* increased its average biomass concentration ten-fold and species abundance from 1% to 22% compared to the healthy case (Figure 4.4A). The biomass concentration of each commensal species dropped due to reduced glucose availability. A substantial effect was predicted for *F. prausnitzii* with its species abundance decreasing from 21% to 12%, partially due to increased competition for succinate with *C. difficile*. These predictions are in agreement with *in vivo* studies

[45, 201–203], with the exception that dysbiosis during CDI should be accompanied by an increase in *E. coli* abundance [29, 31, 204–206]. The model predicted reduced total biomass production due to reduced growth of the three commensal species.

Dysbiosis was predicted to result in increased acetate, decreased butyrate and propionate, and lower total SCFA levels compared to the healthy case (Figure 4.4C). We attributed reduced total SCFA synthesis to lower glucose availability and increased acetate and decreased butyrate levels to a change in the balance of acetate-producing *C. difficile* and acetate-to-butyrate converting *F. prausnitzii*. Experimental studies have shown that dysbiosis is associated with reduced butyrate concentrations in the gut [202, 207]. The model predicted large changes in organic acid levels, with succinate, formate and total OA concentrations dropping due to reduced glucose fermentation. These predictions suggest that the combination of decreased carbohydrate and increased amino acid levels could play a role in *C. difficile* associated dysbiosis.

4.3.4 Primary bile acid perturbations

Primary bile acids such as taurocholate are secreted by the liver and transported into the intestines where anaerobic bacteria degrade them into secondary bile acids [208–210]. Broad spectrum antibiotics are known to reduce gut microbiota diversity [46–49, 211], including the possible loss of bacterial species from families *Lachnospiraceae* and *Ruminococcaceae* responsible for conversion of primary bile acids. Various *in vitro* [212, 210, 213] and *in vivo* [32, 214] studies have shown that *C. difficile* spores can use primary bile acids for germination. Sodium taurocholate is the typical reagent used to grow *C. difficile in vitro* [215, 216]. We investigated the impact of such perturbations with the multispecies biofilm model by adding taurocholate as a representative primary bile acid (Table 4.2). While primary bile acids are known to promote *C. difficile* transition from spores to a vegetative state [212, 217], we assumed that *C. difficile* was already vegetative and investigated the effect of

taurocholate on *C. difficile* growth. Preliminary FBA calculations with the *C. difficile* metabolic reconstruction showed that taurocholate uptake increased the growth rate, while taurocholate uptake was not possible with the three commensal species reconstructions.

Compared to the healthy case, the introduction of taurocholate was predicted to increase the local *C. difficile* growth rate across the biofilm (Figure 4.5A). *B. thetaiotaomicron* and *E. coli* growth were largely unaffected, while the *F. prausnitzii* growth rate decreased due to increased competition for succinate from *C. difficile*. As a result, the *C. difficile* abundance increased from 1% to 18%, while the *F. prausnitzii* abundance decreased by 38% (Figure 4.5B). The *B. thetaiotaomicron* and *E. coli* abundances exhibited relatively small decreases, although experimental studies show that *E. coli* abundance should increase during dysbiosis [204, 206]. The total biomass concentration was predicted to remain almost constant, showing that taurocholate was responsible for changing the species distribution of the biomass.

The predicted trends for SCFA and OA levels were similar to those observed for the combined glucose/amino acid perturbation. Acetate and total SCFA concentrations increased compared to the healthy case due to increased acetate synthesis by *C. difficile* and decreased acetate consumption by *F. prausnitzii* (Figure 4.5C). The formate concentration decreased because of the same mechanism, while we attributed the reduced succinate concentration to increased succinate consumption by *C. difficile* (Figure 4.5D). Butyrate (produced by *F. prausnitzii* and *C. difficile*) and propionate (produced by *B. thetaiotaomicron* and *C. difficile*) concentrations remained almost constant as *C. difficile* compensated for reduced SCFA synthesis by the two commensal species. We also simulated a host-microbiota perturbation with decreased glucose/increased amino acids and increased taurocholate to examine the combined effects of these nutrient changes. Compared to either perturbation alone, the model predicted a further increase in *C. difficile* abundance and decrease in *F. prausnitzii*

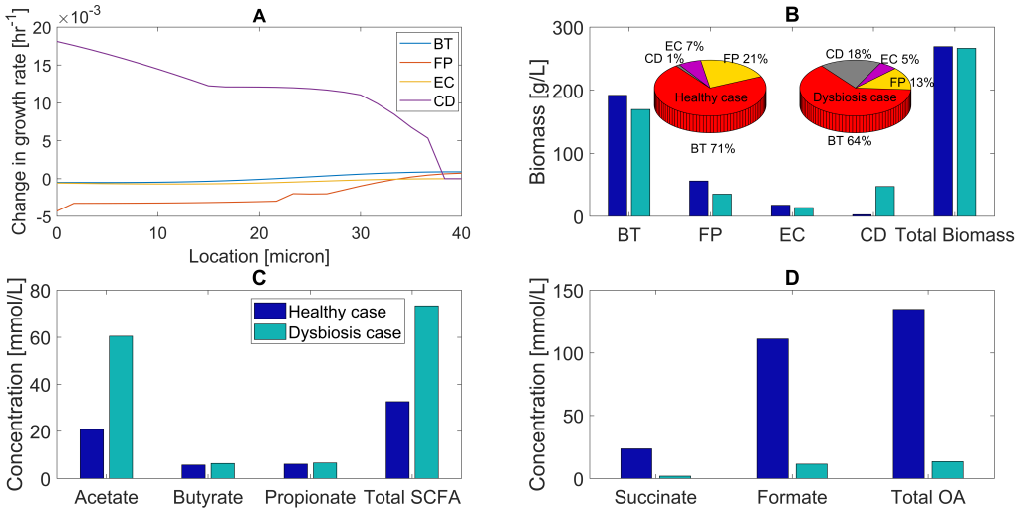

Figure 4.5: Predicted multispecies biofilm dysbiosis resulting from host-microbiota perturbations in the concentration of the primary bile acid taurocholate. (A) Change in species growth rates across the biofilm plotted as the difference between the growth rates for the healthy and dysbiosis case. (B) Biomass concentrations (bar graphs) and species abundances (pie charts) averaged across the biofilm for healthy and dysbiosis case. (C) Acetate, butyrate, propionate and total SCFA concentrations averaged across the biofilm. (D) Succinate, formate and total OA concentrations averaged across the biofilm.

abundance (not shown here). Overall, these results support the hypothesis that increased primary bile acid levels could contribute to *C. difficile* propagation *in vivo*.

4.3.5 Host-derived nitrate perturbations

The human host is known to secrete nitrate in response to inflammation in the gut [33]. Preliminary FBA calculations showed that nitrate uptake increased the *E. coli* growth rate, while the other three community members were unable to use nitrate as an electron acceptor. Therefore, we hypothesized that host-derived nitrate would increase *E. coli* abundance during simulated *C. difficile* associated dysbiosis and yield better agreement with experimental studies [204, 206]. To quantify the effects of nitrate availability, biofilm simulations were performed with and without nitrate for a dysbiosis case with reduced glucose, increased amino acids and available taurocholate (Table 4.2).

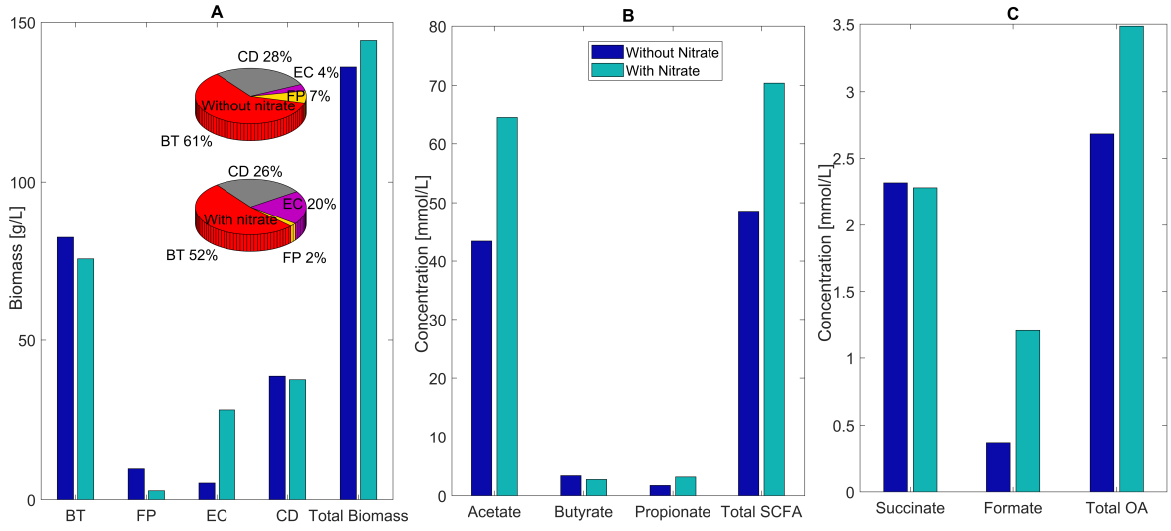

Figure 4.6: Predicted multispecies biofilm dysbiosis with and without host-derived nitrate. (A) Biomass concentrations (bar graphs) and species abundances (pie charts) averaged across the biofilm for healthy and dysbiosis case. (C) Acetate, butyrate, propionate and total SCFA concentrations [mmol/L]averaged across the biofilm. (D) Succinate, formate and total OA concentrations averaged across the biofilm.

As hypothesized, the main impact of host-derived nitrate was to substantially increase *E. coli* abundance from 4% without nitrate to 20% with nitrate (Figure 4.6A). The *F. prausnitzii* abundance decreased from 7% to 2%, while the abundances of *B. thetaiotaomicron* and *C. difficile* decreased modestly to accommodate the increased *E. coli*. The species abundances predicted with nitrate are in good agreement with experimental studies for *C. difficile* associated dysbiosis showing large increases in *C. difficile* and *E. coli*, large decreases in *F. prausnitzii* and modest changes in *B. thetaiotaomicron* [218–220].

Nitrate availability was predicted to substantially increase the acetate and total SCFA concentrations due to large changes in *E. coli* and *F. prausnitzii* abundances (Figure 4.6B). Decreased succinate consumption by *F. prausnitzii* and increase formate synthesis by *E. coli* results in increase levels of individual and total OAs (Figure 4.6C). These predictions implicate a role for host-derived nitrate in *C. difficile* associated dysbiosis.

4.4 Discussion

The gut microbiota serve a broad array of important functions for the human host, including providing colonization resistance to opportunistic pathogens. Unhealthy changes in the microbiota composition, commonly termed dysbiosis, have been correlated to a wide variety of gut and metabolic diseases including inflammatory bowel disease, Crohn's disease, obesity, diabetes and chronic gut infections. The opportunistic gut pathogen *Clostridium difficile* has been estimated to asymptomatically colonize 3%–15% of healthy adults [44]. A common cause of symptomatic *C. difficile* infection (CDI) is the use of broad spectrum antibiotics, which induce dysbiosis by reducing the diversity and density of gut commensal bacteria that provide resistance to *C. difficile* expansion [46–49, 211]. Improved understanding of the complex interactions between commensal species, *C. difficile*, the gut environment and the human host are needed to more rationally treat CDI.

To help unravel the metabolic determinants of *C. difficile* associated dysbiosis, we developed a multispecies biofilm model by combining genome-scale metabolic reconstruction of *C. difficile* [181] and commensal species representing the three dominant phyla in the gut: *Bacteroides thetaiotaomicron* (Bacteroidetes) [182], *Faecalibacterium prausnitzii* (Firmicutes) [183] and *Escherichia coli* (Proteobacteria) [184]. The chosen species are well-studied representatives of the most dominant phyla in human gut microbiome and curated metabolic reconstructions of these species are available. While specific spatial organization of gut microbes is currently unknown, the structure likely includes biofilm growth associated with host mucosa and epithelial tissue [221]. The literature provides significant evidence to support the hypothesis that some gut microbes develops spatially structured multispecies biofilms [174, 172]. We sought to understand how the commensal species could sublimate *C. difficile* expansion and under what gut conditions colonization resistance could become compromised. The biofilm model was tuned to represent a healthy state with species abundances and

concentrations of short-chain fatty acids (SCFAs; acetate, butyrate, propionate) consistent with experimental studies for healthy individuals [21, 196, 189] Because our model lacked an explicit description of the human host, we mimicked host-microbiota perturbations associated with CDI by varying nutrient levels guided by experimental observations. More specifically, dysbiosis states were modeled through changes in the concentrations of available glucose, amino acids [28, 191–194], primary bile acids [32, 214, 210] and nitrate [33].

Our model predicted that crossfeeding of secreted byproducts plays an important role in *C. difficile* sublimation and expansion. *C. difficile* consumed formate synthesized by *F. prausnitzii* and *E. coli* and succinate synthesized by *B. thetaiotaomicron* and *F. prausnitzii*. The existence of both crossfeeding relationships is supported by the experimental literature [197, 198]. *In silico* removal of either crossfeeding relationship was predicted to provide *C. difficile* colonization resistance, demonstrating the complexity and importance of crossfeeding networks even in this simplified four-species community. More importantly, these results suggest therapeutic strategies that target species-species interactions could be promising alternatives to conventional antibiotics that target *C. difficile* directly.

Host-microbiota perturbations modeled as increases in glucose and decreases in amino acid concentrations reproduced several feature of *C. difficile* associated dysbiosis including substantially reduced *F. prausnitzii* and increased *C. difficile* abundances and an imbalance in SCFA synthesis characterized by increased acetate and reduced butyrate levels [222]. The predicted decrease in anti-inflammatory butyrate would be expected to exasperate dysbiosis and accelerate disease progression [202, 207]. Similar predictions were obtained when glucose and amino acid changes were replaced by increases in the primary bile acid taurocholate, which can be used as an electron acceptor by *C. difficile in vivo* to provide a growth advantage in the absence of commensal bacteria that degrade primary bile acids to secondary bile acids [191, 223, 224].

Taurocholate availability was predicted to have less effect on butyrate and propionate synthesis, but the SCFA imbalance remained due to high acetate synthesis. Our model predicted that dysbiosis could be induced with moderate changes in nutrient concentrations, suggesting the possible promise of therapeutic strategies that aim to alter the gut nutritional environment.

Despite their many consistencies with experimental studies [28, 225, 226], our simulations with glucose, amino acids and taurocholate changes were unable to reproduce the large increase in *E. coli* abundance observed during CDI [204, 206]. The addition of host-derived nitrate [33, 227] to the other nutrient changes rectified this inconsistency and reproduced the key microbiota signatures of *C. difficile* associated dysbiosis during CDI: large increases in *C. difficile* and *E. coli* abundances, large decreases in health-promoting *F. prausnitzii* abundance and moderate changes in *B. thetaiotaomicron* abundance. We believe further development of our multispecies biofilm model could yield a general computational platform for *in silico* investigation of CDI, other gut infections and chronic inflammation disorders such as inflammatory bowel and Crohn's diseases. Some possibilities include the modeling of *C. difficile* spore formation/germination, the inclusion of more commensal gut species (*e.g.* [228]) including those from other phyla [229–231], the addition of a broader array of gut nutrients including fibers, oligosaccharides and fats resulting from realistic diets [28–31, 232], and modeling of the human host through incorporation of available metabolic reconstructions such as Recon 2 or Recon 3D [233–235]. A possible drawback of our modeling approach is the lack of species-specific parameters for nutrient uptake kinetics and metabolite-dependent mass transfer coefficients.

4.5 Conclusions

Clostridium difficile infection (CDI) is a common problem in hospital settings, with almost 500,000 CDI cases diagnosed within the U.S. annually in acute care facil-

ities alone. CDI involves dysbiosis of the commensal gut microbiota characterized by a significant reduction of butyrate producing species *e.g. Faecalibacterium prausnitzii* and a large increase in Proteobacteria *e.g. Escherichia coli* along with uncontrolled propagation of *C. difficile*. Motivated by recent experimental studies demonstrating the ability of *C. difficile* and commensal gut bacteria to form biofilms, we developed a multispecies biofilm model with a minimal representation of the gut microbiota containing *C. difficile* and one species each from the three dominant phyla (*F. prausnitzii*, *E. coli*, *Bacteroides thetaiotaomicron*). The model was used to investigate possible metabolic determinants of CDI mediated through host-microbiota perturbations, modeled as decreased carbohydrate levels and increased amino acid, primary bile acid and nitrate levels compared to the healthy gut. These nutrient perturbations were shown to mimic microbiota changes characteristic of CDI, namely marked increases in *C. difficile* and *E. coli*, abundances and a sharp decrease in *F. prausnitzii* abundance. *C. difficile* propagation was strongly dependent on crossfeeding of formate and succinate secreted by the commensal species, a prediction in agreement with experimental studies and that provides possible targets for the development of novel therapeutic strategies. While our model is a simplified representation of a complex disease process, the results presented emphasized the importance of metabolic interactions between *C. difficile* and commensal species in CDI progression.

CHAPTER 5

METABOLIC MODELING OF CHRONIC WOUND MICROBIOTA PREDICTS MUTUALISTIC INTERACTIONS THAT DRIVE COMMUNITY COMPOSITION

5.1 Introduction

Chronic wounds are usually colonized by microbial communities rather than single bacterial species [54–56, 65, 66]. Polymicrobial infections often require about 12+ months to clear, have recurrence frequencies of 60 to 70% [236, 237] and have elevated mortality rates as compared to single-species infections [67]. *In vivo* rabbit models have demonstrated that polymicrobial infections slow wound healing compared to their respective monoculture infections [61, 68].

Culture- and molecular-based methods have been used to analyze chronic wound communities [62, 238, 239]. The most common genera represented in chronic wound infections are *Staphylococcus*, *Corynebacterium*, *Pseudomonas*, *Streptococcus*, *Enterococcus*, *Enterobacter*, *Finegoldia* and *Serratia* [54, 55, 65, 240–243]. *Staphylococcus aureus* and *Pseudomonas aeruginosa* are the two most common bacterial pathogens observed in chronic wound infections. These two pathogens have been shown to establish mutualistic interactions including metabolite crossfeeding that allows them to resist antibiotic treatment in multiple types of infection environments including chronic wounds and the cystic fibrosis lung [244, 118, 245, 246]. Mutualistic relationships between pathogens reduce competition for available nutrients and result in robust communities associated with prolonged infections and poor clinical outcomes [247]. Chronic wound pathogens also form mutualistic relationships with skin com-

mensal species that impact their virulence [248, 139, 249]. These interactions allow pathogens to survive at infection sites, enhance antibiotic resistance and increase disease severity [57, 250, 149, 251]. More detailed knowledge about the mechanisms underlying these interspecies relationships offers the potential for developing novel treatment strategies based on disrupting specific mutualistic interactions rather than just targeting specific pathogens.

In this study, We have used our *in silico* computational methods and 16S rDNA pyrosequencing data collected from 2,963 chronic wound patients [1] to develop a bacterial community model for investigation of pathogen-pathogen and pathogen-commensal interactions. The dataset contained abundances (i.e. the relative amount of the genera averaged across samples) of the 20 most abundant genera for each type of chronic wound, diabetic foot ulcers, venous leg ulcers, pressure ulcers and non-healing surgical wounds, as well as prevalences (i.e. the fraction of samples containing the genus). Because the original study [1] concluded that the average bacterial community present at each wound location were not significantly different, the average abundance data for each wound type was assimilated into a combined dataset and used to construct a single 12 species community model representing the most abundant pathogenic and commensal genera. Simulation results were performed and analyzed to identify putative mutualistic interactions that could drive community composition and negatively impact the effectiveness of antibiotic treatments.

5.2 Materials and methods

5.2.1 Community metabolic model

16S rDNA pyrosequencing data was obtained from a published study which analyzed chronic wound samples from 2,963 patients treated for decubitus ulcers (767 samples), diabetic foot ulcers (910 samples), venous leg ulcers (916 samples) and non-healing surgical wounds (370 samples) [1]. The publication provided relative

Table 5.1: The 12 species included in the chronic wound community model along with the prevalences and normalized average abundances of the associated genera from [1].

Number	Strain	References	Prevalence (%)	Relative abundance
1	*Staphylococcus aureus* subsp *aureus* USA300 FPR3757	[238, 239, 1]	63	0.42
2	*Pseudomonas aeruginosa* NCGM2 S1	[238, 239, 1]	25	0.13
3	*Corynebacterium striatum* ATCC 6940	[54, 238, 1]	36	0.11
4	*Streptococcus agalactiae* A909	[238, 1]	23	0.07
5	*Enterococcus faecalis* V583	[239, 252]	17	0.05
6	*Finegoldia magna* ATCC 29328	[54, 1]	25	0.05
7	*Anaerococcus vaginalis* ATCC 51170	[238, 253]	24	0.05
8	*Stenotrophomonas maltophilia* D457	[238, 1]	19	0.04
9	*Prevotella bivia* DSM 20514	[1, 253]	12	0.03
10	*Acinetobacter baumannii* AB0057	[238, 253]	9	0.02
11	*Serratia liquefaciens* ATCC 27592	[62, 254]	5	0.02
12	*Bacteroides fragilis* 3 1 12	[253, 255]	8	0.02

abundances of the top 20 bacterial genera for each wound types. Community composition was shown to be independent of the wound type and patient demographics such as age, gender and race. Therefore, we assimilated the average abundance data for each wound type into a single dataset and determined the most abundant genera across all samples. To limit model complexity and focus on the most dominant genera, the community model accounted for the 12 genera with highest average abundances (Figure 5.1A). These 12 genera accounted for approximately 74% of the 16S read data averaged across all 2,963 samples. To allow direct comparison with community model predictions, the 16S data was normalized such that the abundances of these 12 genera summed to unity. A representative species for each genus was selected from the AGORA database (www.vmh.life) [77] according to its documented presence in chronic wound infections (Table 5.1). The genome-scale metabolic reconstructions for the 12 species accounted for 16,133 reactions, 13,666 metabolites and 9,713 genes.

5.2.2 Model tuning and simulation

The nutrient environment in chronic wound is complex and expected to vary between patients and according to disease progression. A metabolomics study conducted for four chronic pressure ulcer samples detected 122 metabolites with the quantified metabolite concentrations spanning several orders of magnitude. Several studies have

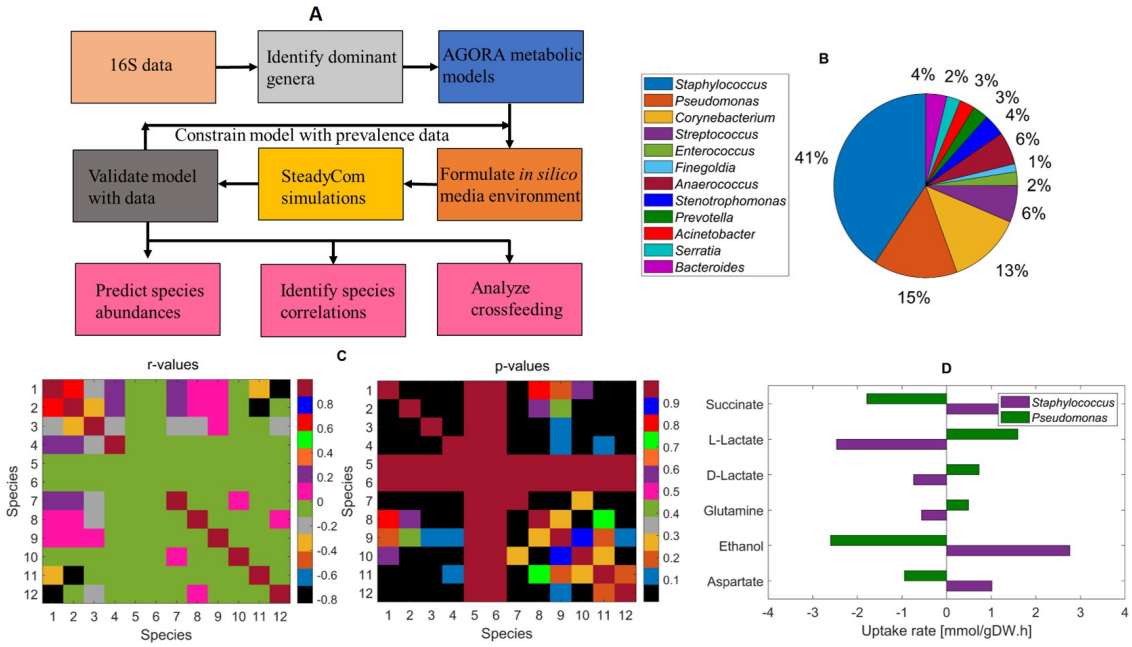

Figure 5.1: Overview of the community modeling framework. (A) Flow chart showing steps in model development, simulation and analysis. (B) Average species abundances obtained from the model ensemble. (C) r and p values obtained from correlation analysis of the model ensemble abundance data. (D) Significant crossfeeding relationships between *Staphylococcus* and *Pseudomonas* predicted by model ensemble simulations.

identified upregulated or downregulated metabolites in chronic wounds compared to healing wounds, but absolute metabolite concentrations were not reported [256–258]. The *in vitro* Lubbock chronic wound biofilm model based on chopped meat-based media (Bolton broth, MRS broth and BHI broth) has been shown to contain nutrients present in chronic wound beds [259]. While these studies provided important guidance on nutrient selection for the community model, they were not sufficient to completely define a nutrient environment in which all 12 species were capable of growth and the predicted species abundances were in approximate agreement with the 16S data [1] used in this study.

Therefore, our approach previously used to specify nutrients for a community model of the adult cystic fibrosis microbiota [76] was followed. First, all 21 amino acids and 6 carbon sources (glucose, L-lactate, ribose, galactose, L-arabinose, fructose) known to be available in chronic wound beds were added. Then 15 common metals and ions and 30 metabolites that were required for each species to grow in simulated monoculture were included. The metabolites guanosine, inosine, uracil and uridine [256, 257] and the terminal electron acceptors O_2 and NO_3 were added because they are known to be present in the chronic wound environment. Finally, three putative metabolites were added to increase the growth rates of particular species such that predicted species abundances were in approximate agreement with the 16S data: starch 1 for *Corynebacterium*; kestose for *Enterococcus* and; glycerol-3-phosphate for *Prevotella*.

The 81 metabolites contained in the simulated chronic wound environment were partitioned into 19 groups for the purpose of model tuning: (1) 15 metals and ions; (2) 30 essential growth metabolites; (3)-(6) each of the 4 chronic wound metabolites guanosine, inosine, uracil and uridine: (7) 17 amino acids; (8) 4 amino acids isoleucine, leucine, lysine and valine reported to be elevated in chronic wounds compared to the other 17 amino acids [258]; (9)-(14) each of the 6 carbon sources; (15) O_2; (16)

NO_3; (17) starch 1; (18) kestose; and (19) glycerol-3-phosphate. The community uptake rates of metabolites in these 19 groups were tuned by trial-and-error to achieve approximate agreement with the 16S data (see Figure 5.1C).

The SteadyCom method [74] was used to formulate and solve the chronic wound community model as described in our previous studies on the human gut microbiota [75] and cystic fibrosis [76]. The SteadyCom method uses a form of community flux balance analysis to calculate the relative abundance of each species with an objective of maximizing the community growth rate. The non-growth associated ATP maintenance for each species was chosen to be 5 mmol/gDw/h, which is in reported ranges for curated bacterial reconstructions [184]. Individual species simulations were performed to ensure that each species was able to grow in monoculture on the *in silico* media. In addition to providing the community growth rate and species abundances, SteadyCom calculated species-dependent uptake and secretion rates of all supplied and secreted metabolites.

The community model was further constrained with genus prevalence data (i.e. the fraction of samples containing the genus) available in the original experimental study [1]. To implement these constraints, the participating species of the community were randomly chosen according to the prevalences using uniform random numbers and then the model was solved. A large number of models were solved to adequately sample the species participation space. A total of 5,250 model ensemble simulations were performed with 250 cases discarded because the community growth rate was zero or the SteadyCom tolerance on the sum of the species abundances was not satisfied. The remaining 5,000 cases were treated as simulated patient samples and their abundances were averaged (Figure 5.1B). The community uptake rates of the 81 supplied metabolites were further tuned to achieve quantitative agreement with the 16S data (see Figure 5.1D).

5.2.3 Analysis of simulation results

The difference (e) between the normalized 16S abundances (p_{id}) and the model predicted abundances (p_{im}) was calculated as the angle between the two abundance vectors [260],

$$e = sin\left[cos^{-1}\left(\frac{p_{im}^T p_{id}}{\|p_{im}\|\|p_{id}\|}\right)\right] \tag{5.1}$$

where $\|\cdot\|$ denote the Euclidean norm and $e \in [0, 1]$. The two abundance vectors were identical (i.e. parallel) if $e = 0$ and orthogonal if $e = 1$. The inverse Simpson equitability index (D_{com}) was used as a measure of community diversity [75],

$$D_{com} = \frac{1}{N}\frac{1}{\sum_{i=1}^{N} p_i^2} \tag{5.2}$$

where $N = 12$ is the total number of species and p_i is the 16S determined or model predicted abundance of the species i. Significant crossfeeding relationships were identified based on the magnitudes of the secretion and uptake fluxes as detailed in our previous study [75]. We typically reported the top six crossfeeding relationships between the participating species (Figure 5.1D).

Staphylococcus and *Pseudomonas* are the most common genera in chronic wound infections [65, 61, 243, 261–263] and are known to exhibit strong interactions. Correspondingly, we were interested in community behavior with the presence and absence of these two dominant pathogens. Therefore, the ensemble of 5,000 community simulations was partitioned into four groups: both *Staphylococcus* and *Pseudomonas* present (SaPa); *Pseudomonas* not present (SaΔPa); *Staphylococcus* not present (ΔSaPa); and neither *Staphylococcus* or *Pseudomonas* present (ΔSaΔPa). For the entire ensemble and each of the four partitioned subsets, mutualistic interactions between species were identified by performing correlation analysis on the predicted abundance data (Figure 5.1C). An interaction was deemed significant if the r-value was greater than 0 and p-value was less than 0.05.

5.3 Results

5.3.1 Community composition is shaped by single-species metabolism

Monoculture simulations were performed with the *in silico* nutrients to access the metabolic capabilities of the 12 species. *Staphylococcus* was predicted to have the highest single-species growth rate (Figure 5.2A), consistent with its role as a dominant chronic wound pathogen. *Serratia*, *Stenotrophomonas* and *Pseudomonas* had growth rates greater than 0.3 h^{-1}, suggesting that these species would be competitive in community simulations. Of 9 metabolites commonly found in the chronic wound environment [256], acetate, CO_2 and formate were the primary secreted byproducts predicted from monoculture simulations (Figure 5.2B). Interestingly neither L-lactate or D-lactate secretion was predicted even though species from genera such as *Streptococcus* are well known to secrete L-lactate as a primary byproduct [264, 265]. As discussed in our study on cystic fibrosis communities [76], this model behavior was attributable to alternative optima with respect to byproduct secretion patterns.

When the community model was simulated without prevalence constraints, 7 of the 12 species were predicted to coexist (Figure 5.2C). Consistent with the normalized 16S data, *Staphylococcus* was the dominant species and both *Pseudomonas* and *Corynebacterium*) were present at abundances greater than 10%. However, the model overpredicted the abundances of *Acinetobacter*, *Serratia* and *Bacteroides* and incorrectly predicted zero abundances for 5 other species. The difference e between the predicted and 16S abundance vectors was 0.38, denoting a moderate prediction error. This difference was not unexpected, as the 16S data was provided as the average over a large number of patient samples while the simulation represented a single predicted sample [76]. As a result, the normalized 16S data exhibited a greater species diversity ($D_{com} = 0.38$) than the simulated sample ($D_{com} = 0.36$). The predicted species abundances were strongly correlated to the single-species growth rates ($r = 0.72$, $p = 0.009$; Figure 5.2D), as expected for a community modeling method such

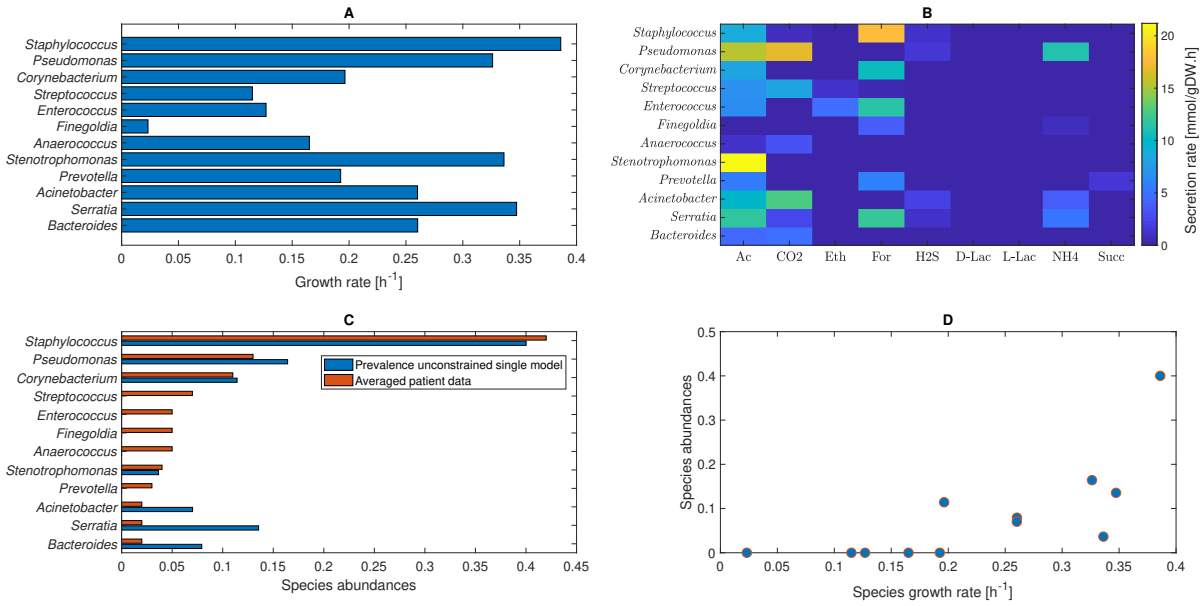

Figure 5.2: Model predictions for monoculture simulations and a 12 species community simulation without prevalence constraints. (A) Single-species growth rates (h^{-1}) where the species are listed by their genera. (B) Single-species secretion rates predicted from monoculture simulations for the byproducts acetate (Ac), CO_2, ethanol (Eth), formate (For), H_2S, D-lactate (D-Lac), L-lactate (L-lac), NH_4 and succinate (Succ). (C) Comparison of species abundances predicted from the 12 species community model without prevalence constraints and obtained from normalized 16S patient data. (D) Relationship between single-species growth rates and species abundances predicted from the community simulation ($r = 0.72$, $p = 0.009$).

as SteadyCom based on growth rate maximization. An sublinear correlation was predicted because some species were more/less efficient at metabolite crossfeeding. For example, *Pseudomonas* had the fourth highest monoculture growth rate but the second highest abundance.

5.3.2 Incorporation of genera prevalence data improves prediction of community composition

A single model simulation with all 12 species allowed to participate in the community only provided qualitative agreement with normalized 16S data with respect to the abundances of the dominant genera (Figure 5.2). We hypothesized that incorporation of genera prevalence data as additional constraints would improve model predictions with respect to the coexisting species and their abundances. Given that the 16S abundances were obtained by averaging over 2,963 patient samples, we used prevalence data reported in the original study [1] to generate an ensemble of 5,000 *in silico* communities by randomly generating the species allowed to participate (see Materials and Methods). Then the predicted abundances were averaged over the ensemble for comparison to 16S values. This approach was consistent with the constraints-based philosophy of metabolic modeling based on the refinement of model predictions through the imposition of additional data-based constraints [266, 267]. Even if allowed to participate in a community, a particular species could be predicted to have a zero abundance. Therefore, participation was a necessary but not sufficient condition for a species to coexist in a simulated community. Below we used the terms "prevalence" and "participation" interchangeably with respect to the model ensemble simulations for simplicity.

A comparison of the genera prevalence data and the *in silico* prevalences of the corresponding modeled species showed a slight bias even through the model ensemble was generated with the intent of these prevalences being identical (Figure 5.3A). This

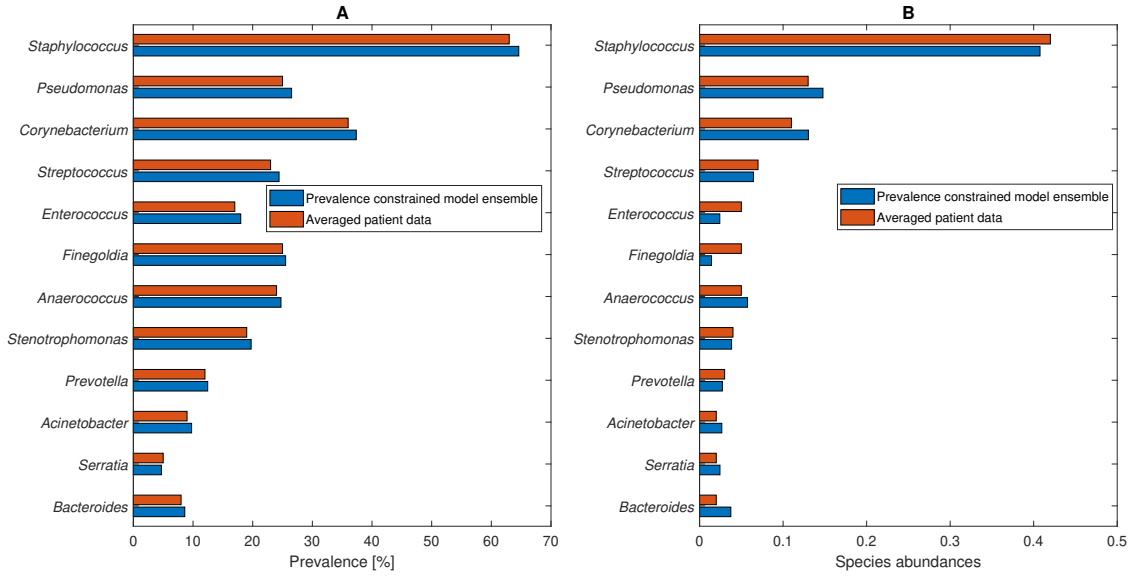

Figure 5.3: Prevalence constrained model ensemble predictions. (A) Comparison of genera prevalence data [1] and *in silico* prevalences of the corresponding modeled species. (B) Comparison of species abundances predicted from the model ensemble with species prevalence constraints and normalized 16S patient data.

disparity was caused by the need to discard 250 of 5,250 total simulation cases because the community growth rate was zero or the SteadyCom tolerance on the sum of the species abundances was not satisfied. The removal of these 250 cases introduced a small systematic bias into the *in silico* prevalences as most species were advantaged by being allowed to participate more frequently than indicated by data. Despite this small bias, the model ensemble generated substantially improved predictions of the 16S-derived abundances ($e = 0.12$; Figure 5.3A) compared to the prevalence unconstrained model ($e = 0.38$; Figure 5.2). As expected, the model prevalences and abundances were strongly correlated ($r = 0.91$, $p = 5\text{x}10^{-5}$). While the abundances of some minor species were substantially underpredicted (e.g. *Enterococcus*) or overpredicted (e.g. *Bacteroides*), we deemed these prediction to be sufficiently accurate to utilize the model ensemble for further analysis of the chronic wound community.

5.3.3 Analysis of community structure and composition

We defined the richness of the community as the number of species with abundances exceeding 1%. To further investigate the effect of imposing prevalence constraints in the ensemble of 5,000 models, we calculated the number of species allowed to participate in each community (Figure 5.4A) and the actual richness of each community (Figure 5.4B). Over 90% of the simulations allowed no more than 4 species, with the most likely cases being 2 or 3 species. Because some species allowed to participate were predicted to have zero abundances, the predicted richness was generally less than the number of participating species. Over 90% of the simulated communities had richnesses of no more than 3 species. Therefore, the model ensemble predicted that most individual patient samples would have low diversity. The original study [1] did not provide data on individual samples that would allow comparison with these modeling results.

Because *Staphylococcus* and *Pseudomonas* are the two dominant pathogens in chronic wound infections [65, 61, 243, 261–263], we partitioned the ensemble of 5,000 community models into four groups based on the allowed participation of these two species (see Materials and Methods): both *Staphylococcus* and *Pseudomonas* present (SaPa); *Pseudomonas* not present (SaΔPa); *Staphylococcus* not present (ΔSaPa); and neither *Staphylococcus* or *Pseudomonas* present (ΔSaΔPa). Each group was populated by a sufficient number of models to allow statistical analysis of the impact of each dominant pathogens on community structure and species interactions (Figure 5.4C). The SaPa group was predicted to have the highest average growth rate with little variability except for some outliers (Figure 5.4D). The growth rate decreased and variability increased as *Pseudomonas* (SaΔPa), *Staphylococcus* (ΔSaPa) or both species (ΔSaΔPa) were removed from the communities. These predictions suggest mutualistic interactions between the two pathogens and possibly with some commensal species that enhance community fitness.

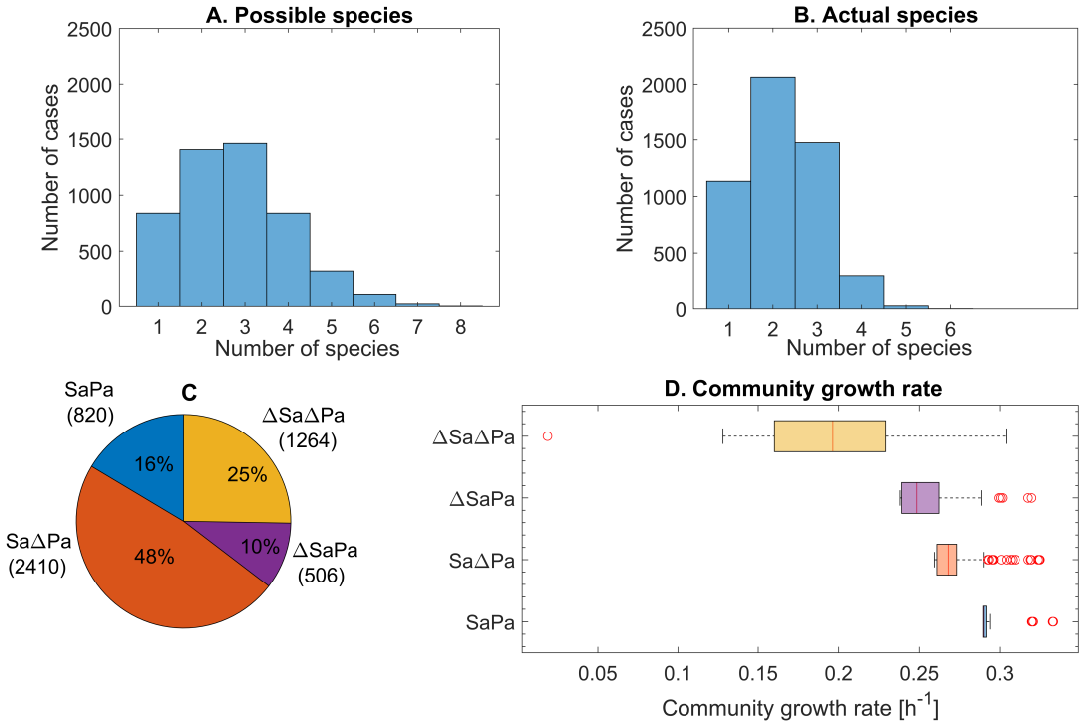

Figure 5.4: Analysis of chronic wound community structure and growth rates. (A) The number of species allowed to participate in each community simulation. (B) The richness (number of species with calculated abundances exceeding 1%) of each simulated community. (C) The percentages and numbers of the 5,000 simulated models in which both *Staphylococcus* and *Pseudomonas* were allowed to participate (SaPa),*Pseudomonas* was not allowed to participate (SaΔPa); *Staphylococcus* was not allowed to participate (ΔSaPa); and neither *Staphylococcus* or *Pseudomonas* were allowed to participate (ΔSaΔPa). (D) A box and whisker plot showing the community growth rates for each of the four partitioned cases, where the red line corresponds to the median, the black dotted lines (whiskers) indicate the variability outside the lower upper quartiles, and the red circles represent outliers.

Interestingly, all outlier communities were characterized by high growth rates with the exception of the ΔSaΔPa group. We analyzed the compositions of these outliers for each group by comparing predicted abundances of the outlier communities to those of communities with outliers removed (not shown here). This analysis revealed several putative mutualistic relationships including: *Serratia* and/or *Bacteroides* with *Staphylococcus* and/or *Pseudomonas*; and *Streptococcus* with *Finegoldia*. The outlier-free cases for the ΔSaΔPa group were predicted to have much higher diversity than the other groups, suggesting that the presence of *Staphylococcus* and/or *Pseudomonas* increased community growth at the expense of diversity. These predictions were consistent with our previously posited hypothesis that infectious disease progression correlates to high growth and low diversity of the evolving community [75].

5.3.4 *Staphylococcus* and *Pseudomonas* form a mutualistic relationship

We used the ensemble of 820 community models in which both dominant pathogens *Staphylococcus* and *Pseudomonas* could participate (SaPa) to identify putative mutualistic interactions between the 12 modeled species. The only significant mutualistic relationship predicted was between the two pathogens themselves (Table 5.2), suggesting that this interaction drove community growth and composition. We performed additional analysis to test this hypothesis. Compared to the average species abundances calculated from the entire 5,000 model ensemble, the 820 SaPa cases produced a much larger *Pseudomonas* abundance such that the abundances of the two dominant pathogens averaged almost 90% (Figure 5.5A). The *Pseudomonas* abundance was greater than the *Staphylococcus* abundance in 780 communities (Figure 5.5B), indicating that *Pseudomonas* was the primary beneficiary of the mutualistic interaction.

The SaPa model ensemble predicted a significant positive correlation ($r = 0.53$, $p < 10^{-6}$) between community equitability and growth rate (Figure 5.5C). These

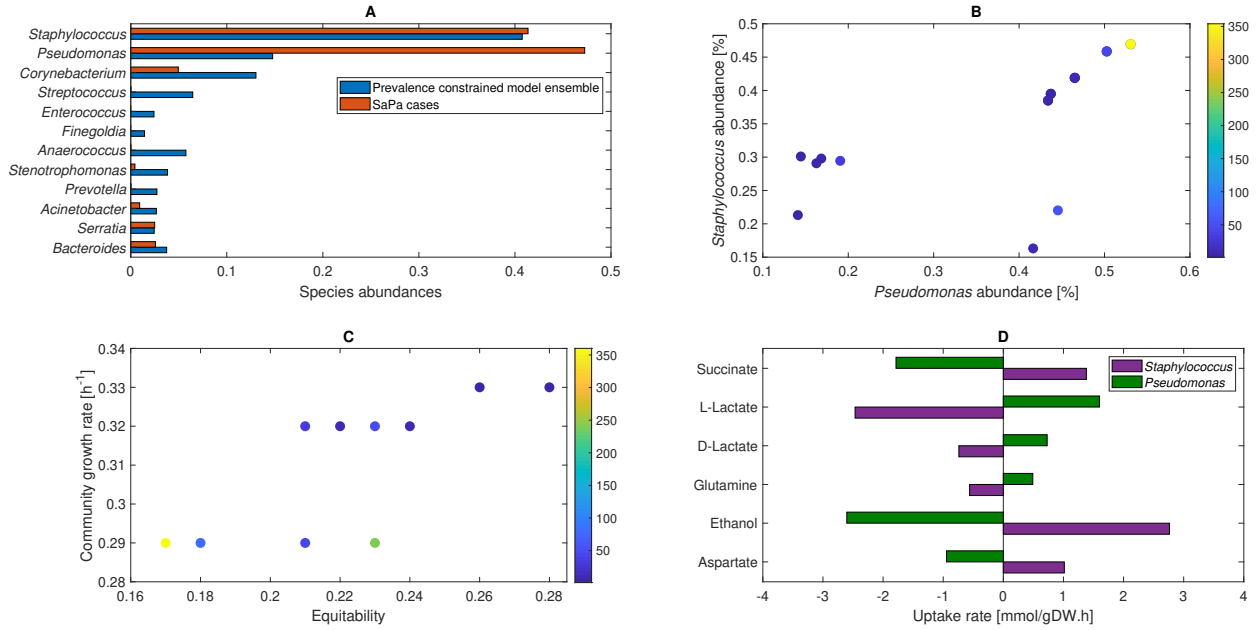

Figure 5.5: Model ensemble predictions for SaPa simulations showing a mutualistic relationship between *Staphylococcus* and *Pseudomonas*. (A) Average species abundances for all 5,000 ensemble simulations and 820 SaPa simulations. (B) *Staphylococcus* and *Pseudomonas* abundances for 820 simulated communities containing both species where the colorbar indicates the number of simulations represented by each circle. The two species show a mutualistic interaction ($r = 0.69$, $p < 10^{-6}$). (C) Community growth rates and equitability for 820 simulated communities containing both species. (D) The six most significant crossfeeding relationships between the two species.

Table 5.2: Species abundance correlation analysis.

Group	**Positively correlated species**	r **value**	p **value**	**Number of cases**	**Analysis**
SaPa	*Staphylococcus* and *Pseudomonas*	0.69	<10e-6	820	Figure 5.5
SaΔPa	*Staphylococcus* and *Acinetobacter*	0.57	<10e-6	235	Figure 5.6
SaΔPa	*Staphylococcus* and *Corynebacterium*	0.22	<10e-6	895	Not shown
PaΔSa	*Pseudomonas* and *Serratia*	0.88	<10e-6	18	Figure 5.7
PaΔSa	*Pseudomonas* and *Streptococcus*	0.72	<10e-6	125	Not shown
PaΔSa	*Pseudomonas* and *Acinetobacter*	0.41	<10e-2	42	Not shown
PaΔSa	*Pseudomonas* and *Bacteroides*	0.4	<1e-2	39	Not shown
ΔSaΔPa	*Corynebacterium* and *Stenotrophomonas*	0.6	<10e-6	107	Not shown
ΔSaΔPa	*Corynebacterium* and *Serratia*	0.5	<1e-2	24	Not shown
ΔSaΔPa	*Corynebacterium* and *Bacteroides*	0.6	<10e-6	41	Not shown
ΔSaΔPa	*Streptococcus* and *Enterococcus*	0.53	<10e-6	51	Figure 5.8
ΔSaΔPa	*Streptococcus* and *Acinetobacter*	0.46	<10e-3	30	Not shown
ΔSaΔPa	*Streptococcus* and *Serratia*	0.61	<1e-1	12	Not shown
ΔSaΔPa	*Streptococcus* and *Bacteroides*	0.92	<10e-6	30	Not shown
ΔSaΔPa	*Enterococcus* and *Finegoldia*	0.78	<10e-6	66	Not shown
ΔSaΔPa	*Enterococcus* and *Stenotrophomonas*	0.3	<1e-2	63	Not shown
ΔSaΔPa	*Enterococcus* and *Acinetobacter*	0.91	<10e-6	25	Not shown
ΔSaΔPa	*Enterococcus* and *Bacteroides*	0.98	<10e-6	18	Not shown
ΔSaΔPa	*Finegoldia* and *Anaerococcus*	0.75	<10e-6	85	Not shown
ΔSaΔPa	*Finegoldia* and *Acinetobacter*	0.63	<10e-6	40	Not shown
ΔSaΔPa	*Finegoldia* and *Serratia*	0.86	<10e-6	17	Not shown
ΔSaΔPa	*Finegoldia* and *Bacteroides*	0.51	<1e-2	20	Not shown
ΔSaΔPa	*Anaerococcus* and *Stenotrophomonas*	0.49	<10e-6	73	Not shown
ΔSaΔPa	*Anaerococcus* and *Acinetobacter*	0.8	<10e-6	35	Not shown
ΔSaΔPa	*Anaerococcus* and *Bacteroides*	0.54	<10e-2	28	Not shown
ΔSaΔPa	*Stenotrophomonas* and *Acinetobacter*	0.5	<10e-2	29	Not shown
ΔSaΔPa	*Stenotrophomonas* and *Bacteroides*	1	<10e-6	20	Not shown
ΔSaΔPa	*Prevotella* and *Bacteroides*	0.7	<1e-2	12	Not shown
ΔSaΔPa	*Serratia* and *Bacteroides*	0.83	<1e-2	8	Not shown

results suggest that the incorporation of less abundant commensal species such as *Corynebacterium* enhanced community growth. When combined with predictions that the SaPa ensemble produced the highest growth rates with the lowest variability (Figure 5.4D), these predictions indicate that the mutualistic interaction produced resilient communities not negatively affected by the addition of commensal species. The mutualistic relationship between *Pseudomonas* and *Staphylococcus* was supported by bi-directional metabolite crossfeeding, with ethanol, L-lactate and succinate being the primary crossfed metabolites (Figure 5.5D). Interestingly, L-lactate and D-lactate were not secreted by either species in monoculture (Figure 5.2B) due to alternative optima with respect to byproducts. These predictions suggest that the exchange

of these two byproducts was important for maintaining the interaction. In fact, *Staphylococcus* is known to consume lactate *in vivo* to enhance its competitiveness [268].

5.3.5 *Staphylococcus* and *Acinetobacter* form a mutualistic relationship in the absence of *Pseudomonas*

Next we used the ensemble of 2,410 community models in which *Pseudomonas* was absent (SaΔPa) to predict mutualistic interactions between *Staphylococcus* and the 10 remaining species. Compared to the entire 5,000 model ensemble (Figure 5.6A), the 2,140 SaΔPa simulations produced a substantially higher average *Staphylococcus* abundance and richer communities in which only *Enterococcus* and *Finegoldia* failed to coexist (Figure 5.6A).Two mutualisms involving *Staphylococcus* were identified (Table 5.2); we focused on the *Staphylococcus* and *Acinetobacter* relationship (Figure 5.6B) because the correlation was most positive (i.e. mutualistic) and experimental literature characterizing the interaction was available. Compared to the SaPa cases (Figure 5.5A), the absence of *Pseudomonas* resulted in increased average *Acinetobacter* abundance over the 235 cases in which *Acinetobacter* was allowed to participate.

A significant positive correlation ($r = 0.53$, $p < 10^{-6}$) between community equitability and growth rate was predicted for the SaΔPa model ensemble (Figure 5.6C), suggesting that commensals such as *Streptococcus* enhanced community growth. However, the SaΔPa ensemble produced lower growth rates than the SaPa ensemble (Figure 5.4D) due to the absence of *Pseudomonas*. Therefore, increased richness of the SaΔPa ensemble was accompanied by decreased growth. These predictions are consistent our hypothesis that low abundance of dominant pathogens such as *Pseudomonas* corresponds to an earlier disease stage with relatively low growth and high diversity [75]. Compared to the mutualistic interaction between *Staphylococcus* and

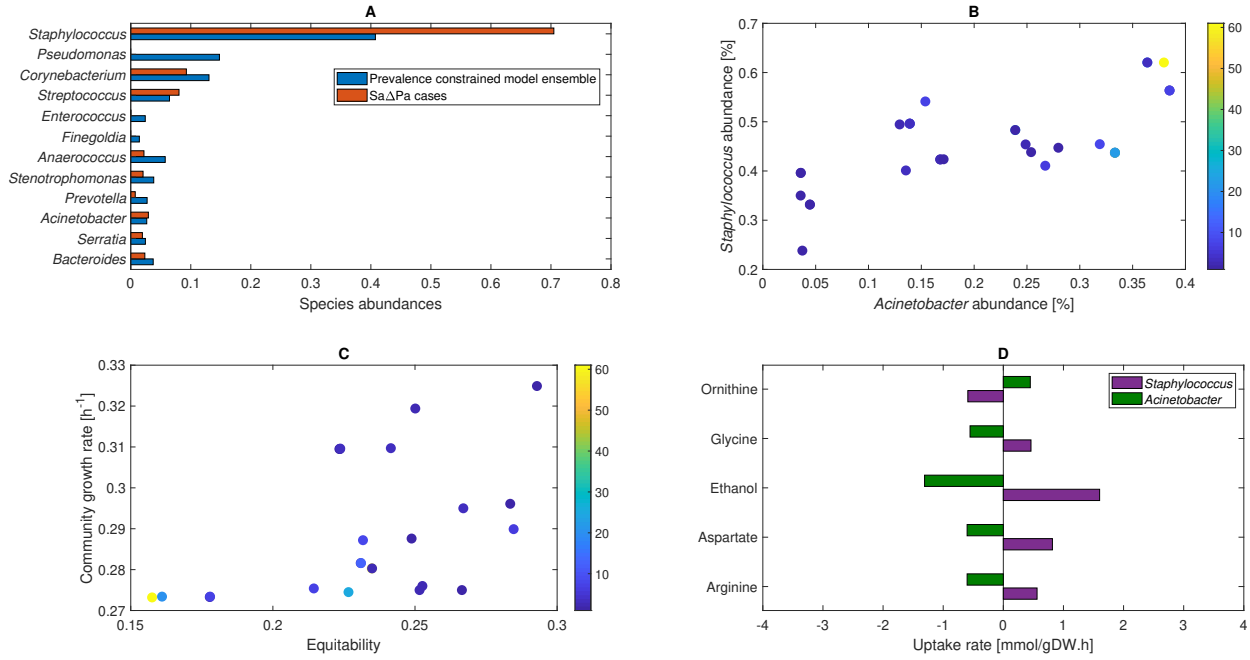

Figure 5.6: Model ensemble predictions for SaΔPa simulations showing a mutualistic relationship between *Staphylococcus* and *Acinetobacter*. (A) Average species abundances for all 5,000 ensemble simulations and 2,410 SaΔPa simulations. (B) *Staphylococcus* and *Acinetobacter* abundances for 235 simulated communities in which both species could participate where the colorbar indicates the number of simulations represented by each circle. The two species showed a mutualistic interaction ($r = 0.57$, $p < 10^{-6}$). (C) Community growth rates and equitability for 235 simulated communities with both species. (D) The five most significant crossfeeding relationships between the two species.

Pseudomonas in the SaPa ensemble (Figure 5.6D), *Pseudomonas* and *Acinetobacter* mutualism was supported by lower crossfeeding rates of amino acids rather than organic acids and alcohols. *Acinetobacter* was predicted to be the primary beneficiary of crossfeeding, explaining its ability to coexist with *Pseudomonas* absent. This predicted mutualistic relationship has experimental support, as *Staphylococcus* and *Acinetobacter* are major nosocomial pathogens involved in burn infections [269–271] and both genera are known to develop antibiotic resistance [272]. These predictions could yield new insights into the treatment of the so-called ESKAPE pathogens (*Enterococcus faecalis*, *Staphylococcus aureus*, *Klebsiella pneumoniae*, *Acinetobacter baumannii*, *Pseudomonas aeruginosa*, *Enterobacter species*) which are the leading cause of nosocomial infections [272, 273].

5.3.6 *Pseudomonas* and *Serratia* form a mutualistic relationship in the absence of *Staphylococcus*

The ensemble of 506 community models in which *Staphylococcus* was absent (ΔSaPa) was analyzed to predict mutualistic relationships between *Pseudomonas* and the 10 remaining species. The ΔSaPa simulations produced a high average *Pseudomonas* abundance and a large increase in the average abundance of *Anaerococcus* (Figure 5.7A); only *Finegoldia* failed to appear in any community. Of the four significant mutualistic relationships predicted (Table 5.2), we focused on *Pseudomonas* and *Serratia* even though the two species were both allowed to participate in only 18 ΔSaPa communities (Figure 5.7B). Interestingly, the average *Serratia* abundance was almost unchanged from the full model ensemble despite *Serratia* having a positive correlation with *Pseudomonas*. Furthermore *Anaerococcus* did not have a significant correlation with *Pseudomonas* despite *Anaerococcus* having a larger average abundance compared to the full model ensemble. These results demonstrate that significant species inter-

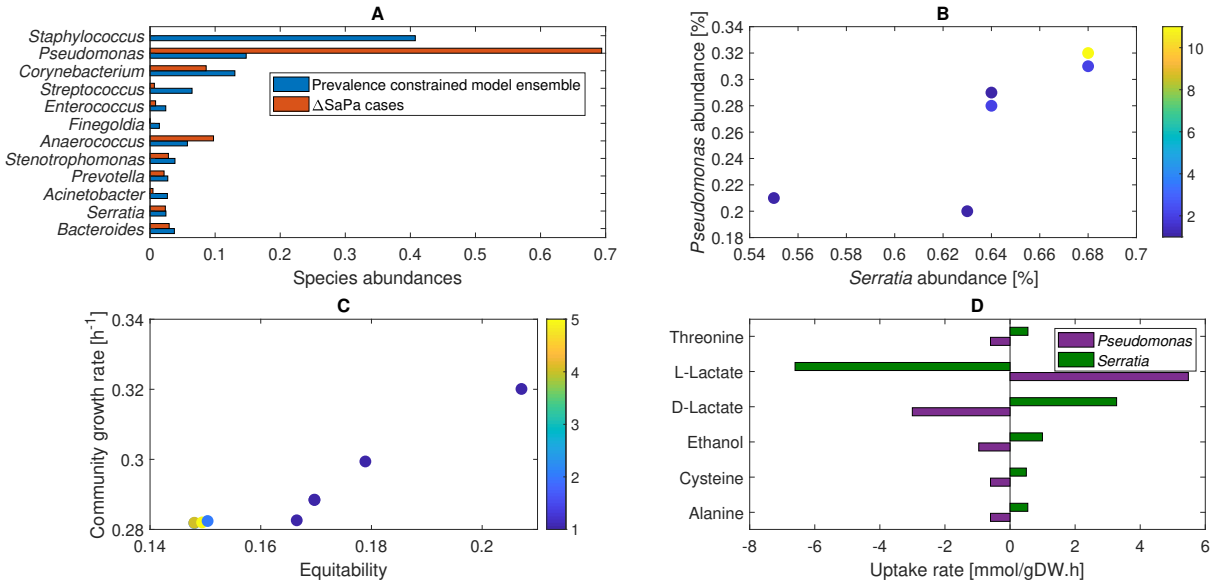

Figure 5.7: Model ensemble predictions for ΔSaPa simulations showing a mutualistic relationship between *Pseudomonas* and *Serratia*. (A) Average species abundances for all 5,000 ensemble simulations and 506 ΔSaPa simulations. (B) *Pseudomonas* and *Serratia* abundances for 18 simulated communities in which both species could participate where the colorbar indicates the number of simulations represented by each circle. The two species showed a mutualistic interaction ($r = 0.88$, $p < 10^{-6}$). (C) Community growth rates and equitability for 18 simulated communities with both species. (D) The six most significant crossfeeding relationships between the two species.

actions cannot easily be discerned from abundance data averaged over heterogeneous samples.

A significant positive correlation ($r = 0.95$, $p < 10^{-6}$) between community equitability and growth rate was predicted for the ΔSaPa model ensemble despite the small number of samples (Figure 5.6C). The mutualistic relationship was primarily supported by lactate crossfeeding, with *Serratia* having a large uptake rate of L-lactate and *Pseudomonas* consuming D-lactate (Figure 5.6D). The ability of *Serratia* to enhance its competitiveness through L-lactate crossfeeding explains why *Serratia* was predicted to be dominant in the 18 ΔSaPa communities in which it appeared (Figure 5.6B). *Pseudomonas* and *Serratia* are often found to coexist in infections associated

with chronic wounds and corneal ulcers [54, 274]. Furthermore, the two genera are known to secrete the quorum sensing molecule N-butanoyl l-homoserinelactone (C4 HSL) which might be used in interspecies communication [275].

5.3.7 *Streptococcus* and *Enterococcus* form a mutualistic relationship in the absence of *Pseudomonas* and *Staphylococcus*

To identify putative mutualistic interactions between less abundant species, we analyzed the ensemble of 1,264 community models in which both *Staphylococcus* and *Pseudomonas* were absent (ΔSaΔPa). This ensemble produced lower and more variable growth rates than the other ensembles due to lack of the two dominant, growth-promoting pathogens (Figure 5.4). This growth reduction was accompanied by an increase in community richness as all 10 remaining species were able to coexist in some communities and no species was predicted to have an average abundance less than 3% (Figure 5.8A). This enhanced richness translated into higher equitabilities than predicted for the other ensembles (Figure 5.8C), again supporting the hypothesis that pathogen emergence results in resilient communities characterized by increased growth and reduced diversity.

Rather than focus on mutualisms with respect to a single species, we used the ΔSaΔPa simulation results to identify mutualistic relationships between any pair of the 10 remaining species (90 possible cases). The analysis produced 23 significant interactions (Table 5.2), suggesting that mutualistic benefits could be spread across more species in the absence of dominant pathogens. For example, the commensal *Corynebacterium* positively interacted with less abundant pathogen *Stenotrophomonas*. We focused on the mutualistic relationship between *Streptococcus* and *Enterococcus* (Figure 5.8B) because these two genera are known to coexist in infections [276, 277]. As before, the community growth rate and equitability were positively correlated ($r = 0.49$, $p = 10^{-5}$, Figure 5.8C) in the 51 communities in which both species could par-

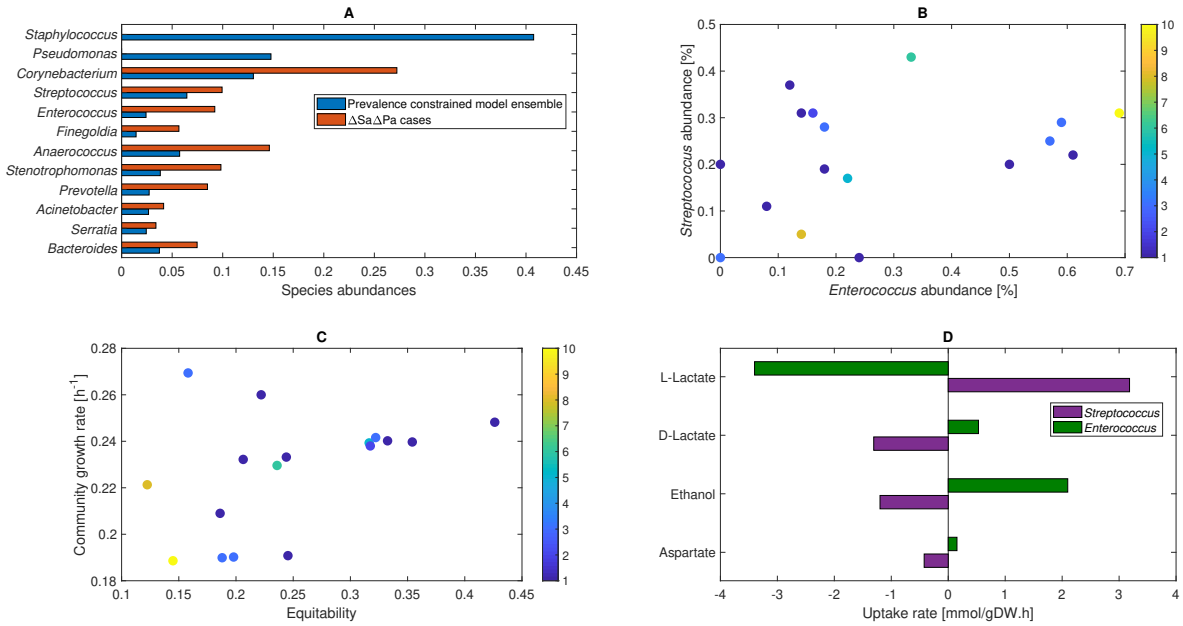

Figure 5.8: Model ensemble predictions for ΔSaΔPa simulations showing a mutualistic relationship between *Streptococcus* and *Enterococcus*. (A) Average species abundances for all 5,000 ensemble simulations and 1,264 ΔSaΔPa simulations. (B) *Streptococcus* and *Enterococcus* abundances for 51 simulated communities in which both species could participate where the colorbar indicates the number of simulations represented by each circle. The two species showed a mutualistic interaction ($r = 0.53$, $p < 10^{-6}$). (C) Community growth rates and equitability for 51 simulated communities with both species. (D) The four most significant crossfeeding relationships between the two species.

ticipate. The two species interacted through the crossfeeding of multiple metabolites (Figure 5.8D), with L-lactate consumption important for *Enterococcus* coexistence. *Streptococcus* and *Enterococcus* are known to form thick and dense biofilms on root canal dentin and glass slides [277]. Furthermore, *Enterococcus* has been shown to be more resistant to starvation in coexistence with *Streptococcus* [277], an interaction our model attributed to L-lactate crossfeeding.

5.4 Discussion

Polymicrobial infections in chronic wounds are responsible for poor clinical outcomes and cause elevated mortality rates as compared to single-species infections [252]. Colonizing species establish mutualistic relationship through multiple mechanisms including metabolite crossfeeding to promote community stability and resilience [137, 139, 278]. Robust community structures mitigate the effectiveness of antibiotic treatments and promote the evolution of antibiotic resistance through mechanisms such as horizontal gene transfer [279, 280]. The communities place an increasing bioburden on the host and play a critical role in impaired/delayed wound healing [281–283]. While recent studies based on 16S rRNA [284] and rDNA [285, 1] sequencing have revealed key bacterial taxa involved in chronic wound infections, knowledge about the interspecies mechanisms that drive community structure and function have remained elusive.

We developed a 12 species community metabolic model to identify putative interactions that drive the composition of chronic wound communities. The 12 bacterial species covered 74% of 16S rDNA pyrosequencing reads of genera from 2,963 chronic wound patients [1]. We used the limited data available from chronic wound metabolomics studies [256–258] as a starting point to define community uptake rates as required in the SteadyCom modeling framework [74]. Model tuning was used to define 81 host-derived nutrients and their uptake rates such that each species was capa-

ble of monoculture growth and predicted species abundances were in rough agreement with normalized 16S values from the original study [1]. The tuning process required the introduction of 30 metabolites to achieve monoculture growth and three putative chronic wound metabolites to enhance the growth rates of particular species: starch 1 (*Corynebacterium*), kestose (*Enterococcus*) and glycerol-3-phosphate (*Prevotella*). As discussed in our previous modeling study on cystic fibrosis communities [76], the 30 essential metabolites suggests limitations for the AGORA genome-scale metabolic models [77] with respect to biosynthetic pathways leading to biomass formation. The presence of the three growth-enhancing metabolites in chronic wound beds would need to be tested through metabolomics.

The tuned single-species models offered a wide range of predicted metabolic capabilities with respect to their growth rates and metabolite secretion patterns (Figure 2). As found in our previous modeling studies on gut [75] and cystic fibrosis [76] communities, pathogens such as *Staphylococcus*, *Pseudomonas* and *Stenotrophomonas* generally had higher growth rates than commensal species, suggesting that they are more metabolically capable of dominating the community. When compared to normalized 16S-derived abundances averaged across the 2,963 patients, the tuned community model predicted relatively high abundances for the most highly represented genera (*Staphylococcus*, *Pseudomonas*, *Corynebacterium*) but underpredicted or overpredicted abundances of the remaining genera and generated a relatively low diversity community.

We sought to improve the prediction of community composition by imposing genera prevalence data available from the original study [1] as additional *in silico* constraints. The prevalence data was used to generate an ensemble of 5,000 communities in which the participating species of each community were randomly determined. While the *in silico* prevalences averaged over the 5,000 simulations deviated slightly from the 16S-derived values (see Materials and Methods), the average species abun-

dances predicted by the prevalence-constrained model ensemble showed substantially improved agreement (Figure 3). These results demonstrate the difficulties in predicting 16S-derived abundances averaged over large numbers of patient samples with a single community model that is best thought of as simulating a single patient sample.

Because *Staphylococcus* and *Pseudomonas* are the dominant pathogens observed in most chronic wound infections [65, 263, 262, 61, 243, 261], we were interested in community behavior in the presence and absence of these two pathogens. To overcome the lack of individual patient sample data in the original study [1], the ensemble of 5,000 community simulations was partitioned into four groups: both *Staphylococcus* and *Pseudomonas* allowed to participate (SaPa, 820 cases); *Pseudomonas* not allowed to participate (SaΔPa, 2,410 cases); *Staphylococcus* not allowed to participate (ΔSaPa, 506 cases); and neither *Staphylococcus* or *Pseudomonas* allowed to participate (ΔSaΔPa, 1,264 cases). We sought to computationally identify mutualistic relationships between species for each of the four scenarios since mutualisms reduce competition for available nutrients and result in robust communities associated with prolonged infections and poor clinical outcomes [62]. These putative mutualistic interactions were viewed as future targets for experimental testing and possible therapeutic disruption to enhance treatment efficacy.

When the pathogens *Staphylococcus* and *Pseudomonas* were allowed to participate in communities, the only significant mutualistic relationship predicted was between the two pathogens themselves. These SaPa communities were characterized by pathogen dominance, low diversity and high growth rates with little variability (Figure 5), characteristics we previously attributed to resilient communities well progressed towards a fully developed disease state [75, 76]. Mutualism was supported by bi-directional crossfeeding of organic acids, amino acids and ethanol between the two species, making the identification of a single crossfeeding relationship for disruption a challenge. These predictions are supported by studies showing that the

presence of *Pseudomonas* along with *Staphylococcus* generates larger chronic wounds and delays/prevents the healing process [286, 287, 65, 288].

In the absence of *Pseudomonas*, *Staphylococcus* was predicted to form mutualistic relationships with the less abundant pathogen *Acinetobacter* and the commensal *Corynebacterium*. By spreading mutualism across two pairs of species, the SaΔPa ensemble produced slightly more diverse communities at the expense of slower and more variable growth (Figure 6). These results suggest that infections lacking *Pseudomonas* should be more easily treated, a hypothesis supported by the aforementioned studies [286, 287, 65, 288]. The *Staphylococcus–Acinetobacter* interaction was driven by lower metabolite crossfeeding rates than those predicted for *Staphylococcus* and *Pseudomonas*, another indication that *Pseudomonas*-free infections should be more easily cleared. These predictions could yield new insights into the treatment of the so-called ESKAPE pathogens (*Enterococcus faecalis*, *Staphylococcus aureus*, *Klebsiella pneumoniae*, *Acinetobacter baumannii*, *Pseudomonas aeruginosa*, *Enterobacter species*) which are the leading cause of nosocomial infections [272, 273].

When *Staphylococcus* was omitted from the simulated communities, *Pseudomonas* was predicted to have mutualistic relationships with four other species: *Serratia*, *Streptococcus*, *Acinetobacter* and *Bacteroides*. Consistent with the trends mentioned above, this increase in the number of mutualistic interactions resulted in the ΔSaPa ensemble producing more diverse communities which exhibited slower and more variable growth (Figure 6). The effect of removing *Staphylococcus* in the SaΔPa communities was greater than the effect of removing *Pseudomonas* in the SaΔPa communities, consistent with the role of *Staphylococcus* as the single dominant pathogen in chronic wound infections whose absence correlates to better clinical outcomes [289, 61]. The *Pseudomonas-Serratia* interaction was primarily driven by L-lactate and D-lactate exchange between the two species, a prediction that could be tested through *in vitro* experiments.

Of the 90 pairwise interactions possible when both *Staphylococcus* and *Pseudomonas* were removed, 22 interactions were predicted to be significantly mutualistic. The ΔSaΔPa ensemble exhibited substantially higher diversity and lower and more variable growth than the other three ensembles, consistent with earlier stage infections that lack dominant pathogens. One particularly interesting mutualistic relationship involved the commensal *Streptococcus* and ESKAPE pathogen *Enterococcus*, which has some experimental support [277]. Our model predicted that this interaction was driven largely by L-lactate consumption by *Enterococcus*, demonstrating how pathogens may take advantage of metabolic byproducts secreted by commensals to increase their abundance when more dominant pathogens are absent.

CHAPTER 6

CONCLUSIONS AND FUTURE WORK

6.1 Summary

The metabolic modeling framework (Figure 6.1) was developed to study interspecies interactions and to evaluate the impact of host environment on the interspecies interactions in the multispecies biofilms. Steady state community metabolic models were developed by identifying dominant genera from 16S patient data. These models were solved using SteadyCom method where community growth rate is maximized and the relative species abundances, cross feeding rates and byproduct secretion rates were obtained. These models can be used to identify mutualistic interactions from multispecies communities. The mutualistic interactions play important role in species pathogenesis and disease progression. The developed metabolic modeling framework is capable of mapping individual patient data for devising patient specific antibiotic treatments.

To study the heterogeneity in the biofilm system caused by concentration gradients, the spatiotemporal biofilm metabolic models were developed. These models were used to study spatial/temporal organization of the species and interspecies interactions such as crossfeeding, species inhibition and nutrient competition. The biofilm models were formulated by combining genome scale metabolic reconstructions of considered species and transport equations for species biomass and nutrient concentrations. The models were solved by using dynamic flux balance approach. This is a powerful tool as the concentration gradients in the biofilms drive the dynamics of the interspecies interactions and spatial organization.

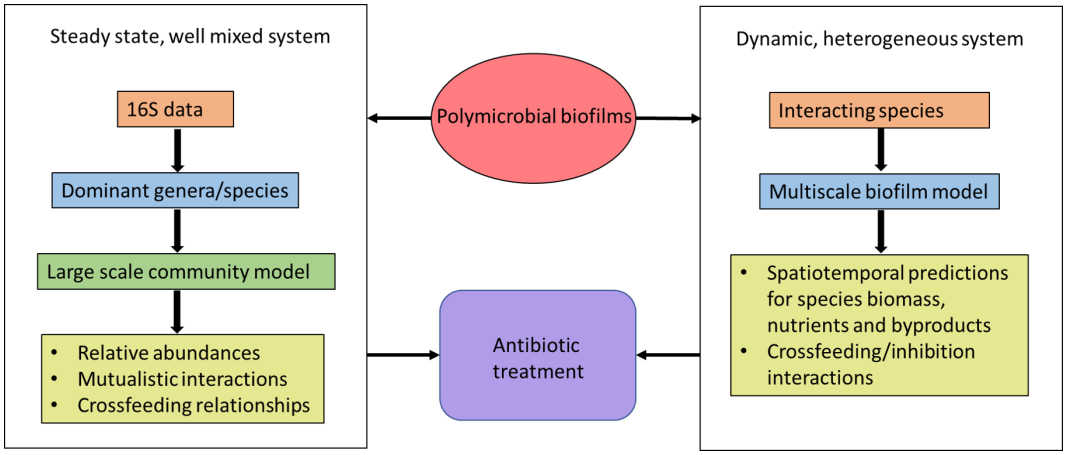

Figure 6.1: Overview of multispecies biofilm metabolic modeling.

Taken together, the steady state models use 16S patient data to predict robust mutualistic interactions which further can be studied with the help of spatiotemporal models to analyze the underlying causes of treatment failures. These insights would be helpful in designing better antibiotic treatments.

6.2 Future Work

Two species chronic wound biofilm model can be extended by developing a model bacterial consortia system comprised of three clinical chronic wound isolates: aerobic *Pseudomonas aeruginosa*, facultative anaerobe *Staphylococcus aureus* and obligate anaerobe *Clostridium perfringens* [86]. This consortium would be ideal for developing and validating the necessary computational and analytical methods for investigating the recalcitrance of chronic wound biofilms. The existing chronic wound biofilm model can be modified by adding genome scale metabolic reconstruction of a third species *Clostridium perfringens*. The model can be further extended by adding reaction-diffusion equation for supplied antibiotics. The model can be initially limited to a single antibiotic at a time. The species biomass equations can be modified to include growth inhibition and cell death terms mediated by the antibiotics. For simplicity, the model can be initially limited to a single antibiotic at a time. The species biomass

equations can be modified to include growth inhibition and cell death terms mediated by the antibiotics. The antibiotic uptake kinetics, inhibited growth rate and death rate will depend on the local antibiotic concentrations. The simulation results can be validated with experimental observations.

Multispecies community models can be developed for studying interactions between gut microbiota and *Clostridium difficile* during CDI associated dysbiosis. The relative abundance data obtained for healthy case and dysbiosis case along with mutualistic relationships within the community would be useful in understanding the CDI and develop antibiotic therapy. This community modeling framework would also be useful in identifying the metabolic differences in gut microbiota of healthy person and *C. difficile* infected patient.

The metabolic model predictions are dependent on the species uptake kinetics (v_{max} and k_m). Due to lack of species specific nutrient uptake kinetics, we have used parameters obtained from *E. coli*. The model predictions are also dependent on diffusion and mass transfer coefficients of species, metabolites and byproducts. Experiments can be performed to obtain the species specific nutrient uptake parameters. The dissolved oxygen levels and the pH gradients in the biofilm will significantly change the coexistence map of the species and hence experiments can be performed to get these profiles. Further, the computational model can be extended to account the changes in pH by fitting the profiles obtained from experiments and the predictions of species concentrations can be improved.

The spatiotemporal model can be extended to account for spatial expansion or contraction in case of biofilm development or treatment. Biofilm expansion can be assumed to be driven by the relative rates of cell growth and death. Cell growth increases the local biomass concentration and cell death leads to decrease in biomass concentration. This extension would be useful in predicting the biofilm metabolism over expanding/contracting thicknesses.

The biofilm systems are assumed to be in laminar flow and model predictions can be improved by adding an impact of shear force on the removal of biomass cells. The mass transfer occurring at air-biofilm interface can be modeled as a two phase mass transfer and the boundary conditions can be changed based on this correction. The air-biofilm mass transfer coefficients can be calculated by developing a simple computational fluid dynamic model for in vitro system of well plates. The results from computational study can be validated from the in vitro experiments.

BIBLIOGRAPHY

[1] R. D. Wolcott, J. D. Hanson, E. J. Rees, L. D. Koenig, C. D. Phillips, R. A. Wolcott, S. B. Cox, and J. S. White, Analysis of the chronic wound microbiota of 2,963 patients by 16s rdna pyrosequencing, *Wound Repair and Regeneration* **24**(1), 163–174 (2016).

[2] M. Ackermann, A functional perspective on phenotypic heterogeneity in microorganisms, *Nature Reviews Microbiology* **13**(8), 497–508 (2015).

[3] H. C. Bernstein and R. P. Carlson, Microbial consortia engineering for cellular factories: in vitro to in silico systems, *Computational and structural biotechnology journal* **3**(4), 1–8 (2012).

[4] L. Hall-Stoodley, J. W. Costerton, and P. Stoodley, Bacterial biofilms: from the natural environment to infectious diseases, *Nature reviews microbiology* **2**(2), 95–108 (2004).

[5] P. Stoodley, K. Sauer, D. Davies, and J. W. Costerton, Biofilms as complex differentiated communities, *Annual Reviews in Microbiology* **56**(1), 187–209 (2002).

[6] J. N. Anderl, M. J. Franklin, and P. S. Stewart, Role of antibiotic penetration limitation in klebsiella pneumoniae biofilm resistance to ampicillin and ciprofloxacin, *Antimicrobial agents and chemotherapy* **44**(7), 1818–1824 (2000).

[7] T. R. Zuroff, H. Bernstein, J. Lloyd-Randolfi, L. Jimenez-Taracido, P. S. Stewart, and R. P. Carlson, Robustness analysis of culturing perturbations on *Escherichia coli* colony biofilm beta-lactam and aminoglycoside antibiotic tolerance, *BMC microbiology* **10**(1), 185 (2010).

[8] A. Swidsinski, J. Weber, V. Loening-Baucke, L. P. Hale, and H. Lochs, Spatial organization and composition of the mucosal flora in patients with inflammatory bowel disease, *Journal of clinical microbiology* **43**(7), 3380–3389 (2005).

[9] R. R. Bollinger, A. S. Barbas, E. L. Bush, S. S. Lin, and W. Parker, Biofilms in the large bowel suggest an apparent function of the human vermiform appendix, *Journal of Theoretical Biology* **249**(4), 826–831 (2007).

[10] P. Tenke, B. Köves, K. Nagy, S. J. Hultgren, W. Mendling, B. Wullt, M. Grabe, F. M. Wagenlehner, M. Cek, R. Pickard, *et al.*, Update on biofilm infections in the urinary tract, *World Journal of Urology* **30**(1), 51–57 (2012).

[11] S. Macfarlane, E. Furrie, A. Kennedy, J. Cummings, and G. Macfarlane, Mucosal bacteria in ulcerative colitis, *British Journal of Nutrition* **93**(S1), S67–S72 (2005).

[12] J. W. Costerton, P. S. Stewart, and E. P. Greenberg, Bacterial biofilms: a common cause of persistent infections, *Science* **284**(5418), 1318–1322 (1999).

[13] T. J. Kinnari, The role of biofilm in chronic laryngitis and in head and neck cancer, *Current Opinion in Otolaryngology & Head and Neck Surgery* **23**(6), 448–453 (2015).

[14] T. M. Hoehler, B. M. Bebout, and D. J. Des Marais, The role of microbial mats in the production of reduced gases on the early earth, *Nature* **412**(6844), 324–327 (2001).

[15] H. Van Gemerden, Microbial mats: a joint venture, *Marine Geology* **113**(1-2), 3–25 (1993).

[16] T. R. Zuroff and W. R. Curtis, Developing symbiotic consortia for lignocellulosic biofuel production, *Applied Microbiology and Biotechnology* **93**(4), 1423–1435 (2012).

[17] S. R. Gill, M. Pop, R. T. DeBoy, P. B. Eckburg, P. J. Turnbaugh, B. S. Samuel, J. I. Gordon, D. A. Relman, C. M. Fraser-Liggett, and K. E. Nelson, Metagenomic analysis of the human distal gut microbiome, *science* **312**(5778), 1355–1359 (2006).

[18] F. Bäckhed, R. E. Ley, J. L. Sonnenburg, D. A. Peterson, and J. I. Gordon, Host-bacterial mutualism in the human intestine, *science* **307**(5717), 1915–1920 (2005).

[19] A. J. Macpherson and N. L. Harris, Interactions between commensal intestinal bacteria and the immune system, *Nature Reviews Immunology* **4**(6), 478–485 (2004).

[20] A. J. Bäumler and V. Sperandio, Interactions between the microbiota and pathogenic bacteria in the gut, *Nature* **535**(7610), 85–93 (2016).

[21] G. den Besten, K. van Eunen, A. K. Groen, K. Venema, D.-J. Reijngoud, and B. M. Bakker, The role of short-chain fatty acids in the interplay between diet, gut microbiota, and host energy metabolism, *Journal of lipid research* **54**(9), 2325–2340 (2013).

[22] S. Macfarlane, H. Steed, and G. T. Macfarlane, Intestinal bacteria and inflammatory bowel disease, *Critical reviews in clinical laboratory sciences* **46**(1), 25–54 (2009).

[23] D. J. Morrison and T. Preston, Formation of short chain fatty acids by the gut microbiota and their impact on human metabolism, *Gut Microbes* **7**(3), 189–200 (2016).

[24] M. Rajilić-Stojanović, H. Smidt, and W. M. De Vos, Diversity of the human gastrointestinal tract microbiota revisited, *Environmental microbiology* **9**(9), 2125–2136 (2007).

[25] E. Zoetendal, M. Rajilić-Stojanović, and W. De Vos, High-throughput diversity and functionality analysis of the gastrointestinal tract microbiota, *Gut* **57**(11), 1605–1615 (2008).

[26] J. Gerritsen, H. Smidt, G. T. Rijkers, and W. M. Vos, Intestinal microbiota in human health and disease: the impact of probiotics, *Genes & nutrition* **6**(3), 209 (2011).

[27] V. B. Young and T. M. Schmidt, Antibiotic-associated diarrhea accompanied by large-scale alterations in the composition of the fecal microbiota, *Journal of clinical microbiology* **42**(3), 1203–1206 (2004).

[28] K. Brown, D. DeCoffe, E. Molcan, and D. L. Gibson, Diet-induced dysbiosis of the intestinal microbiota and the effects on immunity and disease, *Nutrients* **4**(8), 1095–1119 (2012).

[29] M. Anitha, F. Reichardt, S. Tabatabavakili, B. G. Nezami, B. Chassaing, S. Mwangi, M. Vijay-Kumar, A. Gewirtz, and S. Srinivasan, Intestinal dysbiosis contributes to the delayed gastrointestinal transit in high-fat diet fed mice, *CMGH Cellular and Molecular Gastroenterology and Hepatology* **2**(3), 328–339 (2016).

[30] M. T. Alou, J.-C. Lagier, and D. Raoult, Diet influence on the gut microbiota and dysbiosis related to nutritional disorders, *Human Microbiome Journal* **1**, 3–11 (2016).

[31] A. Agus, J. Denizot, J. Thévenot, M. Martinez-Medina, S. Massier, P. Sauvanet, A. Bernalier-Donadille, S. Denis, P. Hofman, R. Bonnet, *et al.*, Western diet induces a shift in microbiota composition enhancing susceptibility to adherent-invasive *E. coli* infection and intestinal inflammation., *Scientific reports* **6** (2016).

[32] C. M. Theriot, A. A. Bowman, and V. B. Young, Antibiotic-induced alterations of the gut microbiota alter secondary bile acid production and allow for *Clostridium difficile* spore germination and outgrowth in the large intestine, *MSphere* **1**(1), e00045–15 (2016).

[33] S. E. Winter, M. G. Winter, M. N. Xavier, P. Thiennimitr, V. Poon, A. M. Keestra, R. C. Laughlin, G. Gomez, J. Wu, S. D. Lawhon, *et al.*, Host-derived nitrate boosts growth of *E. coli* in the inflamed gut, *science* **339**(6120), 708–711 (2013).

[34] D. N. Frank, A. L. S. Amand, R. A. Feldman, E. C. Boedeker, N. Harpaz, and N. R. Pace, Molecular-phylogenetic characterization of microbial community imbalances in human inflammatory bowel diseases, *Proceedings of the National Academy of Sciences* **104**(34), 13780–13785 (2007).

[35] R. E. Ley, P. J. Turnbaugh, S. Klein, and J. I. Gordon, Microbial ecology: human gut microbes associated with obesity, *Nature* **444**(7122), 1022–1023 (2006).

[36] S. Carding, K. Verbeke, D. T. Vipond, B. M. Corfe, and L. J. Owen, Dysbiosis of the gut microbiota in disease, *Microbial ecology in health and disease* **26**(1), 26191 (2015).

[37] C. M. Surawicz, L. J. Brandt, D. G. Binion, A. N. Ananthakrishnan, S. R. Curry, P. H. Gilligan, L. V. McFarland, M. Mellow, and B. S. Zuckerbraun, Guidelines for diagnosis, treatment, and prevention of clostridium difficile infections, *The American journal of gastroenterology* **108**(4), 478 (2013).

[38] J. K. Shim, S. Johnson, M. H. Samore, D. Z. Bliss, and D. N. Gerding, Primary symptomless colonisation by *Clostridium difficile* and decreased risk of subsequent diarrhoea, *The Lancet* **351**(9103), 633–636 (1998).

[39] L. Kyne, M. Warny, A. Qamar, and C. P. Kelly, Asymptomatic carriage of *Clostridium difficile* and serum levels of igg antibody against toxin a, *New England Journal of Medicine* **342**(6), 390–397 (2000).

[40] F. Barbut and J.-C. Petit, Epidemiology of *Clostridium difficile*-associated infections, *Clinical Microbiology and Infection* **7**(8), 405–410 (2001).

[41] H. Kato, H. Kita, T. Karasawa, T. Maegawa, Y. Koino, H. Takakuwa, T. Saikai, K. Kobayashi, T. Yamagishi, and S. Nakamura, Colonisation and transmission of *Clostridium difficile* in healthy individuals examined by pcr ribotyping and pulsed-field gel electrophoresis, *Journal of medical microbiology* **50**(8), 720–727 (2001).

[42] E. Ozaki, H. Kato, H. Kita, T. Karasawa, T. Maegawa, Y. Koino, K. Matsumoto, T. Takada, K. Nomoto, R. Tanaka, *et al.*, *Clostridium difficile* colonization in healthy adults: transient colonization and correlation with enterococcal colonization, *Journal of medical microbiology* **53**(2), 167–172 (2004).

[43] S. M. Poutanen and A. E. Simor, *Clostridium difficile*-associated diarrhea in adults, *Canadian Medical Association Journal* **171**(1), 51–58 (2004).

[44] L. Furuya-Kanamori, J. Marquess, L. Yakob, T. V. Riley, D. L. Paterson, N. F. Foster, C. A. Huber, and A. C. Clements, Asymptomatic *Clostridium difficile* colonization: epidemiology and clinical implications, *BMC infectious diseases* **15**(1), 516 (2015).

[45] J. Y. Chang, D. A. Antonopoulos, A. Kalra, A. Tonelli, W. T. Khalife, T. M. Schmidt, and V. B. Young, Decreased diversity of the fecal microbiome in recurrent *Clostridium difficile*—associated diarrhea, *The Journal of infectious diseases* **197**(3), 435–438 (2008).

[46] J. G. Bartlett, *Clostridium difficile*: history of its role as an enteric pathogen and the current state of knowledge about the organism, *Clinical Infectious Diseases* **18**(Supplement_4), S265–S272 (1994).

[47] A. E. Pérez-Cobas, A. Moya, M. J. Gosalbes, and A. Latorre, Colonization resistance of the gut microbiota against *Clostridium difficile*, *Antibiotics* **4**(3), 337–357 (2015).

[48] C. Pothoulakis, Pathogenesis of *Clostridium difficile*-associated diarrhoea., *European journal of gastroenterology & hepatology* **8**(11), 1041–1047 (1996).

[49] C. M. Theriot and V. B. Young, Interactions between the gastrointestinal microbiome and *Clostridium difficile*, *Annual review of microbiology* **69**, 445–461 (2015).

[50] E. Mylonakis, E. T. Ryan, and S. B. Calderwood, Clostridium difficile–associated diarrhea: a review, *Archives of Internal Medicine* **161**(4), 525–533 (2001).

[51] A. M. Jarrad, T. Karoli, M. A. Blaskovich, D. Lyras, and M. A. Cooper, *Clostridium difficile* drug pipeline: challenges in discovery and development of new agents, *Journal of medicinal chemistry* **58**(13), 5164–5185 (2015).

[52] F. C. Lessa, Y. Mu, W. M. Bamberg, Z. G. Beldavs, G. K. Dumyati, J. R. Dunn, M. M. Farley, S. M. Holzbauer, J. I. Meek, E. C. Phipps, *et al.*, Burden of *Clostridium difficile* infection in the united states, *New England Journal of Medicine* **372**(9), 825–834 (2015).

[53] E. R. Dubberke and M. A. Olsen, Burden of *Clostridium difficile* on the healthcare system, *Clinical infectious diseases* **55**(suppl_2), S88–S92 (2012).

[54] S. E. Dowd, Y. Sun, P. R. Secor, D. D. Rhoads, B. M. Wolcott, G. A. James, and R. D. Wolcott, Survey of bacterial diversity in chronic wounds using pyrosequencing, dgge, and full ribosome shotgun sequencing, *BMC microbiology* **8**(1), 43 (2008a).

[55] S. E. Dowd, R. D. Wolcott, Y. Sun, T. McKeehan, E. Smith, and D. Rhoads, Polymicrobial nature of chronic diabetic foot ulcer biofilm infections determined using bacterial tag encoded flx amplicon pyrosequencing (btefap), *PloS one* **3**(10), e3326 (2008b).

[56] G. A. James, E. Swogger, R. Wolcott, E. deLancey Pulcini, P. Secor, J. Sestrich, J. W. Costerton, and P. S. Stewart, Biofilms in chronic wounds, *Wound Repair and regeneration* **16**(1), 37–44 (2008).

[57] B. M. Peters, M. A. Jabra-Rizk, A. Graeme, J. W. Costerton, and M. E. Shirtliff, Polymicrobial interactions: impact on pathogenesis and human disease, *Clinical microbiology reviews* **25**(1), 193–213 (2012).

[58] T. R. Thomsen, M. S. Aasholm, V. B. Rudkjøbing, A. M. Saunders, T. Bjarnsholt, M. Givskov, K. Kirketerp-Møller, and P. H. Nielsen, The bacteriology of chronic venous leg ulcer examined by culture-independent molecular methods, *Wound Repair and Regeneration* **18**(1), 38–49 (2010).

[59] D. G. Metcalf and P. G. Bowler, Biofilm delays wound healing: A review of the evidence, *Burns & Trauma* **1**(1), 5 (2015).

[60] A. T. Nguyen and A. G. Oglesby-Sherrouse, Interactions between pseudomonas aeruginosa and staphylococcus aureus during co-cultivations and polymicrobial infections, *Applied microbiology and biotechnology* **100**(14), 6141–6148 (2016).

[61] I. Pastar, A. G. Nusbaum, J. Gil, S. B. Patel, J. Chen, J. Valdes, O. Stojadinovic, L. R. Plano, M. Tomic-Canic, and S. C. Davis, Interactions of methicillin resistant *Staphylococcus aureus* usa300 and *Pseudomonas aeruginosa* in polymicrobial wound infection, *PloS one* **8**(2), e56846 (2013).

[62] P. Bowler, B. Duerden, and D. G. Armstrong, Wound microbiology and associated approaches to wound management, *Clinical microbiology reviews* **14**(2), 244–269 (2001).

[63] F. Gottrup, A specialized wound-healing center concept: importance of a multidisciplinary department structure and surgical treatment facilities in the treatment of chronic wounds, *The American Journal of Surgery* **187**(5), S38–S43 (2004).

[64] C. K. Sen, G. M. Gordillo, S. Roy, R. Kirsner, L. Lambert, T. K. Hunt, F. Gottrup, G. C. Gurtner, and M. T. Longaker, Human skin wounds: a major and snowballing threat to public health and the economy, *Wound repair and regeneration* **17**(6), 763–771 (2009).

[65] K. Gjødsbøl, J. J. Christensen, T. Karlsmark, B. Jørgensen, B. M. Klein, and K. A. Krogfelt, Multiple bacterial species reside in chronic wounds: a longitudinal study, *International wound journal* **3**(3), 225–231 (2006).

[66] R. Wolcott, V. Gontcharova, Y. Sun, A. Zischakau, and S. Dowd, Bacterial diversity in surgical site infections: not just aerobic cocci any more, *Journal of wound care* **18**(8), 317–323 (2009).

[67] S. Pulimood, L. Ganesan, G. Alangaden, and P. Chandrasekar, Polymicrobial candidemia, *Diagnostic microbiology and infectious disease* **44**(4), 353–357 (2002).

[68] A. K. Seth, M. R. Geringer, S. J. Hong, K. P. Leung, R. D. Galiano, and T. A. Mustoe, Comparative analysis of single-species and polybacterial wound biofilms using a quantitative, in vivo, rabbit ear model, *PLoS One* **7**(8), e42897 (2012).

[69] T. Tolker-Nielsen and S. Molin, Spatial organization of microbial biofilm communities, *Microbial ecology* **40**(2), 75–84 (2000).

[70] O. Perez-Garcia, G. Lear, and N. Singhal, Metabolic network modeling of microbial interactions in natural and engineered environmental systems, *Frontiers in microbiology* **7**, 673 (2016).

[71] M. Hanemaaijer, W. F. Röling, B. G. Olivier, R. A. Khandelwal, B. Teusink, and F. J. Bruggeman, Systems modeling approaches for microbial community studies: from metagenomics to inference of the community structure, *Frontiers in microbiology* **6**, 213 (2015).

[72] S. Freilich, R. Zarecki, O. Eilam, E. S. Segal, C. S. Henry, M. Kupiec, U. Gophna, R. Sharan, and E. Ruppin, Competitive and cooperative metabolic interactions in bacterial communities, *Nature communications* **2**, 589 (2011).

[73] S. Shoaie, F. Karlsson, A. Mardinoglu, I. Nookaew, S. Bordel, and J. Nielsen, Understanding the interactions between bacteria in the human gut through metabolic modeling, *Scientific reports* **3**, 2532 (2013).

[74] S. H. J. Chan, M. N. Simons, and C. D. Maranas, Steadycom: Predicting microbial abundances while ensuring community stability, *PLoS computational biology* **13**(5), e1005539 (2017).

[75] M. A. Henson and P. Phalak, Suboptimal community growth mediated through metabolite crossfeeding promotes species diversity in the gut microbiota, *PLoS computational biology* **14**(10), e1006558 (2018).

[76] M. A. Henson, G. Orazi, P. Phalak, and G. O'Toole, Metabolic modeling of cystic fibrosis airway communities predicts mechanisms of pathogen dominance, *bioRxiv* p. 520619 (2019).

[77] S. Magnúsdóttir, A. Heinken, L. Kutt, D. A. Ravcheev, E. Bauer, A. Noronha, K. Greenhalgh, C. Jäger, J. Baginska, P. Wilmes, *et al.*, Generation of genome-scale metabolic reconstructions for 773 members of the human gut microbiota, *Nature biotechnology* **35**(1), 81 (2017).

[78] E. K. Costello, C. L. Lauber, M. Hamady, N. Fierer, J. I. Gordon, and R. Knight, Bacterial community variation in human body habitats across space and time, *Science* **326**(5960), 1694–1697 (2009).

[79] K. Faust and J. Raes, Microbial interactions: from networks to models, *Nature Reviews Microbiology* **10**(8), 538–550 (2012).

[80] F. J. Hol, P. Galajda, R. G. Woolthuis, C. Dekker, and J. E. Keymer, The idiosyncrasy of spatial structure in bacterial competition, *BMC research notes* **8**(1), 245 (2015).

[81] Á. T. Kovács, Impact of spatial distribution on the development of mutualism in microbes, *Frontiers in microbiology* **5**, 649 (2014).

[82] P. S. Stewart and M. J. Franklin, Physiological heterogeneity in biofilms, *Nature Reviews Microbiology* **6**(3), 199–210 (2008).

[83] M. Burmølle, D. Ren, T. Bjarnsholt, and S. J. Sørensen, Interactions in multi-species biofilms: do they actually matter?, *Trends in microbiology* **22**(2), 84–91 (2014).

[84] V. Mazumdar, S. Amar, and D. Segrè, Metabolic proximity in the order of colonization of a microbial community, *PloS one* **8**(10), e77617 (2013).

[85] P. S. Stewart, A review of experimental measurements of effective diffusive permeabilities and effective diffusion coefficients in biofilms, *Biotechnology and bioengineering* **59**(3), 261–272 (1998).

[86] J. Woods, L. Boegli, K. R. Kirker, A. M. Agostinho, A. M. Durch, E. deLancey Pulcini, P. S. Stewart, and G. A. James, Development and application of a polymicrobial, in vitro, wound biofilm model, *Journal of applied microbiology* **112**(5), 998–1006 (2012).

[87] Y. Fang, T. D. Scheibe, R. Mahadevan, S. Garg, P. E. Long, and D. R. Lovley, Direct coupling of a genome-scale microbial in silico model and a groundwater reactive transport model, *Journal of Contaminant Hydrology* **122**(1), 96–103 (2011).

[88] N. Jayasinghe, A. Franks, K. P. Nevin, and R. Mahadevan, Metabolic modeling of spatial heterogeneity of biofilms in microbial fuel cells reveals substrate limitations in electrical current generation, *Biotechnology Journal* **9**(10), 1350–1361 (2014).

[89] T. D. Scheibe, R. Mahadevan, Y. Fang, S. Garg, P. E. Long, and D. R. Lovley, Coupling a genome-scale metabolic model with a reactive transport model to describe in situ uranium bioremediation, *Microbial Biotechnology* **2**(2), 274–286 (2009).

[90] J. A. Cole, L. Kohler, J. Hedhli, and Z. Luthey-Schulten, Spatially-resolved metabolic cooperativity within dense bacterial colonies, *BMC Systems Biology* **9**(1), 1 (2015).

[91] W. R. Harcombe, W. J. Riehl, I. Dukovski, B. R. Granger, A. Betts, A. H. Lang, G. Bonilla, A. Kar, N. Leiby, P. Mehta, *et al.*, Metabolic resource allocation in individual microbes determines ecosystem interactions and spatial dynamics, *Cell Reports* **7**(4), 1104–1115 (2014).

[92] J. Chen, J. A. Gomez, K. Höffner, P. I. Barton, and M. A. Henson, Metabolic modeling of synthesis gas fermentation in bubble column reactors, *Biotechnology for Biofuels* **8**(1), 1 (2015).

[93] J. Chen, J. A. Gomez, K. Höffner, P. Phalak, P. I. Barton, and M. A. Henson, Spatiotemporal modeling of microbial metabolism, *BMC systems biology* **10**(1), 21 (2016).

[94] M. W. Konstan, K. A. Hilliard, T. M. Norvell, and M. Berger, Bronchoalveolar lavage findings in cystic fibrosis patients with stable, clinically mild lung disease suggest ongoing infection and inflammation., *American Journal of Respiratory and Critical Care <edicine* **150**(2), 448–454 (1994).

[95] J. P. Folsom, L. Richards, B. Pitts, F. Roe, G. D. Ehrlich, A. Parker, A. Mazurie, and P. S. Stewart, Physiology of *Pseudomonas aeruginosa* in biofilms as revealed by transcriptome analysis, *BMC Microbiology* **10**(1), 1 (2010).

[96] G. Borriello, E. Werner, F. Roe, A. M. Kim, G. D. Ehrlich, and P. S. Stewart, Oxygen limitation contributes to antibiotic tolerance of *Pseudomonas aeruginosa* in biofilms, *Antimicrobial Agents and Chemotherapy* **48**(7), 2659–2664 (2004).

[97] G. W. Lau, D. J. Hassett, H. Ran, and F. Kong, The role of pyocyanin in *Pseudomonas aeruginosa* infection, *Trends in Molecular Medicine* **10**(12), 599–606 (2004).

[98] S. Bakkal, S. M. Robinson, C. L. Ordonez, D. A. Waltz, and M. A. Riley, Role of bacteriocins in mediating interactions of bacterial isolates taken from cystic fibrosis patients, *Microbiology* **156**(7), 2058–2067 (2010).

[99] C. Gao, C. Hu, Z. Zheng, C. Ma, T. Jiang, P. Dou, W. Zhang, B. Che, Y. Wang, M. Lv, *et al.*, Lactate utilization is regulated by the fadr-type regulator lldr in *Pseudomonas aeruginosa*, *Journal of Bacteriology* **194**(10), 2687–2692 (2012).

[100] M. Shitashiro, J. Kato, T. Fukumura, A. Kuroda, T. Ikeda, N. Takiguchi, and H. Ohtake, Evaluation of bacterial aerotaxis for its potential use in detecting the toxicity of chemicals to microorganisms, *Journal of Biotechnology* **101**(1), 11–18 (2003).

[101] A. Berger, K. Dohnt, P. Tielen, D. Jahn, J. Becker, and C. Wittmann, Robustness and plasticity of metabolic pathway flux among uropathogenic isolates of *Pseudomonas aeruginosa*, *PloS One* **9**(4), e88368 (2014).

[102] M. A. Oberhardt, J. Puchałka, K. E. Fryer, V. A. M. Dos Santos, and J. A. Papin, Genome-scale metabolic network analysis of the opportunistic pathogen *Pseudomonas aeruginosa* pao1, *Journal of Bacteriology* **190**(8), 2790–2803 (2008).

[103] M. Eschbach, K. Schreiber, K. Trunk, J. Buer, D. Jahn, and M. Schobert, Long-term anaerobic survival of the opportunistic pathogen *Pseudomonas aeruginosa* via pyruvate fermentation, *Journal of Bacteriology* **186**(14), 4596–4604 (2004).

[104] M. Heinemann, A. Kümmel, R. Ruinatscha, and S. Panke, In silico genome-scale reconstruction and validation of the *Staphylococcus aureus* metabolic network, *Biotechnology and Bioengineering* **92**(7), 850–864 (2005).

[105] F. Collins and J. Lascelles, The effect of growth conditions on oxidative and dehydrogenase activity in *Staphylococcus aureus*, *Microbiology* **29**(3), 531–535 (1962).

[106] R. Seidl, W. Rammer, R. M. Scheller, and T. A. Spies, An individual-based process model to simulate landscape-scale forest ecosystem dynamics, *Ecological Modelling* **231**, 87–100 (2012).

[107] K. Strasters and K. Winkler, Carbohydrate metabolism of *Staphylococcus aureus*, *Microbiology* **33**(2), 213–229 (1963).

[108] J.-L. Sun, S.-K. Zhang, J.-Y. Chen, and B.-Z. Han, Metabolic profiling of *Staphylococcus aureus* cultivated under aerobic and anaerobic conditions with 1h nmr-based nontargeted analysis, *Canadian Journal of Microbiology* **58**(6), 709–718 (2012).

[109] T. Theodore and A. Schade, Carbohydrate metabolism of iron-rich and iron-poor *Staphylococcus aureus*, *Microbiology* **40**(3), 385–395 (1965).

[110] E. F. Keller and L. A. Segel, Model for chemotaxis, *Journal of Theoretical Biology* **30**(2), 225–234 (1971).

[111] Z. A. Machan, G. W. Taylor, T. L. Pitt, P. J. Cole, and R. Wilson, 2-heptyl-4-hydroxyquinoline n-oxide, an antistaphylococcal agent produced by *Pseudomonas aeruginosa*, *Journal of Antimicrobial Chemotherapy* **30**(5), 615–623 (1992).

[112] H. Beyenal, A. Tanyolac, and Z. Lewandowski, Measurement of local effective diffusivity in heterogeneous biofilms, *Water Science and Technology* **38**(8-9), 171–178 (1998).

[113] R. Mahadevan, J. S. Edwards, and F. J. Doyle, Dynamic flux balance analysis of diauxic growth in *Escherichia coli*, *Biophysical Journal* **83**(3), 1331–1340 (2002).

[114] A. L. Meadows, R. Karnik, H. Lam, S. Forestell, and B. Snedecor, Application of dynamic flux balance analysis to an industrial *Escherichia coli* fermentation, *Metabolic engineering* **12**(2), 150–160 (2010).

[115] R. Carlson and F. Srienc, Fundamental *Escherichia coli* biochemical pathways for biomass and energy production: identification of reactions, *Biotechnology and bioengineering* **85**(1), 1–19 (2004).

[116] M. El-Fouly, A. Sharaf, A. Shahin, H. A. El-Bialy, and A. Omara, Biosynthesis of pyocyanin pigment by *Pseudomonas aeruginosa*, *Journal of Radiation Research and Applied Sciences* **8**(1), 36–48 (2015).

[117] M. Beaume, T. Köhler, T. Fontana, M. Tognon, A. Renzoni, and C. van Delden, Metabolic pathways of *Pseudomonas aeruginosa* involved in competition with respiratory bacterial pathogens, *Frontiers in Microbiology* **6**, 321 (2015).

[118] S. DeLeon, A. Clinton, H. Fowler, J. Everett, A. R. Horswill, and K. P. Rumbaugh, Synergistic interactions of pseudomonas aeruginosa and staphylococcus aureus in an in vitro wound model, *Infection and immunity* **82**(11), 4718–4728 (2014).

[119] T. Markussen, R. L. Marvig, M. Gómez-Lozano, K. Aanæs, A. E. Burleigh, N. Høiby, H. K. Johansen, S. Molin, and L. Jelsbak, Environmental heterogeneity drives within-host diversification and evolution of *Pseudomonas aeruginosa*, *MBio* **5**(5), e01592–14 (2014).

[120] N. J. Trengove, S. R. Langton, and M. C. Stacey, Biochemical analysis of wound fluid from nonhealing and healing chronic leg ulcers, *Wound Repair and Regeneration* **4**(2), 234–239 (1996).

[121] M. B. Biggs and J. A. Papin, Novel multiscale modeling tool applied to *Pseudomonas aeruginosa* biofilm formation, *PloS One* **8**(10), e78011 (2013).

[122] P. S. Stewart, Diffusion in biofilms, *Journal of bacteriology* **185**(5), 1485–1491 (2003).

[123] C. Wilke and P. Chang, Correlation of diffusion coefficients in dilute solutions, *AIChE Journal* **1**(2), 264–270 (1955).

[124] L. Yang, Y. Liu, T. Markussen, N. Høiby, T. Tolker-Nielsen, and S. Molin, Pattern differentiation in co-culture biofilms formed by *Staphylococcus aureus* and *Pseudomonas aeruginosa*, *FEMS Immunology & Medical Microbiology* **62**(3), 339–347 (2011).

[125] M. A. Henson, Genome-scale modelling of microbial metabolism with temporal and spatial resolution, *Biochemical Society Transactions* **43**(6), 1164–1171 (2015).

[126] J. A. Gomez, K. Hoffner, and P. I. Barton, DFBAlab: a fast and reliable MATLAB code for dynamic flux balance analysis, *BMC bioinformatics* **15** (2014).

[127] K. Höffner, S. Harwood, and P. Barton, A reliable simulator for dynamic flux balance analysis, *Biotechnology and Bioengineering* **110**(3), 792–802 (2013).

[128] E. Werner, F. Roe, A. Bugnicourt, M. J. Franklin, A. Heydorn, S. Molin, B. Pitts, and P. S. Stewart, Stratified growth in *Pseudomonas aeruginosa* biofilms, *Applied and Environmental Microbiology* **70**(10), 6188–6196 (2004).

[129] G. Schultz, P. Phillips, Q. Yang, and P. Stewart, Biofilm maturity studies indicate sharp debridement opens a time-dependent therapeutic window, *J Wound Care* **19**(8), 320 (2010).

[130] G. A. James, A. Ge Zhao, M. Usui, R. A. Underwood, H. Nguyen, H. Beyenal, E. deLancey Pulcini, A. Agostinho Hunt, H. C. Bernstein, P. Fleckman, *et al.*, Microsensor and transcriptomic signatures of oxygen depletion in biofilms associated with chronic wounds, *Wound Repair and Regeneration* (2016).

[131] B. Aydin, R. P. Carlson, and L. Hanley, Identification and imaging of peptides and proteins on enterococcus faecalis biofilms by matrix assisted laser desorption ionization mass spectrometry, *Analyst* **137**(21), 5018–5025 (2012).

[132] C. Bhardwaj, J. F. Moore, Y. Cui, G. L. Gasper, H. C. Bernstein, R. P. Carlson, and L. Hanley, Laser desorption vuv postionization ms imaging of a cocultured biofilm, *Analytical and Bioanalytical Chemistry* **405**(22), 6969–6977 (2013).

[133] J. Oetjen, K. Veselkov, J. Watrous, J. S. McKenzie, M. Becker, L. Hauberg-Lotte, J. H. Kobarg, N. Strittmatter, A. K. Mróz, F. Hoffmann, *et al.*, Benchmark datasets for 3d maldi-and desi-imaging mass spectrometry, *GigaScience* **4**(1), 1 (2015).

[134] N. Crosetto, M. Bienko, and A. van Oudenaarden, Spatially resolved transcriptomics and beyond, *Nature Reviews Genetics* **16**(1), 57–66 (2015).

[135] A. C. Pérez-Osorio, K. S. Williamson, and M. J. Franklin, Heterogeneous rpos and rhlr mrna levels and 16s rrna/rdna (rrna gene) ratios within *Pseudomonas aeruginosa* biofilms, sampled by laser capture microdissection, *Journal of Bacteriology* **192**(12), 2991–3000 (2010).

[136] R. Almstrand, H. Daims, F. Persson, F. Sörensson, and M. Hermansson, New methods for analysis of spatial distribution and coaggregation of microbial populations in complex biofilms, *Applied and Environmental Microbiology* **79**(19), 5978–5987 (2013).

[137] S. A. West, A. S. Griffin, A. Gardner, and S. P. Diggle, Social evolution theory for microorganisms, *Nature reviews microbiology* **4**(8), 597 (2006).

[138] W. Harcombe, Novel cooperation experimentally evolved between species, *Evolution* **64**(7), 2166–2172 (2010).

[139] M. M. Ramsey, K. P. Rumbaugh, and M. Whiteley, Metabolite cross-feeding enhances virulence in a model polymicrobial infection, *PLoS pathogens* **7**(3), e1002012 (2011).

[140] S. Estrela, C. H. Trisos, and S. P. Brown, From metabolism to ecology: cross-feeding interactions shape the balance between polymicrobial conflict and mutualism, *The American Naturalist* **180**(5), 566 (2012).

[141] P. Phalak, J. Chen, R. P. Carlson, and M. A. Henson, Metabolic modeling of a chronic wound biofilm consortium predicts spatial partitioning of bacterial species, *BMC systems biology* **10**(1), 90 (2016).

[142] L. M. Filkins, J. A. Graber, D. G. Olson, E. L. Dolben, L. R. Lynd, S. Bhuju, and G. A. O'Toole, Coculture of *Staphylococcus aureus* with *Pseudomonas aeruginosa* drives *S. aureus* towards fermentative metabolism and reduced viability in a cystic fibrosis model, *Journal of Bacteriology* **197**(14), 2252–2264 (2015).

[143] K. L. Palmer, L. M. Aye, and M. Whiteley, Nutritional cues control *Pseudomonas aeruginosa* multicellular behavior in cystic fibrosis sputum, *Journal of Bacteriology* **189**(22), 8079–8087 (2007).

[144] L. E. Dietrich, A. Price-Whelan, A. Petersen, M. Whiteley, and D. K. Newman, The phenazine pyocyanin is a terminal signalling factor in the quorum sensing network of *Pseudomonas aeruginosa*, *Molecular Microbiology* **61**(5), 1308–1321 (2006).

[145] Z. Qin, L. Yang, D. Qu, S. Molin, and T. Tolker-Nielsen, *Pseudomonas aeruginosa* extracellular products inhibit staphylococcal growth, and disrupt established biofilms produced by staphylococcus epidermidis, *Microbiology* **155**(7), 2148–2156 (2009).

[146] L. R. Hoffman, E. Déziel, D. A. D'Argenio, F. Lépine, J. Emerson, S. McNamara, R. L. Gibson, B. W. Ramsey, and S. I. Miller, Selection for *Staphylococcus aureus* small-colony variants due to growth in the presence of *Pseudomonas aeruginosa*, *Proceedings of the National Academy of Sciences* **103**(52), 19890–19895 (2006).

[147] J. C. Conrad, M. L. Gibiansky, F. Jin, V. D. Gordon, D. A. Motto, M. A. Mathewson, W. G. Stopka, D. C. Zelasko, J. D. Shrout, and G. C. Wong, Flagella and pili-mediated near-surface single-cell motility mechanisms in *P. aeruginosa*, *Biophysical Journal* **100**(7), 1608–1616 (2011).

[148] B.-P. AC, In the staphylococci, *ed Cohen, J O* **Ch.1**(0), 1–20 (1972).

[149] T. Dalton, S. E. Dowd, R. D. Wolcott, Y. Sun, C. Watters, J. A. Griswold, and K. P. Rumbaugh, An in vivo polymicrobial biofilm wound infection model to study interspecies interactions, *PloS one* **6**(11), e27317 (2011).

[150] L. Gatto, L. M. Breckels, T. Burger, D. J. Nightingale, A. J. Groen, C. Campbell, C. M. Mulvey, A. Christoforou, M. Ferro, and K. S. Lilley, A foundation for reliable spatial proteomics data analysis, *Molecular & Cellular Proteomics* pp. mcp–M113 (2014).

[151] A. Cox, E. L. Shock, and J. R. Havig, The transition to microbial photosynthesis in hot spring ecosystems, *Chemical Geology* **280**(3-4), 344–351 (2011).

[152] N. Stambler and Z. Dubinsky, Marine phototrophs in the twilight zone, in *Algae and cyanobacteria in extreme environments* (Springer, 2007), pp. 79–97.

[153] K. Song, X. Tan, Y. Liang, and X. Lu, The potential of synechococcus elongatus utex 2973 for sugar feedstock production, *Applied microbiology and biotechnology* **100**(18), 7865–7875 (2016).

[154] J. K. Cole, J. R. Hutchison, R. S. Renslow, Y.-M. Kim, W. B. Chrisler, H. E. Engelmann, A. C. Dohnalkova, D. Hu, T. O. Metz, J. K. Fredrickson, *et al.*, Phototrophic biofilm assembly in microbial-mat-derived unicyanobacterial consortia: model systems for the study of autotroph-heterotroph interactions, *Frontiers in microbiology* **5**, 109 (2014).

[155] S. R. Lindemann, J. M. Mobberley, J. K. Cole, L. Markillie, R. C. Taylor, E. Huang, W. B. Chrisler, H. Wiley, M. S. Lipton, W. C. Nelson, *et al.*, Predicting species-resolved macronutrient acquisition during succession in a model phototrophic biofilm using an integrated 'omics approach, *Frontiers in microbiology* **8**, 1020 (2017).

[156] A. A. Shastri and J. A. Morgan, Flux balance analysis of photoautotrophic metabolism, *Biotechnology progress* **21**(6), 1617–1626 (2005).

[157] J. Triana, A. Montagud, M. Siurana, A. Urchueguía, D. Gamermann, J. Torres, J. Tena, P. de Córdoba, J. Urchueguía, *et al.*, Generation and evaluation of a genome-scale metabolic network model of synechococcus elongatus pcc7942, *Metabolites* **4**(3), 680–698 (2014).

[158] S. R. Lindemann, J. J. Moran, J. C. Stegen, R. S. Renslow, J. R. Hutchison, J. K. Cole, A. C. Dohnalkova, J. Tremblay, K. Singh, S. A. Malfatti, *et al.*, The epsomitic phototrophic microbial mat of hot lake, washington: community structural responses to seasonal cycling, *Frontiers in microbiology* **4**, 323 (2013).

[159] H. C. Bernstein, M. Kesaano, K. Moll, T. Smith, R. Gerlach, R. P. Carlson, C. D. Miller, B. M. Peyton, K. E. Cooksey, R. D. Gardner, *et al.*, Direct measurement and characterization of active photosynthesis zones inside wastewater remediating and biofuel producing microalgal biofilms, *Bioresource technology* **156**, 206–215 (2014).

[160] R. N. Glud, N. B. Ramsing, and N. P. Revsbech, Photosynthesis and photosynthesis-coupled respiration in natural biofilms quantified with oxygen microsensors 1, *Journal of Phycology* **28**(1), 51–60 (1992).

[161] M. Kühl, R. N. Glud, H. Ploug, and N. B. Ramsing, Microenvironmental control of photosynthesis and photosynthesis-coupled respiration in an epilithic cyanobacterial biofilm 1, *Journal of Phycology* **32**(5), 799–812 (1996).

[162] H. Bolhuis, M. S. Cretoiu, and L. J. Stal, Molecular ecology of microbial mats, *FEMS Microbiology Ecology* **90**(2), 335–350 (2014).

[163] S. G. Hays, L. L. Yan, P. A. Silver, and D. C. Ducat, Synthetic photosynthetic consortia define interactions leading to robustness and photoproduction, *Journal of biological engineering* **11**(1), 4 (2017).

[164] J. T. Kirk, Effects of suspensoids (turbidity) on penetration of solar radiation in aquatic ecosystems, *Hydrobiologia* **125**(1), 195–208 (1985).

[165] S. Ohkubo and H. Miyashita, A niche for cyanobacteria producing chlorophyll f within a microbial mat, *The ISME journal* **11**(10), 2368 (2017).

[166] M. Hagemann, Molecular biology of cyanobacterial salt acclimation, *FEMS microbiology reviews* **35**(1), 87–123 (2011).

[167] S. Hein, H. Tran, and A. Steinbüchel, Synechocystis sp. pcc6803 possesses a two-component polyhydroxyalkanoic acid synthase similar to that of anoxygenic purple sulfur bacteria, *Archives of microbiology* **170**(3), 162–170 (1998).

[168] X. Lu, A perspective: photosynthetic production of fatty acid-based biofuels in genetically engineered cyanobacteria, *Biotechnology advances* **28**(6), 742–746 (2010).

[169] G. Taroncher-Oldenburg, K. Nishina, and G. Stephanopoulos, Identification and analysis of the polyhydroxyalkanoate-specific β-ketothiolase and acetoacetyl coenzyme a reductase genes in the cyanobacterium synechocystis sp. strain pcc6803, *Appl. Environ. Microbiol.* **66**(10), 4440–4448 (2000).

[170] L. F. Dawson, E. Valiente, A. Faulds-Pain, E. H. Donahue, and B. W. Wren, Characterisation of *Clostridium difficile* biofilm formation, a role for spo0a, *PloS one* **7**(12), e50527 (2012).

[171] T. Dhapa, R. Leuzzi, Y. K. Ng, S. T. Baban, R. Adamo, S. A. Kuehne, M. Scarselli, N. P. Minton, D. Serruto, and M. Unnikrishnan, Multiple factors modulate biofilm formation by the anaerobic pathogen *Clostridium difficile*, *Journal of bacteriology* **195**(3), 545–555 (2013).

[172] G. Donelli, C. Vuotto, R. Cardines, and P. Mastrantonio, Biofilm-growing intestinal anaerobic bacteria, *FEMS Immunology & Medical Microbiology* **65**(2), 318–325 (2012).

[173] E. G. Semenyuk, M. L. Laning, J. Foley, P. F. Johnston, K. L. Knight, D. N. Gerding, and A. Driks, Spore formation and toxin production in *Clostridium difficile* biofilms, *PloS one* **9**(1), e87757 (2014).

[174] S. Macfarlane and J. Dillon, Microbial biofilms in the human gastrointestinal tract, *Journal of Applied Microbiology* **102**(5), 1187–1196 (2007).

[175] A. B. Shreiner, J. Y. Kao, and V. B. Young, The gut microbiome in health and in disease, *Current opinion in gastroenterology* **31**(1), 69 (2015).

[176] M. A. Henson and P. Phalak, Byproduct cross feeding and community stability in an in silico biofilm model of the gut microbiome, *Processes* **5**(1), 13 (2017).

[177] M. A. Henson and P. Phalak, Microbiota dysbiosis in inflammatory bowel diseases: *in silico* investigation of the oxygen hypothesis, *BMC Systems Biology* **11**(1), 145 (2017).

[178] A. Rivière, M. Selak, D. Lantin, F. Leroy, and L. De Vuyst, Bifidobacteria and butyrate-producing colon bacteria: importance and strategies for their stimulation in the human gut, *Frontiers in microbiology* **7**, 979 (2016).

[179] D. Ríos-Covián, P. Ruas-Madiedo, A. Margolles, M. Gueimonde, C. G. de los Reyes-Gavilán, and N. Salazar, Intestinal short chain fatty acids and their link with diet and human health, *Frontiers in microbiology* **7**, 185 (2016).

[180] G. Jakobsdottir, J. Xu, G. Molin, S. Ahrne, and M. Nyman, High-fat diet reduces the formation of butyrate, but increases succinate, inflammation, liver fat and cholesterol in rats, while dietary fibre counteracts these effects, *PloS one* **8**(11), e80476 (2013).

[181] H. Dannheim, S. E. Will, D. Schomburg, and M. Neumann-Schaal, *Clostridioides difficile* 630δerm in silico and in vivo–quantitative growth and extensive polysaccharide secretion, *FEBS open bio* **7**(4), 602–615 (2017).

[182] A. Heinken, S. Sahoo, R. M. Fleming, and I. Thiele, Systems-level characterization of a host-microbe metabolic symbiosis in the mammalian gut, *Gut microbes* **4**(1), 28–40 (2013).

[183] A. Heinken, M. T. Khan, G. Paglia, D. A. Rodionov, H. J. Harmsen, and I. Thiele, Functional metabolic map of *Faecalibacterium prausnitzii*, a beneficial human gut microbe, *Journal of bacteriology* **196**(18), 3289–3302 (2014).

[184] D. J. Baumler, R. G. Peplinski, J. L. Reed, J. D. Glasner, and N. T. Perna, The evolution of metabolic networks of *E. coli*, *BMC systems biology* **5**(1), 182 (2011).

[185] S. Karlsson, L. G. Burman, and T. Åkerlund, Suppression of toxin production in *Clostridium difficile* vpi 10463 by amino acids, *Microbiology* **145**(7), 1683–1693 (1999).

[186] M. Neumann-Schaal, J. D. Hofmann, S. E. Will, and D. Schomburg, Time-resolved amino acid uptake of *Clostridium difficile* 630δerm and concomitant fermentation product and toxin formation, *BMC microbiology* **15**(1), 281 (2015).

[187] Z.-L. Dai, G. Wu, and W.-Y. Zhu, Amino acid metabolism in intestinal bacteria: links between gut ecology and host health, *Front Biosci* **16**(1), 1768–1786 (2011).

[188] H. Horn and S. Lackner, Modeling of biofilm systems: a review, in *Productive Biofilms* (2014), pp. 53–76.

[189] A. Spor, O. Koren, and R. Ley, Unravelling the effects of the environment and host genotype on the gut microbiome, *Nature Reviews Microbiology* **9**(4), 279–290 (2011).

[190] C. De Filippo, D. Cavalieri, M. Di Paola, M. Ramazzotti, J. B. Poullet, S. Massart, S. Collini, G. Pieraccini, and P. Lionetti, Impact of diet in shaping gut microbiota revealed by a comparative study in children from europe and rural africa, *Proceedings of the National Academy of Sciences* **107**(33), 14691–14696 (2010).

[191] C. M. Theriot, M. J. Koenigsknecht, P. E. Carlson Jr, G. E. Hatton, A. M. Nelson, B. Li, G. B. Huffnagle, J. Z. Li, and V. B. Young, Antibiotic-induced shifts in the mouse gut microbiome and metabolome increase susceptibility to *Clostridium difficile* infection, *Nature communications* **5** (2014).

[192] K. M. Utzschneider, M. Kratz, C. J. Damman, and M. Hullarg, Mechanisms linking the gut microbiome and glucose metabolism, *The Journal of Clinical Endocrinology & Metabolism* **101**(4), 1445–1454 (2016).

[193] R. N. Carmody, G. K. Gerber, J. M. Luevano, D. M. Gatti, L. Somes, K. L. Svenson, and P. J. Turnbaugh, Diet dominates host genotype in shaping the murine gut microbiota, *Cell host & microbe* **17**(1), 72–84 (2015).

[194] X. Zhang, D. Shen, Z. Fang, Z. Jie, X. Qiu, C. Zhang, Y. Chen, and L. Ji, Human gut microbiota changes reveal the progression of glucose intolerance, *PloS one* **8**(8), e71108 (2013).

[195] T. D. Lawley, S. Clare, A. W. Walker, M. D. Stares, T. R. Connor, C. Raisen, D. Goulding, R. Rad, F. Schreiber, C. Brandt, *et al.*, Targeted restoration of the intestinal microbiota with a simple, defined bacteriotherapy resolves relapsing *Clostridium difficile* disease in mice, *PLoS Pathog* **8**(10), e1002995 (2012).

[196] C. Byrne, E. Chambers, D. Morrison, and G. Frost, The role of short chain fatty acids in appetite regulation and energy homeostasis, *International journal of obesity* **39**(9), 1331–1338 (2015).

[197] J. A. Ferreyra, K. J. Wu, A. J. Hryckowian, D. M. Bouley, B. C. Weimer, and J. L. Sonnenburg, Gut microbiota-produced succinate promotes c. difficile infection after antibiotic treatment or motility disturbance, *Cell host & microbe* **16**(6), 770–777 (2014).

[198] M. Köpke, M. Straub, and P. Dürre, *Clostridium difficile* is an autotrophic bacterial pathogen, *PLoS One* **8**(4), e62157 (2013).

[199] J. M. Campbell, G. C. Fahey, and B. W. Wolf, Selected indigestible oligosaccharides affect large bowel mass, cecal and fecal short-chain fatty acids, ph and microflora in rats, *The Journal of nutrition* **127**(1), 130–136 (1997).

[200] S. Jackson, M. Calos, A. Myers, and W. T. Self, Analysis of proline reduction in the nosocomial pathogen *Clostridium difficile*, *Journal of bacteriology* **188**(24), 8487–8495 (2006).

[201] D. A. Antonopoulos, S. M. Huse, H. G. Morrison, T. M. Schmidt, M. L. Sogin, and V. B. Young, Reproducible community dynamics of the gastrointestinal microbiota following antibiotic perturbation, *Infection and immunity* **77**(6), 2367–2375 (2009).

[202] V. C. Antharam, E. C. Li, A. Ishmael, A. Sharma, V. Mai, K. H. Rand, and G. P. Wang, Intestinal dysbiosis and depletion of butyrogenic bacteria in *Clostridium difficile* infection and nosocomial diarrhea, *Journal of clinical microbiology* **51**(9), 2884–2892 (2013).

[203] C. Vincent and A. Manges, Antimicrobial use, human gut microbiota and clostridium difficile colonization and infection, *Antibiotics* **4**(3), 230–253 (2015).

[204] S. Schippa and M. P. Conte, Dysbiotic events in gut microbiota: impact on human health, *Nutrients* **6**(12), 5786–5805 (2014).

[205] C. Tamboli, C. Neut, P. Desreumaux, and J. Colombel, Dysbiosis in inflammatory bowel disease, *Gut* **53**(1), 1–4 (2004).

[206] K. Honda and D. R. Littman, The microbiome in infectious disease and inflammation, *Annual review of immunology* **30**, 759–795 (2012).

[207] Z. Ling, X. Liu, X. Jia, Y. Cheng, Y. Luo, L. Yuan, Y. Wang, C. Zhao, S. Guo, L. Li, *et al.*, Impacts of infection with different toxigenic *Clostridium difficile* strains on faecal microbiota in children, *Scientific reports* **4**, 7485 (2014).

[208] J. M. Ridlon, D.-J. Kang, and P. B. Hylemon, Bile salt biotransformations by human intestinal bacteria, *Journal of lipid research* **47**(2), 241–259 (2006).

[209] K. Setchell, A. Lawson, N. Tanida, and J. Sjövall, General methods for the analysis of metabolic profiles of bile acids and related compounds in feces., *Journal of lipid research* **24**(8), 1085–1100 (1983).

[210] J. A. Winston and C. M. Theriot, Impact of microbial derived secondary bile acids on colonization resistance against *Clostridium difficile* in the gastrointestinal tract, *Anaerobe* **41**, 44–50 (2016).

[211] M. C. Rea, A. Dobson, O. O'Sullivan, F. Crispie, F. Fouhy, P. D. Cotter, F. Shanahan, B. Kiely, C. Hill, and R. P. Ross, Effect of broad-and narrow-spectrum antimicrobials on *Clostridium difficile* and microbial diversity in a model of the distal colon, *Proceedings of the National Academy of Sciences* **108**(Supplement 1), 4639–4644 (2011).

[212] J. A. Sorg and A. L. Sonenshein, Bile salts and glycine as cogerminants for clostridium difficile spores, *Journal of bacteriology* **190**(7), 2505–2512 (2008).

[213] J. A. Sorg and A. L. Sonenshein, Inhibiting the initiation of clostridium difficile spore germination using analogs of chenodeoxycholic acid, a bile acid, *Journal of bacteriology* **192**(19), 4983–4990 (2010).

[214] J. R. Allegretti, S. Kearney, N. Li, E. Bogart, K. Bullock, G. K. Gerber, L. Bry, C. B. Clish, E. Alm, and J. Korzenik, Recurrent *Clostridium difficile* infection associates with distinct bile acid and microbiome profiles, *Alimentary pharmacology & therapeutics* **43**(11), 1142–1153 (2016).

[215] K. H. Wilson, M. J. Kennedy, and F. R. Fekety, Use of sodium taurocholate to enhance spore recovery on a medium selective for clostridium difficile., *Journal of clinical microbiology* **15**(3), 443–446 (1982).

[216] B. Buggy, C. Hawkins, and R. Fekety, Effect of adding sodium taurocholate to selective media on the recovery of clostridium difficile from environmental surfaces., *Journal of clinical microbiology* **21**(4), 636–637 (1985).

[217] K. H. Wilson, Efficiency of various bile salt preparations for stimulation of clostridium difficile spore germination., *Journal of clinical microbiology* **18**(4), 1017–1019 (1983).

[218] A. M. Seekatz and V. B. Young, *Clostridium difficile* and the microbiota, *The Journal of clinical investigation* **124**(10), 4182–4189 (2014).

[219] E. Thursby and N. Juge, Introduction to the human gut microbiota, *Biochemical Journal* **474**(11), 1823–1836 (2017).

[220] M. A. Engevik, K. A. Engevik, M. B. Yacyshyn, J. Wang, D. J. Hassett, B. Darien, B. R. Yacyshyn, and R. T. Worrell, Human *Clostridium difficile* infection: inhibition of nhe3 and microbiota profile, *American Journal of Physiology-Gastrointestinal and Liver Physiology* **308**(6), G497–G509 (2015).

[221] J. P. Ouwerkerk, W. M. de Vos, and C. Belzer, Glycobiome: bacteria and mucus at the epithelial interface, *Best practice & research Clinical gastroenterology* **27**(1), 25–38 (2013).

[222] C. L. Ross, J. K. Spinler, and T. C. Savidge, Structural and functional changes within the gut microbiota and susceptibility to *Clostridium difficile* infection, *Anaerobe* **41**, 37–43 (2016).

[223] H. P. Browne, S. C. Forster, B. O. Anonye, N. Kumar, B. A. Neville, M. D. Stares, D. Goulding, and T. D. Lawley, Culturing of 'unculturable'human microbiota reveals novel taxa and extensive sporulation, *Nature* **533**(7604), 543–546 (2016).

[224] C. Staley, A. R. Weingarden, A. Khoruts, and M. J. Sadowsky, Interaction of gut microbiota with bile acid metabolism and its influence on disease states, *Applied microbiology and biotechnology* **101**(1), 47–64 (2017).

[225] S. P. Myers, The causes of intestinal dysbiosis: a review, *Altern Med Rev* **9**(2), 180–197 (2004).

[226] R. K. Singh, H.-W. Chang, D. Yan, K. M. Lee, D. Ucmak, K. Wong, M. Abrouk, B. Farahnik, M. Nakamura, T. H. Zhu, *et al.*, Influence of diet on the gut microbiome and implications for human health, *Journal of translational medicine* **15**(1), 73 (2017).

[227] N. Kamada, G. Y. Chen, N. Inohara, and G. Núñez, Control of pathogens and pathobionts by the gut microbiota, *Nature immunology* **14**(7), 685–690 (2013).

[228] A. R. Weingarden, C. Chen, A. Bobr, D. Yao, Y. Lu, V. M. Nelson, M. J. Sadowsky, and A. Khoruts, Microbiota transplantation restores normal fecal bile acid composition in recurrent *Clostridium difficile* infection, *American Journal of Physiology-Gastrointestinal and Liver Physiology* **306**(4), G310–G319 (2013).

[229] A. Heinken and I. Thiele, Systematic prediction of health-relevant human-microbial co-metabolism through a computational framework, *Gut Microbes* **6**(2), 120–130 (2015).

[230] S. Shoaie and J. Nielsen, Elucidating the interactions between the human gut microbiota and its host through metabolic modeling, *Frontiers in genetics* **5** (2014).

[231] I. Thiele, A. Heinken, and R. M. Fleming, A systems biology approach to studying the role of microbes in human health, *Current opinion in biotechnology* **24**(1), 4–12 (2013).

[232] M. Glick-Bauer and M.-C. Yeh, The health advantage of a vegan diet: exploring the gut microbiota connection, *Nutrients* **6**(11), 4822–4838 (2014).

[233] N. Swainston, P. Mendes, and D. B. Kell, An analysis of a 'community-driven'reconstruction of the human metabolic network, *Metabolomics* **9**(4), 757–764 (2013).

[234] I. Thiele, N. Swainston, R. M. Fleming, A. Hoppe, S. Sahoo, M. K. Aurich, H. Haraldsdottir, M. L. Mo, O. Rolfsson, M. D. Stobbe, *et al.*, A community-driven global reconstruction of human metabolism, *Nature biotechnology* **31**(5), 419 (2013).

[235] I. Thiele, S. Sahoo, A. Heinken, L. Heirendt, M. K. Aurich, A. Noronha, and R. M. Fleming, When metabolism meets physiology: Harvey and harvetta, *bioRxiv* p. 255885 (2018).

[236] R. G. Frykberg and J. Banks, Challenges in the treatment of chronic wounds, *Advances in wound care* **4**(9), 560–582 (2015).

[237] N. A. Richmond, A. D. Maderal, and A. C. Vivas, Evidence-based management of common chronic lower extremity ulcers, *Dermatologic therapy* **26**(3), 187–196 (2013).

[238] D. D. Rhoads, R. D. Wolcott, Y. Sun, and S. E. Dowd, Comparison of culture and molecular identification of bacteria in chronic wounds, *International journal of molecular sciences* **13**(3), 2535–2550 (2012).

[239] J. H. Melendez, Y. M. Frankel, A. T. An, L. Williams, L. B. Price, N.-Y. Wang, G. S. Lazarus, and J. M. Zenilman, Real-time pcr assays compared to culture-based approaches for identification of aerobic bacteria in chronic wounds, *Clinical Microbiology and Infection* **16**(12), 1762–1769 (2010).

[240] D. N. Frank, A. Wysocki, D. D. Specht-Glick, A. Rooney, R. A. Feldman, A. L. St. Amand, N. R. Pace, and J. D. Trent, Microbial diversity in chronic open wounds, *Wound repair and regeneration* **17**(2), 163–172 (2009).

[241] V. Gontcharova, E. Youn, Y. Sun, R. D. Wolcott, and S. E. Dowd, A comparison of bacterial composition in diabetic ulcers and contralateral intact skin, *The open microbiology journal* **4**, 8 (2010).

[242] A. B. Wysocki, S. K. Bhalla-Regev, P. M. Tierno Jr, M. Stevens-Riley, and R.-C. Wiygul, Proteolytic activity by multiple bacterial species isolated from chronic venous leg ulcers degrades matrix substrates, *Biological research for nursing* **15**(4), 407–415 (2013).

[243] U. Trivedi, S. Parameswaran, A. Armstrong, D. Burgueno-Vega, J. Griswold, S. Dissanaike, and K. P. Rumbaugh, Prevalence of multiple antibiotic resistant infections in diabetic versus nondiabetic wounds, *Journal of pathogens* **2014** (2014).

[244] A. Hotterbeekx, S. Kumar-Singh, H. Goossens, and S. Malhotra-Kumar, In vivo and in vitro interactions between pseudomonas aeruginosa and staphylococcus spp., *Frontiers in cellular and infection microbiology* **7**, 106 (2017).

[245] C. N. Marques, P. W. Woods, Z. M. Haynes, and E. G. Mina, Maintenance of s. aureus in co-culture with p. aeruginosa while growing as biofilms, *Frontiers in microbiology* **9**, 3291 (2018).

[246] P. M. Alves, E. Al-Badi, C. Withycombe, P. M. Jones, K. J. Purdy, and S. E. Maddocks, Interaction between staphylococcus aureus and pseudomonas

aeruginosa is beneficial for colonisation and pathogenicity in a mixed biofilm, *Pathogens and disease* **76**(1), fty003 (2018).

[247] M. Loesche, S. E. Gardner, L. Kalan, J. Horwinski, Q. Zheng, B. P. Hodkinson, A. S. Tyldsley, C. L. Franciscus, S. L. Hillis, S. Mehta, *et al.*, Temporal stability in chronic wound microbiota is associated with poor healing, *Journal of Investigative Dermatology* **137**(1), 237–244 (2017).

[248] M. M. Ramsey and M. Whiteley, Polymicrobial interactions stimulate resistance to host innate immunity through metabolite perception, *Proceedings of the National Academy of Sciences* **106**(5), 1578–1583 (2009).

[249] K. E. Weimer, R. A. Juneau, K. A. Murrah, B. Pang, C. E. Armbruster, S. H. Richardson, and W. E. Swords, Divergent mechanisms for passive pneumococcal resistance to β-lactam antibiotics in the presence of haemophilus influenzae, *Journal of Infectious Diseases* **203**(4), 549–555 (2011).

[250] M. D. Mastropaolo, N. P. Evans, M. K. Byrnes, A. M. Stevens, J. L. Robertson, and S. B. Melville, Synergy in polymicrobial infections in a mouse model of type 2 diabetes, *Infection and immunity* **73**(9), 6055–6063 (2005).

[251] A. Korgaonkar, U. Trivedi, K. P. Rumbaugh, and M. Whiteley, Community surveillance enhances pseudomonas aeruginosa virulence during polymicrobial infection, *Proceedings of the National Academy of Sciences* **110**(3), 1059–1064 (2013).

[252] V. Tzaneva, I. Mladenova, G. Todorova, and D. Petkov, Antibiotic treatment and resistance in chronic wounds of vascular origin, *Clujul Medical* **89**(3), 365 (2016).

[253] J. Jneid, J. Lavigne, B. La Scola, and N. Cassir, The diabetic foot microbiota: a review, *Human Microbiome Journal* **5**, 1–6 (2017).

[254] J. C. Alper, E. A. Welch, M. Ginsberg, H. Bogaars, and P. Maguire, Moist wound healing under a vapor permeable membrane, *Journal of the American Academy of Dermatology* **8**(3), 347–353 (1983).

[255] P. Stephens, I. Wall, M. Wilson, K. Hill, C. Davies, C. Hill, K. Harding, and D. Thomas, Anaerobic cocci populating the deep tissues of chronic wounds impair cellular wound healing responses in vitro, *British Journal of Dermatology* **148**(3), 456–466 (2003).

[256] R. F. Sood, H. Gu, D. Djukovic, L. Deng, M. Ga, L. A. Muffley, D. Raftery, and A. M. Hocking, Targeted metabolic profiling of wounds in diabetic and nondiabetic mice, *Wound Repair and Regeneration* **23**(3), 423–434 (2015).

[257] M. C. B. Ammons, K. Morrissey, B. P. Tripet, J. T. Van Leuven, A. Han, G. S. Lazarus, J. M. Zenilman, P. S. Stewart, G. A. James, and V. Copié,

Biochemical association of metabolic profile and microbiome in chronic pressure ulcer wounds, *PloS one* **10**(5), e0126735 (2015).

[258] A. Junka, W. Wojtowicz, A. Zabek, G. Krasowski, D. Smutnicka, B. Bakalorz, A. Boruta, M. Dziadas, P. Młynarz, P. P. Sedghizadeh, *et al.*, Metabolic profiles of exudates from chronic leg ulcerations, *Journal of pharmaceutical and biomedical analysis* **137**, 13–22 (2017).

[259] Y. Sun, S. E. Dowd, E. Smith, D. D. Rhoads, and R. D. Wolcott, In vitro multispecies lubbock chronic wound biofilm model, *Wound repair and regeneration* **16**(6), 805–813 (2008).

[260] R. Li, M. A. Henson, and M. J. Kurtz, Selection of model parameters for off-line parameter estimation, *IEEE Transactions on control systems technology* **12**(3), 402–412 (2004).

[261] L. J. Bessa, P. Fazii, M. Di Giulio, and L. Cellini, Bacterial isolates from infected wounds and their antibiotic susceptibility pattern: some remarks about wound infection, *International wound journal* **12**(1), 47–52 (2015).

[262] A. Körber, E. Schmid, J. Buer, J. Klode, D. Schadendorf, and J. Dissemond, Bacterial colonization of chronic leg ulcers: current results compared with data 5 years ago in a specialized dermatology department, *Journal of the European Academy of Dermatology and Venereology* **24**(9), 1017–1025 (2010).

[263] M. Fazli, T. Bjarnsholt, K. Kirketerp-Møller, B. Jørgensen, A. S. Andersen, K. A. Krogfelt, M. Givskov, and T. Tolker-Nielsen, Nonrandom distribution of *Pseudomonas aeruginosa* and *Staphylococcus aureus* in chronic wounds, *Journal of clinical microbiology* **47**(12), 4084–4089 (2009).

[264] T. D. Thomas, D. C. Ellwood, and V. M. C. Longyear, Change from homo-to heterolactic fermentation by streptococcus lactis resulting from glucose limitation in anaerobic chemostat cultures, *Journal of bacteriology* **138**(1), 109–117 (1979).

[265] C. Keevil, P. Marsh, and D. Ellwood, Regulation of glucose metabolism in oral streptococci through independent pathways of glucose 6-phosphate and glucose 1-phosphate formation., *Journal of bacteriology* **157**(2), 560–567 (1984).

[266] S. Imam, S. Schäuble, A. N. Brooks, N. S. Baliga, and N. D. Price, Data-driven integration of genome-scale regulatory and metabolic network models, *Frontiers in microbiology* **6**, 409 (2015).

[267] M. Conde, P. do Rosario, T. Sauter, and T. Pfau, Constraint based modeling going multicellular, *Frontiers in molecular biosciences* **3**, 3 (2016).

[268] M. T. Ferreira, A. S. Manso, P. Gaspar, M. G. Pinho, and A. R. Neves, Effect of oxygen on glucose metabolism: utilization of lactate in staphylococcus aureus as revealed by in vivo nmr studies, *PLoS One* **8**(3), e58277 (2013).

[269] J. P. Furuno, J. N. Hebden, H. C. Standiford, E. N. Perencevich, R. R. Miller, A. C. Moore, S. M. Strauss, and A. D. Harris, Prevalence of methicillin-resistant staphylococcus aureus and acinetobacter baumannii in a long-term acute care facility, *American journal of infection control* **36**(7), 468–471 (2008).

[270] F. A. Manian, S. Griesenauer, D. Senkel, J. M. Setzer, S. A. Doll, A. M. Perry, and M. Wiechens, Isolation of acinetobacter baumannii complex and methicillin-resistant staphylococcus aureus from hospital rooms following terminal cleaning and disinfection: can we do better?, *Infection Control & Hospital Epidemiology* **32**(7), 667–672 (2011).

[271] F. Barbut, S. Yezli, M. Mimoun, J. Pham, M. Chaouat, and J. A. Otter, Reducing the spread of acinetobacter baumannii and methicillin-resistant staphylococcus aureus on a burns unit through the intervention of an infection control bundle, *Burns* **39**(3), 395–403 (2013).

[272] H. W. Boucher, G. H. Talbot, J. S. Bradley, J. E. Edwards, D. Gilbert, L. B. Rice, M. Scheld, B. Spellberg, and J. Bartlett, Bad bugs, no drugs: no eskape! an update from the infectious diseases society of america, *Clinical infectious diseases* **48**(1), 1–12 (2009).

[273] S. Santajit and N. Indrawattana, Mechanisms of antimicrobial resistance in eskape pathogens, *BioMed research international* **2016** (2016).

[274] M. Mayo, R. Schlitzer, M. Ward, L. Wilson, and D. Ahearn, Association of pseudomonas and serratia corneal ulcers with use of contaminated solutions., *Journal of clinical microbiology* **25**(8), 1398–1400 (1987).

[275] Y. Tashiro, Y. Yawata, M. Toyofuku, H. Uchiyama, and N. Nomura, Interspecies interaction between pseudomonas aeruginosa and other microorganisms, *Microbes and environments* **28**(1), 13–24 (2013).

[276] L. Chávez de Paz, J. R. Davies, G. Bergenholtz, and G. Svensäter, Strains of enterococcus faecalis differ in their ability to coexist in biofilms with other root canal bacteria, *International endodontic journal* **48**(10), 916–925 (2015).

[277] Y. Gao, X. Jiang, D. Lin, Y. Chen, and Z. Tong, The starvation resistance and biofilm formation of enterococcus faecalis in coexistence with candida albicans, streptococcus gordonii, actinomyces viscosus, or lactobacillus acidophilus, *Journal of endodontics* **42**(8), 1233–1238 (2016).

[278] M. Cavaliere, S. Feng, O. S. Soyer, and J. I. Jiménez, Cooperation in microbial communities and their biotechnological applications, *Environmental microbiology* **19**(8), 2949–2963 (2017).

[279] J. Davies and D. Davies, Origins and evolution of antibiotic resistance, *Microbiol. Mol. Biol. Rev.* **74**(3), 417–433 (2010).

[280] C. W. Hall and T.-F. Mah, Molecular mechanisms of biofilm-based antibiotic resistance and tolerance in pathogenic bacteria, *FEMS microbiology reviews* **41**(3), 276–301 (2017).

[281] S. E. Gardner and R. A. Frantz, Wound bioburden and infection-related complications in diabetic foot ulcers, *Biological research for nursing* **10**(1), 44–53 (2008).

[282] A. M. Misic, S. E. Gardner, and E. A. Grice, The wound microbiome: modern approaches to examining the role of microorganisms in impaired chronic wound healing, *Advances in wound care* **3**(7), 502–510 (2014).

[283] M. S. Tuttle, Association between microbial bioburden and healing outcomes in venous leg ulcers: a review of the evidence, *Advances in wound care* **4**(1), 1–11 (2015).

[284] L. B. Price, C. M. Liu, J. H. Melendez, Y. M. Frankel, D. Engelthaler, M. Aziz, J. Bowers, R. Rattray, J. Ravel, C. Kingsley, *et al.*, Community analysis of chronic wound bacteria using 16s rrna gene-based pyrosequencing: impact of diabetes and antibiotics on chronic wound microbiota, *PloS one* **4**(7), e6462 (2009).

[285] D. D. Rhoads, S. B. Cox, E. J. Rees, Y. Sun, and R. D. Wolcott, Clinical identification of bacteria in human chronic wound infections: culturing vs. 16s ribosomal dna sequencing, *BMC infectious diseases* **12**(1), 321 (2012).

[286] A. R. Halbert, M. C. Stacey, J. B. Rohr, and A. Jopp-Mckay, The effect of bacterial colonization on venous ulcer healing, *Australasian journal of dermatology* **33**(2), 75–80 (1992).

[287] S. M. Madsen, H. Westh, L. Danielsen, and V. T. Rosdahl, Bacterial colonization and healing of venous leg ulcers, *Apmis* **104**(7-8), 895–899 (1996).

[288] K. Kirketerp-Møller, P. Ø. Jensen, M. Fazli, K. G. Madsen, J. Pedersen, C. Moser, T. Tolker-Nielsen, N. Høiby, M. Givskov, and T. Bjarnsholt, Distribution, organization, and ecology of bacteria in chronic wounds, *Journal of clinical microbiology* **46**(8), 2717–2722 (2008).

[289] R. H. Demling and B. Waterhouse, The increasing problem of wound bacterial burden and infection in acute and chronic soft-tissue wounds caused by methicillin-resistant staphylococcus aureus, *Journal of burns and wounds* **7** (2007).